MATHEMATICAL MODELING OF SENSING AND FEEDING BY COPEPODS

A DISSERTATION SUBMITTED TO THE GRADUATE DIVISION OF THE
UNIVERSITY OF HAWAIʻI AT MĀNOA IN PARTIAL FULFILLMENT OF THE
REQUIREMENTS FOR THE DEGREE OF

DOCTOR OF PHILOSOPHY

IN

MATHEMATICS

December 2022

By
Julian O. Hachmeister

Dissertation Committee:

Daisuke Takagi, Chairperson
Monique Chyba
Evan Gawlik
Yuriy Mileyko
John Allen

Acknowledgements

This has been a long journey that I haven't accomplished on my own.

I would like to first thank Dr. Daisuke Takagi for his help and guidance throughout the years. He has been a great mentor and without his support I would not have made it this far. I would also like to thank my wife Katie for her words of encouragement and an open ear, my mother Virginia who has also been a constant source of motivation during trying times, and Sue and Alicia from the UH Manoa math department office who have also been invaluable. I would also like to thank the committee members for their time, support and critique of this dissertation.

I deeply appreciate everyone's help in encouraging me to grow and supporting me along this journey.

Lastly, I would like to thank the NSF for funding this research, Award number 1603929.

Abstract

The ability to feed effectively is a fundamental skill required for survival. Microscopic crustaceans called copepods are a great example of an animal that are very adept at eating. They are tiny creatures, roughly on the order of 1 mm, and so their fluid environment is not like the water that we are accustomed to, but rather, is more like that of honey. To make things even more difficult, they have poor eyesight and are only able to detect the presence of light. Instead of using vision to detect the presence of food, they rely on other sensory mechanics like chemical signals and hydromechanical disturbances to remotely detect their prey. Another challenge they are presented with is moving a particle to a desired location for inspection and consumption. Given the high viscosity of their environment, particle transport is difficult since small objects near the boundary of a body will tend to stick to and move with the motion of the body.

In this dissertation, we first create a model for three modes of feeding: sinking, swimming and hovering. For each of the three modes, we first create the flow fields by including the antennae, a feature often neglected in previous studies. Then, we measure the magnitude of the disturbance vector induced by a spherical particle located in a plane with sensor locations along the antennae. From this, a detectable volume is generated showing what the model could theoretically detect over a given period of time. What we discover is that sinking may be a preferable mode of feeding if the copepod were surrounded by food. If the copepod is unable to detect anything, then swimming might be best as it would increase the copepod's chances of encountering food. If the copepod came across a dense cluster of food, then positioning underneath the cluster could be the best mode as it would allow the copepod to funnel the food from above to its body.

In the second and third chapter, we explore the copepod's ability to transport small particles using the Weis-Fogh fling and clap mechanism. Copepods have been observed performing this motion as early as the 1980's but there have been no mathematical models for the fling and clap in the Stokes regime. We investigate the efficacy of the motion by representing a pair of appendages as either a pair of rods or a pair of plates. What we discover is that both representations lead to a positive net displacement of particles in the desired direction and that increasing the maximum slope a of the appendages lead to an increase in the displacement, specifically on the order of a^2 for small values of a.

Table of Contents

List of Tables

List of Figures

Chapter 1

Introduction

The focus of this document is the compilation of research conducted under the guidance of Dr. Daisuke Takagi over the past several years regarding the feeding behavior of copepods. Within it, I will include my journey through the subject, the foundation of the research, the results and their implications.

The ability to feed oneself is an important requirement for the survival of any animal. In order to feed, there are two fundamental steps required to do so successfully. First, an animal must be able to sense its prey. Then, the animal needs to bring it to its mouth in order to ingest it. In this document, we will focus on the sensing capabilities and feeding mechanics of a specific aquatic animal, the copepod. While they live in the same fluid that we interact with when we jump into the ocean or a lake, the relative size difference changes the characteristics of the water so that it is less like what we are accustomed to, and more like honey. To make matters worse, they are unable to detect their prey visually and must rely on other sensory mechanisms. Furthermore, the sticky environment adds further difficulties as it is difficult to manipulate particle matter at such a small scale. Nonetheless, these animals have not only found a way to overcome these challenges but to do so effectively.

1.1 Motivational problem

My study began with the manipulation of small submerged particulate matter, or more broadly, the ability to bring sustenance to the body for the purpose of consumption. The problem that arises in this scenario is that motions that we are accustomed to with the purpose of transporting particles do not work at this scale. Specifically, our motions rely on displacement due to inertial forces while at the microscopic scale, under appropriate velocity scales, viscous forces overcome inertial forces. The dynamics in a fluid environment can be categorized by a dimensionless quantity called the Reynolds number given by

$$\mathrm{Re} = \frac{\rho U L}{\mu} = \frac{\text{inertial forces}}{\text{viscous terms}} \tag{1.1}$$

where ρ is the fluid density, U and L are the characteristic velocity and length scales, and μ is the viscosity of the fluid. Around a feeding copepod, the typical Reynolds number from $\mathrm{Re} \ll 1$ to $\mathrm{Re} \approx O(1)$. In this regime, motions that look the same whether played forward or backward in time, irregardless of the speed of the movements, will produce no net displacement. This is a feature of what is called reciprocal motion.

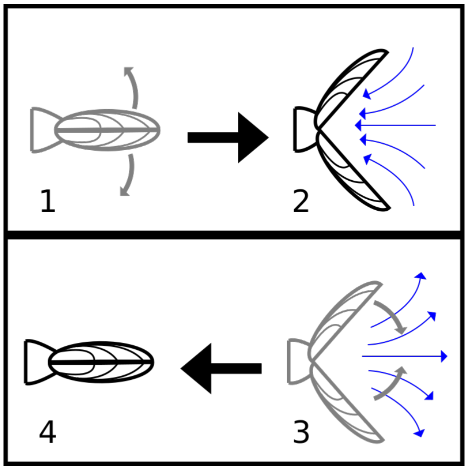

Figure 1.1: The motion of the scallop throughout the scallop theorem. The top image shows the first half of the cycle, close (1) to open (2). The lower image shows the second half of the cycle, open (3) to close (4). The gray outlined image shows the original position and shape of the scallop and the black outlined image shows the final position and shape after the respective half of the cycle has finished. The gray arrows show the direction in which the shell is opening. Generic path of the fluid are shown in blue lines with arrows showing that direction of the flow.

The key concept of reciprocal motion is described by E.M. Purcell in his paper titled *Life at low Reynolds number* with the scallop theorem (Purcell 1977). The idea is that a scallop propels itself through the motion of opening its shell, drawing in the surrounding fluid, and then moving itself in the direction opposite that of the opening by quickly shutting its shell, and projecting the captured fluid. However, the opening and closing of the shell looks exactly the same regardless of whether we play the sequence backward or forward in time. As the scallop opens its shell, its body moves in one direction and as it closes, the body returns to its original position. Again, the reciprocal motion results in no net displacement of the body. The scallop theorem serves as a simple motion in which, at our scale as humans, is known to produce motion. For the example of the scallop, we can think of the mechanic used for *octopus vulgaris* to swim - drawing in water into its mantle and then ejecting it outwards through its funnel (Villanueva et al. 1997). These two methods are seemingly viable at our scale, yet at a microscopic scale fails to produce the desired effect. If motions that we are familiar with produce no net movement, then how do copepods overcome this problem and manipulate the surrounding fluid?

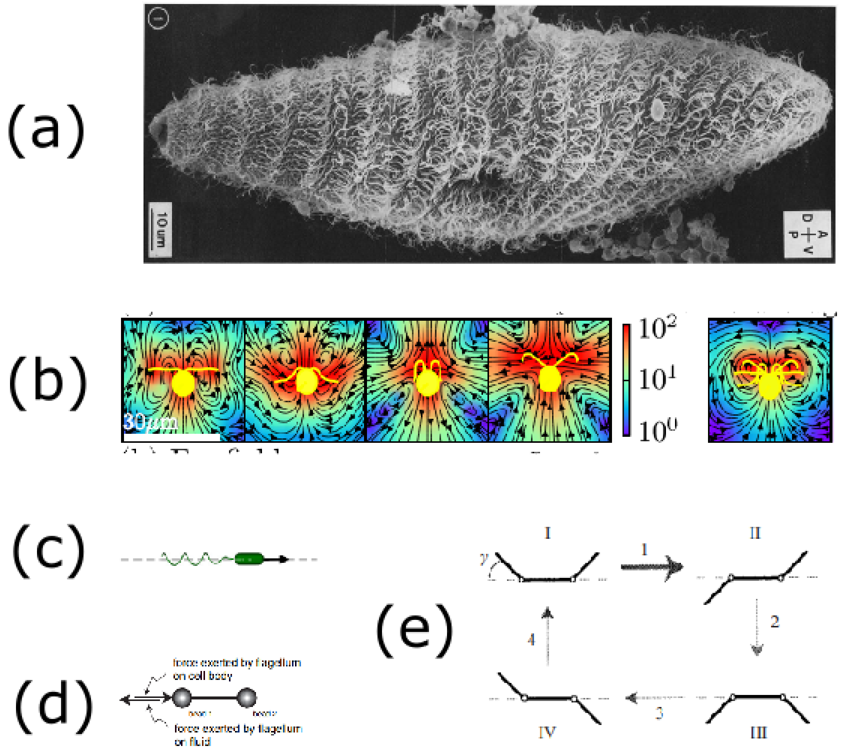

Figure 1.2: Four examples of microswimmers. (a) cilia covering a *paramecia*, image taken from (Tamm 1972) (b) sequence of flagella movements for *Chlamydomonas Reinhardtii*, image taken from (Klindt and Friedrich 2015) (c) helical tail microswimmer, image taken from (Klindt and Friedrich 2015) (d) dumb-bell microswimmer, image taken from (Hernandez-Ortiz et al. 2005) (e) Purcell's three link microswimmer, image taken from (Becker et al. 2003)

Locomotion at low Reynolds number flow is a topic that has been studied for quite some time. As was hopefully emphasized above, the mechanisms that we often conjure when thinking of swimming do not necessarily work in a viscous environment since propulsion is often obtained through acceleration of the water. When the fluid is thicker with a consistency more like honey, other methods are employed to produce displacement. For example, there is the single cell eukaryote *Paramecia* that have many long hair like cilia surrounding their body 1.2(a). Rows of cilia perform motion in sync by performing a power stroke and return to their original position by bending their cilia to produce drag on the water and break symmetry (Tamm 1972). Some microswimmers have a helical tail like structure called a flagella that are anchored at the base of their body which rotates in a corkscrew fashion in one direction which produces motion (Lauga and Powers 2009), figure 1.2(c). Other organisms such as spermatozoa oscillate their flagella to produce motion and have been modelled using a dumb-bell model as seen in figure 1.2(d) (Hernandez-Ortiz et al. 2005; Mueller and Thiffeault 2017). An algal cell known as *Chlamydomonas Reinhardtii* have a pair of flagella at the top end of their body. They are classified as pusher-puller as they use their flagellum to pull their body in a breaststroke-like motion to propel through the water (Jeanneret et al. 2016). See figure 1.2(b) for the sequence of motions of the pair of flagella. The time averaged flow fields generated by these organisms have been modelled by three point forces, two which point in the same direction for the forces representing the pulling motion and another in the opposite direction (Drescher et al. 2010; Andersen et al. 2015; Klindt and Friedrich 2015; Lighthill 1976). In each of these examples, the barrier of reciprocal motion has to be overcome. This is usually obtained by increasing the degrees of freedom in which the swimming appendages may be moved. Over the years, simplified mathematical models have been studied. For example, Purcell proposed a three-link microswimmer in which two of the links pivot about the point of attachment, figure 1.2(e). Others have looked into utilizing chemical reactions to induce movement. These are but a few examples, but illustrate that animals at microscopic scales are have generally basic geometric structures. Coupled with reciprocal motion, inventive and non-intuitive motions are required to overcome the time-reversal issue to produce locomotion. For animals with flexible appendages like cilia and flagella, breaking symmetry is not difficult as they are able to bend. Copepod appendages are rigid structures that do not bend. Therefore, in order to produce non-reciprocal motion, they must be employing different techniques in order to break the symmetry of their motion and ultimately produce net displacement.

Another problem that any animal encounters when feeding is initially locating its food source. Again, for us humans, this is a simple task. From the viewpoint of foraging for food, this is a matter of locating it visually. For example, as a gatherer we would find edible fruit through visual cues such as a recognizable bush or tree or as a hunter, locating tracks on the ground or other spotting prey in the distance. In each instance, visual cues serve as the signal that we interpret as detection of prey. Copepods are much more basic creatures however. Their visual acuity is very low and it is theorized that ability to see is restricted to only be able to detect the presence of light (Kiørboe 2011b). Therefore, they must rely on other sensory mechanisms to track down and detect their food. Two such ways they may detect the presence of a food source is through chemical trails or mechanical disturbances (Alcaraz et al. 1980). Focusing on the physical problem, we can investigate the implications of each method. Organic matter submerged in the ocean will leak a chemical plume which is advected throughout the water column. What this means is that the chemical signal can traverse quite a distance from its original source. However, while this may be considered as an ideal situation since the trail can be extended quite a long distance, the issue lies in the strength of the signal. The concentration of the signal, as a function of time, decreases as time increases. Since the chemical trail travels with the ambient current of the water column, we can then see that the strength of the chemical signal is then a function of its distance from the source. What this means is that the chemical signal, if strong enough, would be a good indicator of the presence of a food source, but the drawback is that because the trail moves with the current, pinpointing an exact location could be difficult.

1.2 Mechanical sensing

Copepods can also sense mechanical signals which they interpret through deflection of thin rod-like structures along their appendages and antennae called setae, see figure 1.3. While a copepod is engaged in a certain behavior, they generate a background flow and create a familiar velocity field around the animal which serves as a baseline. The presence of organic matter of a sufficient size interrupts the fluids pathlines. This in turn relays a signal back to the animal by disturbing the background flow and causing the setae to move in a way different from how it would in a flow field lacking the presence of an obstruction. An analogy to how this mechanism works would be with the movement of our own setae-like structures, the hair on our body. While we are engaged in whatever activity, our recollection of similar events remind us of what senses are triggered from which we catalog and remember. For example, we are able to detect the presence of the wind in the air through the movement of our hair compared to that of a windless day. Or if we are near or far from a wall while we quickly walk by based on how much or if our hair moves. These serve as physical cues alerting us to differences in the background air current based on a comparison between two scenarios - one in which we utilize as our baseline, an ideal situation where we've become accustomed to through repetition, and another where something physical is changed. With the second case of the wall, how much our hair bends as we walk by is affected by a number of parameters. For example, we could change our walking speed or our distance from the wall. If we fix our walking speed, and vary our distance from the wall, then our hairs deflect more or less from the presence of the wall depending on whether we are closer or further from the wall. In fact, we can determine a rough size of an obstruction we are passing by as walking past a wall or a past a pole at the same distance and at the same speed will deflect our hair by different rates and amounts. We as humans are extremely fortunate that we have other senses that we can couple with our mechanical sensing capabilities to gain a much clearer understanding of our surroundings. Copepods do not have such a luxury as they are only equipped with much simpler sensing mechanisms. Similar to the example with the wall, obstructions do cause disturbances to the background generated flow field by the copepod. The issue that arises is that, like our hairs, how much their setae bend is dependent on their distance and the size of the obstruction. This was brought to light by Okubo and Yen in a pair of papers when investigating the copepod's sensory capabilities through deflection of the setae through a pressure gradient induced by a spherical object (Yen and Okubo 2002). What they discovered is that if such a signal is used to detect physical obstructions then the size of the object plays a huge role. Akin to being able to tell the difference between a wall and a pole, the copepod should be able to distinguish the difference between a large and small particle but if the particle is sufficiently large, then it is difficult to tell if the disturbance from a huge particle and a wall.

The main difference between the two modes of detection are the length scales in which each plays a role. Chemical signals advecting with the water may be useful for detecting food sources in the far-field. This would alert the copepod to the presence of its prey, but only gives the the animal a general direction. It would then have to follow the signal to get into a closer vicinity by following an increase in the chemical concentration. On the other hand, mechanical reception would be good for sensing things in the near-field. Obstructions cause disturbances to background flow fields, from which the copepod may be able to determine, compared to a chemical trail, a more accurate location of its food source. Regardless of which serves as the primary mechanism, sensing of food is a fundamentally important step in feeding. To date, it is still not fully understood. But the mystery into their roles in feeding could be uncovered through the use of mathematics by developing a model that captures some of the important aspects of the fluid flow generated by a feeding copepod.

1.3 Copepod Anatomy

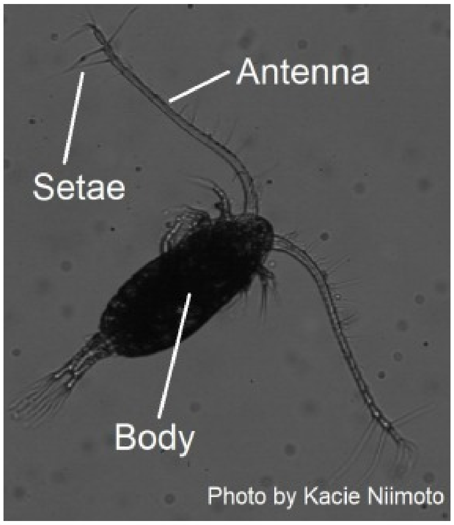

Figure 1.3: Image of a copepod courtesy of Kacie Niimoto

Copepod's are microcrustaceans part of the arthropod phylum. A simplistic view of their anatomy reveals a cylindrical body comprised of a prosome (upper) and urosome (lower), see figure 1.3. Their head and body are contained within the prosome, while their tail is part of the prosome. They have a pair of long antennae that extend perpendicularly from the base of their head similar to a shrimp, but with much thicker and rigid antennae. Along their prosome are various types of appendages for use in swimming and handling of objects. The tips of the appendages have a fan-shaped structure of smaller rods whose functionality is similar to that of our fingers. Along their appendages and antennae are thin rod-like hairs used for chemo- and mechano-reception.

1.4 Feeding behavior

The ocean is filled with large number of animals that feed in different ways. To begin with, some are predators while others are grazers. Some actively search out mobile prey, while others are opportunistic and scan the surrounding waters for potential sources. Similarly, a copepod's feeding behavior varies from species to species. There are four main groups that we can categorize them by- passive ambushing, active ambushing, feed-current feeding, and cruise feeding (Kiørboe 2011a). Both types of ambushing feeders rely on the prey-generated disturbances to the ambient flow field whereas the latter two types of feeders rely on their own generated flow fields in order to create the opportunity to sense a disturbance. The focus of this paper will be on the latter of the two groups where the animal senses its food source by disturbances to its own generated flow field.

For these types of feeders, a primary food source is marine snow. This is organic matter that sinks downward, hence the name, such as algal cells which range in size on the order of millimeters. The distribution of the cells within the surrounding waters varies, but it is accepted that the ocean is a rather barren environment. In the chance that a feeding copepod encounters its food, a feeding behavior is initiated with the intent of overcoming the obstacles that the viscous environment presents that is outlined in the previous section.

For feed-current feeders, we can further split the group based on the basic mode that is employed. Both groups create their own feeding current, but the way the food is captured differs between the two. This divide comes from how the copepod treats possible food sources. On one hand, we have filter-feeders. As the name hints, these are copepods that use their fan-like structures along their appendages to sieve the water. In doing so, all types of matter are collected with no discretion. This type of motion collects everything that comes into close vicinity similar to a net. On the other hand, there are copepods that beat their appendages at high frequencies to effectively overcome the sticky viscous environment and draw particulate matter from the surrounding area to a close vicinity of the body (Bundy and Vanderploeg 2002).

Once the copepod has overcome the obstacle of bringing the food source near its body, the next challenge is to direct the food to its mouth. In a viscous environment, the difficulty is compounded as particles near the body are difficult to maneuver around the body. Generally, feeding appendages are used to guide the food source from the capture region to the mouth in which the copepod determines the quality of its possible food source (Koehl 1981; Price et al. 1983). Particles are brought to the mouth where it is inspected by taste. Things that are recognized for food are consumed while the rest are rejected and ejected from the body. The whole process of how this group of feeders eat can be summarized by familiar processes of a factory line. Products on conveyer belts are much like trajectories in which particles traverse to be brought to someone for the purpose of quality control. Products that pass a level of quality are accepted while those that don't are rejected.

In order to feed, any animal needs to be able to, at the very least, sense its food, maneuver to it and capture it in some manner. But this fundamentally relies on the presence of a food source. If the oceans were abundant in food sources, then the difficulty in sensing food can be relaxed as the opportunity to encounter its food would be certain. However, food for copepods is scarcely distributed throughout the water column making feeding an even more arduous task (Kiørboe 2011b). An interesting fact about copepod's is that as a collective species, they have one of the largest biomasses of all animals. If we step back and think about this, it begs a very perplexing question. How does an animal submerged in a highly viscous honey-like and barren environment maneuver through its surroundings to effectively sense and capture its food to such an extent that it gains such a large population? This would be similar to us walking throughout our house blindfolded trying to find food guided by our sense of smell and touch. It is our hope that aided by a mathematical models we can generate a clearer picture of the scenario and gain insight into their abilities by analyzing their ability to sense their food source through mechanical disturbances as well as capture and consume their food.

1.5 Mathematical Model

Much of our understanding in how copepod's interact with their surroundings is based on observations in such scenarios as prey encounters (Bundy and Vanderploeg 2002), actively swimming (Catton et al. 2007), foraging (van Duren et al. 2003), and escaping from predators (van Duren and Videler 2003). Experiments can be a good start in testing hypotheses about the copepod's abilities. However, it may be difficult to reproduce the exact conditions between experiments or to vary parameters. A mathematical model could go a long way in helping gain insight into copepod's feeding habits.

1.6 Mathematical assumptions

We will briefly introduce the mathematical assumptions made within our models. To begin with, capturing all the physical details of the copepod would certainly be impossible and quite computationally expensive. To make matters easier, we offer a much more simplified structure of the animal that still encapsulates the main details that are important with respect to feeding. This is separated by two scenarios. Sensing of neutrally buoyant spherical particles with a rigid boundary and manipulation of food when near the body of the copepod.

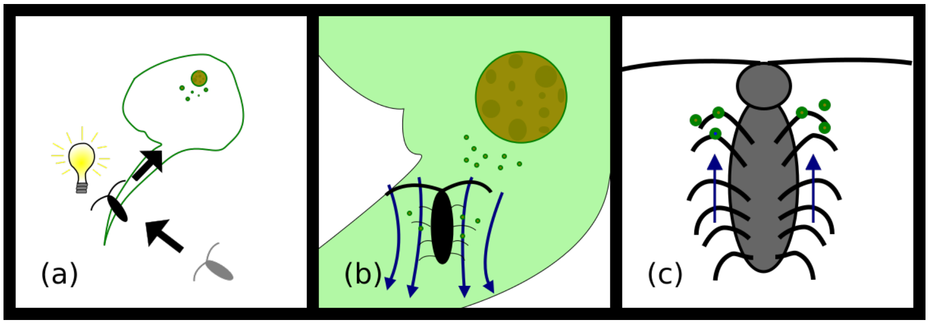

Figure 1.4: A sequence of events that we consider as the process of feeding. In (a) the copepod is swimming through the water column and passes through a chemical plume giving the copepod a general direction of its food source. (b) The copepod maneuvers itself in a prime location to draw the food source near its body. (c) Food near the body is directed upward toward the feeding appendage for inspection and consumption.

1.6.1 Sensing

Firstly, the copepod must sense its prey. In this scenario, we envision a copepod within the water column engaged in some mode of feeding, see figure 1.4(a). This may be a passive ambusher simply waiting to come upon its prey, an active ambusher swimming around in search of its prey, or a stationary feeder maintaining its position and drawing a current to itself. For the sake of simplicity, we categorize these three modes as sinking, swimming and hovering. Remote sensing is an event that takes place in distances sufficiently far from the animal. Thus, our assumptions are such to generalize the main features of the animal and its food. In this regards, we are not too concerned with the fine details of the flow field as the copepod flutters its appendages, but rather the general trends and behavior based on their movement.

The main features of the copepods are the pair of antennae, the body, and the appendages. Much of the copepod is covered in long hair like rods called setae whose primary role is for sensing stimuli such as chemical and mechanical signals (Alcaraz et al. 1980). For the purpose of capturing enough of the detail of the copepod's body, we view the antennae simply as a rod and the body as a single sphere. We disregard the presence of the copepod's appendages, but encapsulate the approximated flow due to the beating of the appendages by the introduction of a force vector. This force, which we will go into more detail later, can be imagined by considering the motion of the copepod within the water column through a time-averaged flow field. For a sinking copepod, this is one where the animal is not beating its appendages and so the averaged force vector should be zero. On the other extreme, a swimming copepod will be beating its appendages with a considerable force in order to overcome gravity, as well as the opposing drag force imposed by the fluid. A hovering copepod will fall somewhere between these two extremes, producing a force vector that is just strong enough to overcome the gravity and balanced by the drag.

As mentioned before, the copepod is covered in setae, which similarly to the appendages, we disregard. With regards to mechanical sensing, the action to which brings upon a neurological response, is the deflection of the setae (Strickler and Bal 1973). A motile food source produces its flow field through locomotion while a non-motile one moves with background flow. Both have an effect on the flow field generated by a feeding copepod that are qualitatively different. In our study, we restricted our assumptions to that of a non-motile prey. We further assume that they are spherical objects with a rigid boundary. Their presence alone distorts the background flow field as the rigidity of their surface resists the shear forces induced by the generated flow field. We measure the resultant disturbed velocity at prescribed locations along the copepod's antennae. If the signal is strong enough, then we consider the particles location a detectable location. To this end, we consider the locations in a plane that intersects the copepod directly though the antennae and body, as in figure 1.4(b).

The primary food source that we consider within this paper is algal cells which we make a rough approximation on the geometry as a sphere. While these cells vary in size, we consider a single radius of the cell on the order of one tenth the body size of a copepod. For the purpose of sensing, we consider a single spherical particle at a particular location within the plane at a time, compute the resultant disturbance velocity and then determine if the produced signal is detectable or not.

1.6.2 Flow between feeding appendages

A second feature of the model described above is the induced background flow produced by the copepod engaged in the three feeding modes. Firstly, this allows us to see the general trajectories that the flow takes around the copepod. This provides information as to what effect the copepod has on the surrounding area around its body as it feeds and allows for a comparison between the three modes of feeding. It also provides a glimpse into understanding what can be sensed throughout time. Previously described is the method employed to determine a detectable region surrounding the copepod with particles located in a plane that passes through the copepod's antennae and a body. By utilizing the same concept, but except by considering a perpendicular plane, we can combine both a new perpendicular detectable region that intersects the body of the copepod and use backward integration to obtain a detectable volume. This provides valuable insight into what the copepod can sense over *a period of time*, rather than just at an instance. What we will show in subsequent chapters is that the three modes of feeding produce widely different characteristics. This proves to be a very interesting find. Not only do these detectable regions differ wildly, but it allows to us to determine scenarios in which one mode of feeding becomes much more advantageous than another.

For the final analysis of our project, we consider the last part of the problem with feeding we described previously. That is, once the particle is near the copepod, how does it direct it towards its mouth, see figure 1.4(c). For this scenario, we do not consider any particular mode of feeding and instead assume that the food particle has traversed its way to the feeding appendages. As stated before, the appendages pivot upon joints producing a fling and clap motion that mimics that of insects and bird wings that produce flight (Strickler 2019; Lighthill 1973). This allows for two degrees of freedom which overcomes the difficulties demonstrated by the scallop theorem, and produces non-reciprocal motion. For this part of the study, we simply consider what part of the fluid is influenced due to the presence of the moving feeding appendages. The body and antennae of the copepod are completely disregarded and only a single pair of feeding appendages are considered in or model. The curvature of the copepod's arms are also completely ignored. Instead, we simply view them as slender rods. We approach this scenario in two different frames of mind. First, we disregard the influence that the movement of the arms would have in a three-dimensional frame and instead consider the pair of arms as two line segments that extend infinitely in an orthogonal plane. For this model, we employ the use of lubrication theory by assuming that the length of the arms greatly dominates the gap in between them. However, there are a few shortcomings of this approach. Firstly, we can only consider the dynamics strictly encased within the lengths of the walls and the the widths obtained by line drawn between corresponding tips. The second approach that we take is to consider the appendages as a pair of slender rods. By doing so, the appendages are approximated by a pair of cylinders that again oscillate in the same fling and clap motion described above. This allows for a much clearer picture and analysis on the flow due to the pair of appendages as it firstly takes into account the dynamics due to the pair of appendages in a three dimensional space.

The fling and clap motion has been studied in a variety of cases for animals operating at a higher Reynolds number such as small insects. In those cases, the environment is quite different as inertia plays an important role. At a low Reynold's environment, the dynamics are quite different. To date, there have only been observations of the motion of the appendages. Providing a simplified mathematical model could be a good step in the direction of providing answers to some of the phenomena observed under a microscope.

1.6.3 The Navier-Stokes equations

The governing equations of any fluid flow are given by a pair of differential equations known as the Navier-Stokes equations. The momentum equation is given by

$$\rho\left(\frac{\partial \mathbf{u}}{\partial t} + (\mathbf{u}\cdot\nabla)\mathbf{u}\right) = -\nabla p + \mu\nabla^2\mathbf{u}, \tag{1.2}$$

where $\mathbf{u}$ is the velocity of the fluid, ρ is the fluid density, μ is the fluid viscosity, and p is pressure. The continuity equation is given by

$$\nabla\cdot\mathbf{u} = \mathbf{0}. \tag{1.3}$$

If we non-dimensionalize the equation using the introduced variables

$$\mathbf{u} = U\tilde{\mathbf{u}}, \quad p = \frac{\mu U}{L}\tilde{p}, \quad \nabla = \frac{1}{L}\tilde{\nabla}, \quad t = \frac{L}{U}\tilde{t}, \tag{1.4}$$

with characteristic velocity and length, U and L, we then obtain

$$\mathrm{Re}\left(\frac{\partial\tilde{\mathbf{u}}}{\partial\tilde{t}} + (\tilde{\mathbf{u}}\cdot\tilde{\nabla})\tilde{\mathbf{u}}\right) = -\nabla\tilde{p} + \tilde{\nabla}^2\tilde{\mathbf{u}}. \tag{1.5}$$

Here, we see that the Reynolds number Re plays a significant role in determining the importance of either side of the equation. For scenarios in which we are accustomed to, high Reynolds number flow, the left hand side of equation (1.5) typically plays a more significant role and dominates over the right-hand side. On the other hand, at a microscopic viscous flow field, the Reynolds number tends to 0. In this limiting case, known as the Stokes regime, viscous forces dominate inertial forces. A simplification of the Navier-Stokes equation commonly used in these situations is to approximate the Reynolds number Re as zero. Explicitly, this is given by

$$\begin{cases} -\nabla\tilde{p} + \nabla^2\tilde{\mathbf{u}} = \mathbf{0} \\ \nabla\cdot\tilde{\mathbf{u}} = 0 \end{cases} \tag{1.6}$$

In the experiment described by the two oscillating slender rods, particles that were near the rods tended to move in conjunction with the motion of the rods. This exemplifies a common boundary condition, called the no-slip condition, accompanied with the Navier-Stokes equation. To put it plainly, the flow along the boundary of a solid object moves with the boundary. If we change the frame of reference to match that of a moving body, then the fluid flow is essentially zero along the body. If $S \subset \mathbf{R}^3$ is a parametrization of the body, then $\tilde{\mathbf{u}} = \mathbf{0}$ along ∂S.

The reduction of the full Navier-Stokes equations in (1.5) to the Stokes equations in (1.6) is a very nice feature. For instance, the Stokes equations are linear differential equations and in certain cases can be solved to produce analytical solutions. In future chapters, we will describe several of these solutions and how they are utilized to model the copepod's motion along the fluid.

1.6.4 Reynolds Number

The Reynolds number in equation (1.1) can be interpreted as a ratio between the types of forces at play in a fluid flow,

$$\text{Re} = \frac{\rho U L}{\mu} = \frac{\text{inertial forces}}{\text{viscous}}. \tag{1.7}$$

This dimensionless number determines the importance of the forces in play. For example, the aquatic scenarios we are familiar with involving larger marine animals such as dolphins and sharks take place generally where the Reynolds number is large, $\approx O(10^5)$, whereas a generic Reynolds number of the flow of a feeding copepod would be somewhere on the order of $\text{Re} < O(1)$. The determining factors here are the values of U and L in equation (1.1). That is, fixing the fluid density of seawater at 20° C as $\rho = 10^3$ kg m^3 and viscosity $\mu = 10^{-3}$ kg s for both situations, leaves the characteristic length and velocity scales as parameters which determine Re. Quite clearly, both U and L differ in magnitude in both cases of a large fish and a copepod.

The dynamics that take place between the two polar ends of the Reynolds number are physically drastically different. In a high Reynolds number flow, the extreme side that we are used to, the flow field can appear to be quite turbulent. In a pool, as we drag our arm through the water, the fluid surrounding our arm bends around the contour of body. The water swishes and swirls in a way that is difficult to discern. Whereas, in a lower Reynolds number flow field, the fluid is much more viscous with a consistency like honey. While it is certainly true that a low Reynolds number flow field is not characterized by one absent of chaotic flow, the way the fluid moves is somewhat more clear. In a high Reynolds number flow, inertial forces play an important role. The flow field is propelled not only by actions that are taking place at the moment, but also continues to move through the acceleration caused by the motion. In a low Reynolds number flow, this is not the case. Similar to the experiment with the slender rods, when the motion has concluded, the fluid also stops moving.

1.7 Dissertation layout

For the remainder of this dissertation, I will recount in detail the steps in my research. The material will be presented in the order that physically takes place in nature. First I will discuss our model for sensing of spherical particles. Then, discuss the model used for manipulation of particles between a pair of feeding appendages. In each case, I will present the physical problem in more detail, some of the assumptions that were utilized to acquire a mathematical model, and the results of the mathematical model. When applicable, I will also compare our work with material that is within present knowledge and the ramifications of the results of my work.

Chapter 2

Sensing of Spherical Particles

Copepods are an important player in aquatic ecosystems as they help break down particulate matter such as marine snow, detritus and other organic matter. Their feeding strategies vary from species to species with some acting as ambushers who actively swimming through the water column to attack their prey, while others employ a different method by instead bringing the food source to themselves through a feeding current. There is, however, something unobservable at play in either of the two modes of feeding. The creatures lack the ability to discern much visibly except perhaps the presence of light, and so it must rely on other senses and cues to alert it to potential food sources. Therefore, feeding becomes much more complex for these animals as it is a multistage process that not only requires the capture of food, but also the necessity to sense it in the first place. There are several different types of signals that a copepod is able to detect, such as chemical trail and mechanical disturbances to the fluid (Alcaraz et al. 1980). The research I've been working on focuses on the latter and its implications under specific conditions and parameters of its prey. In this paper, I will discuss the background physical problem, the creation of our mathematical model, and then compare our study with others works and further implications as a contribution to the community.

2.1 A history on previous work

At the size of a few millimeters, copepods live in a highly viscous environment. The Reynolds number at this scale is very small, and while when we humans generally think of interactions within big bodies of water as being very easy to maneuver within, the environment for microscopic creatures is much different than what our intuition tells us. The fluid environment at their scale is less like water and more like that of honey. Simple functions such as locomotion require motions that are counter-intuitive to what we as humans living at a much larger scale may quickly assume to be possible to produce movement. This is probably best described by the scallop problem posed by E.M. Purcell in his 1977 paper titled *Life at low Reynolds number* (Purcell 1977). The problem posed is for a scallop-like creature whose only motion is the opening and closing of its mouth as a means for locomotion. The issue here is that at low Reynolds number, inertial forces are dominated by viscous forces and so any translation produced by quickly closing its mouth to displace the fluid occupying it in a jet-like motion would be completely cancelled out when the animal opens its mouth to complete another cycle. This paradox here is known as reciprocal motion. Running the sequence of opening to closing of its mouth forward in time produces the same animation as running the sequence in reverse. That is, the motion is invariant under time-reversal. This example demonstrates that our understanding of the dynamics at work at low Reynolds number requires a different perspective than what we may quickly assume to be true.

Anatomically, copepods share many characteristics to shrimp. Their body is made up of a prosome and a urosome and are roughly ellipsoidal in shape. They have a pair on long antenna located at the head that are aligned with both chemo- and mechanoreceptors. Along their their body are numerous appendages used for various purposes. For example, the herbivorous Calanoid copepod have appendages used for filtering, feeding, and swimming. For such copepods as these that feed on algal cells, they cyclically beat their feeding appendages to generate a feeding current which drives the nearby fluid around the body to the filtering appendages where potential food is gathered. Their ability to manipulate the feeding current is so well developed that if a desired particle is on a trajectory out of its grasp, it can redirect the particle by relocating itself to draw in the particle through its feeding current (Jiang et al. 2002b). Until a pivotal paper by M.A.R. Koehl in 1981, the belief within the community was that at this point, the fluid would simply be pushed through the filtering appendages, capturing everything everything entrained in the flow. However, observations at this step showed a different behavior. At the stage when the fluid enters the vicinity near the filtering appendages, the fluid is inspected and possible food sources are selectively picked (Koehl 1981). This key observation shifted the communities beliefs about how some copepods feed from animals that mindlessly searched for food to those who were actively and selectively probing the water column for their food.

Up until Koehl's paper in 1981, there were many observations of the flow field around a copepod engaged in various modes. One of the earliest accounts is by H.G. Cannon in the 1920s where he noted in particular detail the currents that surrounded the anterior of a swimming copepod as it beat its appendages (Cannon 1928). Of particular interest are the vortical motion of the fluid that swirled under the copepod but near the body which he called the "swimming vortex." The fluid would swirl near the body pass from head to tail and outward in, drawing the flow around the body before ejecting it downward to produce thrust. He also noted another vortex that appeared to run in the opposite direction of the aforementioned vortex which he called the "feeding vortex" as it brought the flow near the mandibles located by the copepod's mouth. This, he states, was a byproduct of the first vortex mentioned. The importance of this discovery documented here is that it was one of the first accounts to qualitatively analyze the general flow pattern of a copepod. He summarizes that the flow for a swimming copepod could be thought of as a thick cylindrical tube in which the inner radius held the body of the copepod and in between the inner and outer radius was where the vortical motion and ejection of the fluid took place.

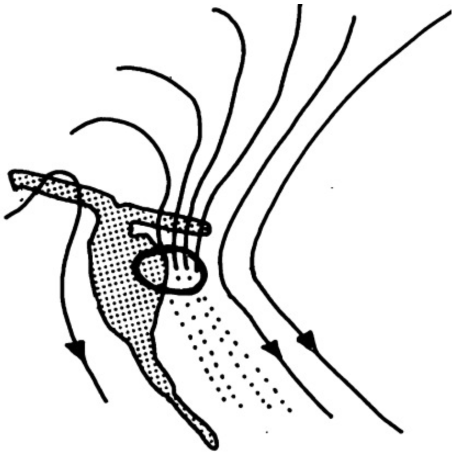

Figure 2.1: A drawing of the capture area and feeding current around a copepod. Image taken from (Strickler 1982)

One of the first to model the feeding current generated by a feeding copepod is Tiselius and Jonsson. In 1990 they published a paper on their observation of six copepod species that fed in three different modes: sinking, swimming, and hovering (Kristineberg Marine Biological Station and Sweden 1990). Motivated by their visual data, they developed mathematical models for each of the three modes. For a copepod that sinks or a swims, the body is approximated by a sphere matching the copepod's radius and the flow is modelled as the velocity field generated by a sphere translating in the appropriate direction. For a hovering copepod that generates a flow by pumping the fluid from its anterior and out its posterior, the flow is captured by a Stokes point force solution, that is a Stokeslet solution, with a downward pointing force vector matching the gravitational force due to its weight, when viewing the species from a top-down dorsal viewpoint. They also reported on the advantages of each mode based on the required energy to perform each action. There is a key apect of the flow for each mode here should be noted. The sinking and swimming copepod is modelled by a translating sphere. Viewing the sphere from above and through the translational vector produces an axisymmetric flow, that is, flow that is invariant regardless of any plane of reference that intersects the translational vector. This is also true for the hovering model as well since the Stokeslet solution can be realized as the flow due to a translating sphere in the limit as the radius of the sphere goes to zero. These approximations of the body as a sphere inherently neglect physical features of the animal that breaks such symmetry to produce a flow that had been previously reported as non-axisymmetric (Cannon 1928). Malkiel et al modelled a similar behavior seen in a sinking copepod (Malkiel et al. 2003). In 2003, they observed a copepod sinking under its own weight while beating its appendages to generate a feeding current. They noted that while the copepod simultaneously sank and beat its appendages, a stagnation point in the flow would form above the copepod's body. The animal would perform this for roughly nine seconds before jumping upward to the stagnation point in order to capture the accumulated particulate matter and then continue the cycle again. To model this behavior, they used a single translating Stokeslet with a downward force vector. This again produces and axisymmetric flow which neglects the effects of the copepod's body on the surrounding fluid.

Visual observations, however, have shown that the flow around a copepod is not axisymmetric. Jiang et al developed theoretical (Jiang et al. 2002c) and numerical (Jiang et al. 2002a) models for a copepod engaged in a variety of movements such as sinking, hovering, and swimming in multiple directions and speeds. The body of the copepod was approximated as a single sphere while the antenna's geometry is not considered. The motion of the fluid due to the beating of the appendages is captured as a point force located outside the sphere and the flow is computed such that the no-slip condition holds along the boundary of the sphere. While not only providing a fresh look into a non-axisymmetric flow field around a copepod, they also formulated and analyzed specific volumes of the surrounding fluid near the copepod. Forgoing any physical implications due to the copepod's ability to sense its surroundings, the authors concluded that in order to capture a particle, the particle needs to end up in a two dimensional shape near the mouth of the copepod which they refer to, after Strickler (Strickler 1982), as the ”capture area” - a region near the head of the copepod where it can easily direct the particle to its mouth, see figure 2.1 (Jiang et al. 2002a). By evolving time backwards, a three dimensional subset of the surrounding fluid is generated. As an increasing function of time, the volume describes how much of the fluid is inspected. The capture zone has been further investigated under different circumstances such as varying the feeding mode (Jiang and Strickler 2007), a tethered copepod (Jiang et al. 1999), a positively buoyant copepod (Jiang and Strickler 2005), or using chemoreception thresholds (Jiang et al. 2002b). Although these studies do not specifically consider the copepod's mechanoreception capabilities, they do provide insight into understanding what region of the surrounding fluid that a copepod could theoretically sense.

The background flow generated by a feeding copepod is one important aspect in understanding how they feed, but is only half of the total problem. This is highlighted by J. Rudi Strickler in his 1985 paper *Feeding Current in Calanoid Copepods: Two new hypotheses* (Strickler 1985) where, based on previous observations (Cannon 1928; Alcaraz et al. 1980; Andrews 1983), delves broadly into various aspects of the feeding current and brings up a very important point with regards to locating algal cells. While it is certainly true that in order to feed, the copepod must bring the food to itself in order to ingest it, but the other side to the question is: how does it know where the food is? The common belief is that it is a chemical signal that which first alerts the copepod to potential food. An algal cell leaks a chemical forming what Strickler refers to as an active space around the algal body. The chemical signal is then advected along with the fluid flow generated by a feeding copepod and, provided that the signal is detected, elicits a feeding behavior in which the copepod redirects the flow to draw the fluid near its body. Another significant characteristic in identifying the copepods ability to feed is pointed out in this paper. The flow field generated by a feeding copepod funnels the flow from above the copepod down past it in a cylindrical shape similar to that illustrated in Cannon's work.

Strickler's 1985 paper brought to light many interesting questions that the community looked to answer. In particular, the primary mechanism used in remote detection of algal cells in the surrounding fluid. In recent years, this sparked a debate within a portion of the scientific community interested in copepod sensory mechanisms with some claiming that chemoreception is responsible in detecting food sources in the near field while others argue that the rate of diffusion of a chemical signal would be too slow in order for the copepod to accurately locate particulate matter (Goncalves and Kiørboe 2015; Kiørboe and Jiang 2013; Kiørboe and Visser 1999; Kiørboe et al. 2016; Paffenhöfer and Jiang 2016; Price 1988). Advocates of the latter theory believe that mechanorecption plays the primary role in remote detection for food sources near copepod body. Many have studied the role of mechanoreception in copepods and formulated mathematical models of varying complexity to explain and illustrate the range and capabilities of such a mechanism.

The first group to provide an answer to the copepod's hydromechanical sensing abilities was Legier-Visser et al in 1986 (Legier-Visser et al. 1986). The scenario in their study is described as a particle entrained in a laminar shear flow located directly above the copepod antenna that would exert a force on the fluid through a pressure differential with a magnitude on the order of the background velocity scale. In 2002, Yen and Okubo (Yen and Okubo 2002) published a follow up paper to correct the 1986 paper (Legier-Visser et al. 1986). In particular, they noted an oversight in the choice of the velocity scale and corrected it by instead scaling the pressure differential by a characteristic velocity scale due to that of a sphere sedimenting under its own weight following Stokes drag law. In a more recent paper, Giuffre et al observed the flow field of a freely swimming feeding copepod (Giuffre et al. 2019). They observed that the food particles entrained in the feeding current followed the trajectory of the flow, but at a lagged rate. In their model, the flow oscillates back and forth sinusoidally while the particle trajectory is assumed to follow the streamlines with a lag shift. The strength of the signal was measured as the maximal difference between the particle trajectory and the trajectory of a fluid element centered at sphere in a flow absent of the presence of the particle. The sensing mechanism in these three papers rely on a fundamental assumption on the particle. Specifically, that the density difference between the particle and the fluid is assumed to be large enough to exert a force on the fluid. In doing so, they assume that the particle will accelerate and decelerate along the fluid elements trajectory, thus producing a distortion to the background flow. However, as Riley and Maxey point out (Maxey and Riley 1983), this is only possible if a spherical particle has a substantial density difference with the fluid. Regardless of how the particle's density difference is treated, the measurement of the signal is intimately linked with the background flow field as they are included in the calculation.

The density difference, however, between the surrounding fluid and an algal cell is very small. Other groups have looked into the hydromechanical signal due to a particle with negligible density difference with the surrounding fluid entrained in a copepod's feeding current. Bundy et al considered the role of the antenna in sensing mechanical disturbances as a swimming copepod approached a stationary particle (Bundy et al. 1998). To study the strength of the signal, a background shear flow with two cylinders of largely different radii are situated perpendicularly to the flow and numerically simulated as the smaller cylinder approaches the larger in the reference frame of the moving copepod. However, there were some crude approximations made in their model. Firstly, the influence due to the copepod's body on the surrounding flow is completely neglected as the body is not considered in their model and only the antenna is modelled as an infinitely long cylinder perpendicular to the background flow. Secondly, a particle is approximated by a smaller cylinder which physically exhibits a different effect on the surrounding flow than a sphere. Lastly, if considering the entire space as a three dimensional object, horizontal planes that slice through both cylinders are identical. This effectively reduces a three dimensional flow field into a two dimensional one and disregards the dynamics that take place in the perpendicular space.

In a similar light, Visser investigated the hydromechanical signal due to the disturbance flow generated by a spherical particle entrained in the background flow of a copepod's feeding current (Visser 2001). He models the background flow field of the feeding copepod by a Stokeslet with a force vector in the direction of gravity. For the particle, he assumes that it is neutrally buoyant and located at a distance directly above the copepods head. The disturbance velocity field generated by the particle is modelled by a stresslet solution and is measured at a single location, which he assumes to be at the tip of the copepod's head. There are some key assumptions here that distinguish his study from previous studies which provides a more realistic analysis of the copepod's mechanical sensing than previous works. By assuming that the particle is neutrally buoyant implies that the density difference between the fluid and the particle is essentially zero. This, coupled with the assumption that the surface of the particle is rigid means that the particle moves with the fluid at the same velocity. Because the body advects with the background flow, the rigidity of the particle deforms the streamlines that locally surround the surface which applies stress and strain on the surrounding fluid which up to a first approximation mimics the flow due to a stresslet. However, some aspects of the copepod's geometry are neglected. For instance, the background flow is again modelled axisymmetrically by a Stokeslet solution and the copepod's geometry is completely ignored. Furthermore, his analysis of sensing capabilities accounts for only a single sensory location at the tip of the copepod's head, which is not entirely accurate as the copepod's antenna are aligned with a number of setae.

Each of the authors work outlined in the previous few paragraphs contribute a substantial amount of information in their analysis of the overall problem in the search for an answer to the copepod's mechanical sensing capabilities. Yet, as with all mathematical models, certain approximations are made that inherently neglect influences from various aspects such as the copepod's shape and sensory locations. Our work looks to build upon the previous works by filling in some of the gaps in knowledge by building upon the works of previous authors. We will analyze the flow field of a copepod engaged in three modes of feeding; a copepod sinking under its own weight, a copepod swimming in the opposite direction of gravity, and a stationary copepod that hovers in the water. The geometry of the copepod will be approximated by a series of regularized Stokeslets. The body will be approximated by a single regularized Stokeslet and the antenna by a rigid row of spheres. The setae's influence on the flow will be neglected, but sensors will be assumed at the location of each antenna Stokeslet. Finally, we will measure the strength of the disturbance velocity of particles arrayed in various planes around the copepod and analyze the ramifications of our results.

2.2 The physical problem

The aquatic environments that copepods generally inhabit are many orders of magnitude larger than themselves and, additionally, is not abundant with food (Kiørboe 2011b). Consequently, these animals are tasked with the daunting challenge of scavenging a barren environment for whatever it can find. However, copepods have one of the largest biomasses among all creatures in the animal kingdom. As all organisms require food in order to survive, the sheer vastness of their population points to their abilities and effectiveness in their feeding strategies.

To date, their are four main types of strategies employed by copepods: passive ambushing, active ambushing, feed-current feeding, and cruise feeding (Kiørboe et al. 2014; Kiørboe 2011b). The first two types of feeders rely on perceiving hydromechanical signals due to motile prey, while the latter two are focused on prey that are encountered due the motion and deformation of the water by the copepod. In this paper, we will focus on the second of the groups mentioned above. The two types of feeders are similar in that they sense their prey using their due to their own action on the water and differ in that feed-current feeders tend to remain stationary while cruise feeders, as their name indicates, actively move through the fluid with the intention of encountering its prey. For our research, we view the prey similarly for both types of feeders as inert spherical in shape.

What we mean by inert is that the particle is non-motile and produces no chemical signal, thus any signal produced by such a particle would be due solely to its own presence in the water column. We further assume that the particle has a rigid boundary, meaning that the surface of the spherical object resists deformations induced by any shear stresses to maintain its shape.

2.3 Mathematical model: The flow field

The signal we use in our research is generated by the presence of a non-motile spherical particle with a rigid boundary and is computed following Faxen's third law for a sphere (Takagi and Strickler 2020). The magnitude of the signal is intimately linked with the background flow field of the feeding copepod. In order to produce the fluid velocity for the three feeding modes, a few approximations on the copepod geometry are necessary to simplify calculations. At first glance, we can simplify the major attributes of the copepod's anatomy as a pair of simple geometric shapes.

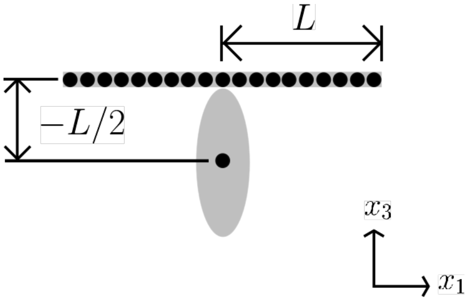

Figure 2.2: Simplificaton of the copepods anatomy. The antennae are approximated by a single rigid rod which is modelled as a row of spheres. The elliptical body is also simplified to a single sphere centered at midpoint of the ellipsoid. The row of spheres for the antennae are aligned along the horizontal x_1-axis while the body sphere aligns with the midpoint of the antennae along the x_3-axis.

Firstly, the antennae are a complex structure with numerous setae that protrude outward. The bending of the setae is the mechanism used to sense the surrounding water, but it adds additional structure. We ignore the setae and simplify the antennae by representing it as a long rigid cylinder. The body is also quite complex with various appendages that extend around an ellipsoidal shape. Here, we make an assumption following previous works (Malkiel et al. 2003; Visser 2001; Kristineberg Marine Biological Station and Sweden 1990) and represent the body as a single sphere. In total, we view our model as simply a long rigid cylinder representing the antennae with a sphere located below the midpoint of the major axis. The image below, figure 2.2, depicts the distribution of spheres described. The length of a single antenna is obtained by approximating the length from images from previous studies ranging between $1 - 1.5$ mm. For simplicity, we've taken this length to be $L = 1$ mm and followed similarly for the length of the body. The row of spheres approximating the antennae are aligned along the horizontal x_1-axis between $x_1 = \pm 1$ and the body sphere lies along the vertical x_3-axis.

2.3.1 The model

With the approximated geometries described above, we produce the flow fields using the method of regularized Stokeslets (Ainley et al. 2008; Cortez 2018, 2001; Cortez et al. 2005; Gimbutas et al. 2015; Nguyen et al. 2014). This technique has been used in a variety of ways by discretizing the geometry of bodies and objects and distributing regularized point forces to produce flow fields based on the movements of such bacteria locomotion due to flagella (Hyon et al. 2012) and other microorganisms with slender and flexible appendages (Nguyen et al. 2014), and the bending of setae due to the presence of a spherical particle entrained in a generic background flow field (Shen and Fu 2020). Essentially, we discretize the approximations of the cylindrical antennae and ellipsoidal body by a series of small spheres that, unlike the traditional Stokeslet solution, take into account a physical boundary around the spheres. In general for a single regularized Stokeslet located at $\mathbf{z} \in \mathbb{R}^3$, the fluid velocity at a point $\mathbf{x} \in \mathbb{R}^3$ can be represented as

$$\mathbf{u}(\mathbf{x}) = \mathbf{K}\mathbf{F} \tag{2.1}$$

where $\mathbf{F}$ is the force vector on the fluid by the sphere and $\mathbf{K}$ is the regularized Stokeslet kernel given by

$$\frac{1}{8\pi\mu}\left[\frac{(r^2 + 2\delta^2)}{(r^2 + \delta^2)^{3/2}}\mathbf{I}_3 + \frac{\mathbf{r}\mathbf{r}^T}{(r^2 + \delta^2)^{3/2}}\right] \tag{2.2}$$

where μ is the fluid's dynamic viscosity, δ is the radius of our sphere, $\mathbf{r} = \mathbf{x} - \mathbf{z}$, and $r = |\mathbf{r}|$. This yields a linear relationship between the fluid velocity $\mathbf{u}$ and the force vector $\mathbf{F}$. Thus, knowing one of the values allows us to solve for the other. The transition from calculating the fluid velocity induced by a single regularized Stokeslet to the fluid velocity generated by n regularized Stokeslets is represented by a linear combination of the velocity of each individual Stokeslet where the interactions between Stokeslets must be taken into account. That is, for n Stokeslets with Stokeslet location in

$\mathbf{Z} = \{\mathbf{z}_1, \mathbf{z}_2, \ldots, \mathbf{z}_n\} \subset \mathbb{R}^3$, the fluid velocity at the point $\mathbf{x} \in \mathbb{R}^3$ is given by

$$\mathbf{u}(\mathbf{x}) = \sum_{i=1}^{n} \mathbf{u}_i(\mathbf{x}) = \sum_{i=1}^{n} \mathbf{K}_i \mathbf{F}_i \tag{2.3}$$

where $\mathbf{F}_i$ is the i-th force vector and $\mathbf{K}_i$ is the i-th regularized Stokeslet kernel where

$$\mathbf{K}_i = \mathbf{K}(\mathbf{x}, \mathbf{z}_i) = \frac{1}{8\pi\mu} \left[\frac{(r_i^2 + 2\delta^2)}{(r_i^2 + \delta^2)^{3/2}} \mathbf{I}_3 + \frac{\mathbf{r}_i \mathbf{r}_i^T}{(r_i^2 + \delta^2)^{3/2}} \right] \tag{2.4}$$

where μ is the fluid's dynamic viscosity, δ is the radius of our sphere, $\mathbf{r}_i = \mathbf{x} - \mathbf{z}_i$, and $r_i = |\mathbf{r}_i|$. As stated above, this also follows a similar scheme as knowing a combination of the forces or the fluid velocity at the locations of the regularized Stokeslets beforehand will allow us to solve for the unknown quantities by utilizing the linear relationship between the forces and the fluid velocity.

2.3.2 Force vectors at play

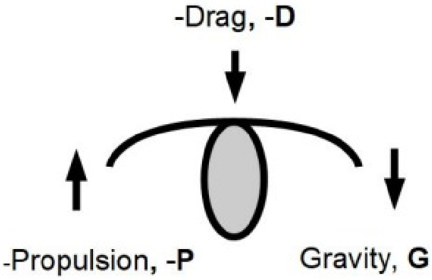

Figure 2.3: Diagram of the force vectors acting on the copepod.

The three modes of feeding we focused on during our research envisioned a copepod swimming through the water column, sinking passively downward, and hovering. These three scenarios produce three differing physical situations with varying parameters on the forces and fluid velocity. However, each mode relies on an underlying force balance on the copepod's body and ultimately there are three dominant forces acting on the copepod, see figure 2.3. Firstly, it experiences a downward gravitational force $\mathbf{w}_{\text{excess}}$ induced by a density difference between the copepod and the water. Secondly, as the copepod beats its appendages against the water to produce propulsion, the body experiences an equal and opposite force by the water, which we call $\mathbf{g}$. Lastly, as the copepod produces propulsion, the body also feels a drag force $\mathbf{f}$ in the opposite direction of translation. The sum of these three forces yield the force balance equation on the body given by

$$\mathbf{w}_{\text{excess}} - \mathbf{f} - \mathbf{g} = \mathbf{0}. \tag{2.5}$$

As a matter of convention, we take the negative of the drag and propulsion vectors to represent the force that the spheres produce on the fluid. It is important to point out that this is the total force acting on the copepod's body and not the forces acting on the fluid. This produces the following modified force balance equation which takes into account only the propulsive and drag forces acting on the fluid with the sum being the excess weight:

$$\mathbf{f} + \mathbf{g} = \mathbf{w}_{\text{excess}}. \tag{2.6}$$

.

In all three modes, the first of the forces, $\mathbf{w}_{\text{excess}}$, is the same and is computed similarly to previous works by previous authors (Malkiel et al. 2003; Jiang et al. 2002c). We use the measurements made by Malkiel et. al. to obtain a density difference between the copepod and the fluid as $\Delta\rho = 6.7\,\text{kg m}^{-3}$. The approximated volume of the cylindrical antenna is calculated using the radius $r_c = 0.1\,\text{mm}$ and length $2L = 2\,\text{mm}$ to compute the volume as $\Omega_{\text{cop}} = 6.3 \times 10^{-11}\,\text{m}^3$. With the gravitational force vector $\mathbf{F}_{\text{grav}} = -9.8\,\text{m}\,\text{s}^{-2}\mathbf{e}_3$ where $\mathbf{e}_3$ is the unit vector in the x_3-direction, the excess weight is computed as

$$\mathbf{w}_{\text{excess}} = \Delta\rho \cdot \Omega_{\text{cop}} \cdot \mathbf{F}_{\text{grav}} = -4.1 \times 10^{-9}\ \text{kg}\,\text{m}\,\text{s}^{-2}\ \mathbf{e}_3. \tag{2.7}$$

.

The drag force $\mathbf{f}$ and the propulsive force $\mathbf{g}$ differ between the three modes. For the sinking mode, there should be no propulsive force as the copepod is assumed to be passively sinking yielding $\mathbf{g} = \mathbf{0}$. This strictly leaves the drag forces to balance the excess weight. A swimming copepod on the other hand must produce a force orders of magnitude larger than the excess weight in order to overcome the downward gravitational force (Jiang et al. 2002c). To this regard, we take $\mathbf{w}_{\text{excess}} = \mathbf{0}$ leaving drag forces to counteract the propulsive force. In the last case, we have a hovering copepod. Here, we make no additional assumptions on any of the forces, leaving the three forces non-zero.

2.3.3 Solving for the force vectors

Having identified the forces in play, we use the above approximations in order to solve for the fluid velocity. As a matter of notation, for a model using n regularized Stokeslets, we assume that the first $n-1$ regularized Stokeslets are located along the discretization of the antennae cylinder and the final n-th regularized Stokeslet represents the body. This allows us to rewrite the above force balance equation, see equation 2.6, as

$$\mathbf{f} + \mathbf{g} = \underbrace{\mathbf{f}_1 + \cdots + \mathbf{f}_{n-1}}_{\text{drag}} + \underbrace{\mathbf{f}_n}_{\text{propulsive}} = \mathbf{w}_{\text{excess}}. \tag{2.8}$$

The fluid velocity at a point $\mathbf{x} \in \mathbb{R}^3$ with n regularized Stokeslets located in $\mathbf{Z} = \{\mathbf{z}_1, \mathbf{z}_2, \ldots, \mathbf{z}_n\} \subset \mathbf{R}^3$ in the laboratory frame of reference of a copepod translating at velocity $\mathbf{U}$ is given by

$$\mathbf{U} + \mathbf{u}(\mathbf{x}) = \sum_{i=1}^{n} \mathbf{K}(\mathbf{x}, \mathbf{z}_i)\mathbf{f}_i. \tag{2.9}$$

Utilizing the linear relationship between the velocities and force vectors allows us to prescribe the values of either the forces or the velocities, and solve for the resulting unknowns. Below, we outline the procedure for the three modes.

To begin with, the force balance equation above, see equation 2.8, will always be used as three of our equations. Furthermore, we include a non-slip boundary condition along the $n-1$ antennae Stokeslets, providing an additional $3n-3$ equations. Depending on the mode, we will either choose to define the velocity at the n th regularized Stokeslet and solve for the translational velocity vector $\mathbf{U}$, or vice versa. This will ulimately leave us with a system of $3n+3$ equations with $3n+3$ unknowns. For a sinking copepod, we apply the no-slip condition at the body Stokeslet, yielding $\mathbf{u}(\mathbf{x}_n) = \mathbf{0}$. This leaves the translational (sinking) velocity as an unknown. For the swimming and hovering modes, we prescribe the translational velocity vectors $\mathbf{U} = 10\,\text{mm s}^{-1}$ for swimming and $\mathbf{U} = \mathbf{0}$ for hovering. Thus, for both cases, the velocities at the body Stokeslet is left as an unknown.

For purposes of demonstrating the process, we use the sinking case parameters to illustrate it. In this mode, the translational velocity vector $\mathbf{U}$ is an unknown quantity. Therefore, the velocity at the j-th regularized Stokeslet located at $\mathbf{z}_j$ is given by

$$\mathbf{u}(\mathbf{z}_j) = \left[\sum_{i=1}^{n} \mathbf{u}_i(\mathbf{z}_j)\right] - \mathbf{U} = \left[\sum_{i=1}^{n} \mathbf{K}(\mathbf{z}_j, \mathbf{z}_i)\mathbf{F}_i\right] - \mathbf{U}. \tag{2.10}$$

This holds for $j = 1, 2, \ldots, n$ and supplies $3n$ of the equations. Including equation 2.8 as the remaining three equations leaves the n force vectors and $\mathbf{U}$ as the $3n + 3$ unknown values. The system of equations is encapsulated in matrix form: $\mathbf{A} = \mathbf{BC}$ where the $(3n + 3) \times 1$ vector $\mathbf{A}$ holds the values of the known quantities, the $(3n + 3) \times 1$ vector $\mathbf{C}$ holds the values of the unknown quantities, and $\mathbf{B}$ is an augmented matrix containing a combination of submatrices of the form $\mathbf{K}(\mathbf{z}_j, \mathbf{z}_i)$ and the 3×3 identity matrix $\mathbf{I}_3$.

$$\begin{bmatrix} \mathbf{u}(\mathbf{z}_1) \\ \mathbf{u}(\mathbf{z}_2) \\ \vdots \\ \mathbf{u}(\mathbf{z}_n) \\ \mathbf{w}_{\text{excess}} \end{bmatrix} = \begin{bmatrix} \mathbf{K}(\mathbf{z}_1, \mathbf{z}_1) & \mathbf{K}(\mathbf{z}_1, \mathbf{z}_2) & \ldots & \mathbf{K}(\mathbf{z}_1, \mathbf{z}_n) & -\mathbf{I}_3 \\ \mathbf{K}(\mathbf{z}_2, \mathbf{z}_1) & \mathbf{K}(\mathbf{z}_2, \mathbf{z}_2) & \ldots & \mathbf{K}(\mathbf{z}_2, \mathbf{z}_n) & -\mathbf{I}_3 \\ \vdots & \vdots & \vdots & \vdots & \vdots \\ \mathbf{K}(\mathbf{z}_n, \mathbf{z}_1) & \mathbf{K}(\mathbf{z}_n, \mathbf{z}_2) & \ldots & \mathbf{K}(\mathbf{z}_n, \mathbf{z}_n) & -\mathbf{I}_3 \\ \mathbf{I}_3 & \mathbf{I}_3 & \cdots & \mathbf{I}_3 & \mathbf{0} \end{bmatrix} \begin{bmatrix} \mathbf{F}_1 \\ \mathbf{F}_2 \\ \vdots \\ \mathbf{F}_n \\ \mathbf{U} \end{bmatrix} \tag{2.11}$$

The vector containing the unknown quantities is then solved for by inverting the $(3n+3)\times(3n+3)$ matrix $\mathbf{B}$ and performing the corresponding matrix multiplication to obtain $\mathbf{C} = \mathbf{B}^{-1}\mathbf{A}$. Once the unknown quantities are obtained, they are then substituted into equation 2.9 to produce the fluid velocity.

2.3.4 The flow fields

Before discussing the results of our flow field, we comment on a few attributes of the model. Notice that the antennae is represented by a row of regularized Stokeslets along the horizontal x_1-axis and the body is a single regularized Stokeslet located below the antennae Stokeslets on the vertical x_3-axis. This induces a great deal of symmetry for our model. For instance, the regions representing the dorsal and anterior side of the model are reflections of eachother. Viewing the regularized Stokeslet model in the x_1, x_2-plane from above with $x_3 > 0$ yields a reflected image. In a similar manner, there is also symmetry about the x_3-axis when viewing the model in the x_1, x_3-plane. This implies that our model produces a flow field that is symmetric about both the x_2 and x_3 axes.

Understanding the fluid flow around a feeding copepod was our first step into calculating the hydromechanical signal due to a spherical particle. Figures 2.4, 2.5, and 2.6 depict the vector fields for each feeding mode in the x_1, x_3 and x_2, x_3-planes along with some characteristic trajectories shown by the thicker lines in the frame of reference of the translating copepod. With regards to each feeding mode, a similar qualitative trend is apparent. Each mode has a strong vertical component to it, whether it be from passing below to above the model or vice-versa. However, there is a very noticeable difference between the sinking and swimming cases compared to a hovering copepod.

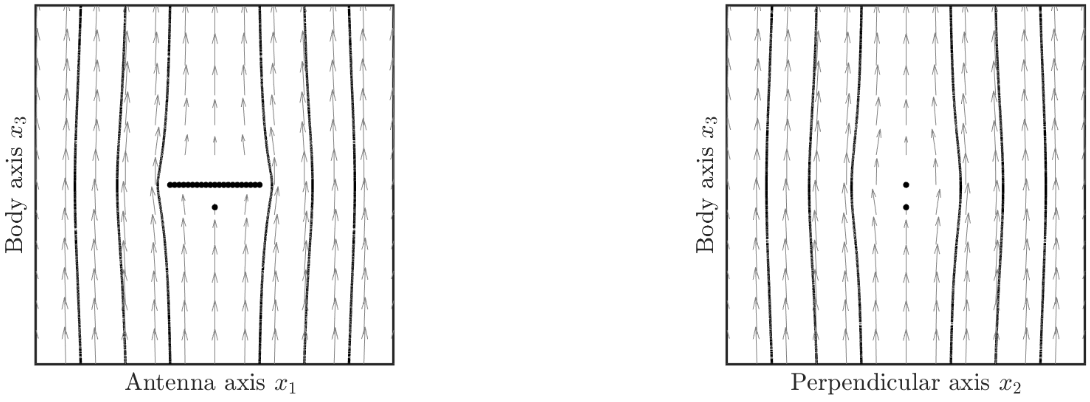

(a) x_1, x_3-plane

(b) x_2, x_3-plane

Figure 2.4: Velocity field for the sinking mode. The points represent the stokeslets used to approximate the body. Trajectories are shown by the dark lines. Vectors have not been scaled.

For the sinking case, depicted in figure 2.4, what we see is a vector field not too different from one produced by a sinking cylinder. The velocity vectors are generally unidirectional and comparable in size with very little deflection in horizontal direction. In the far-field, the fluid simply travels upward in a relatively straight path in both planes. In the near-field, trajectories are again quite vertical, but the trajectories do show a slight horizontal component in the vicinity of the antennae Stokeslets as they pass from below.

Similarly, the flow field for a swimming case shown in figure 2.5 is predominantly vertical in the far-field for both the x_1, x_2 and x_2, x_3-planes. The vectors are again quite comparable in magnitude and direction except in the close vicinity of the body Stokeslet where we see an increase in size and variation in direction. In the far-field, we see downward facing force vectors depicting the flow passing the copepod from above to below. In the near-field, there is a noticable change in behavior

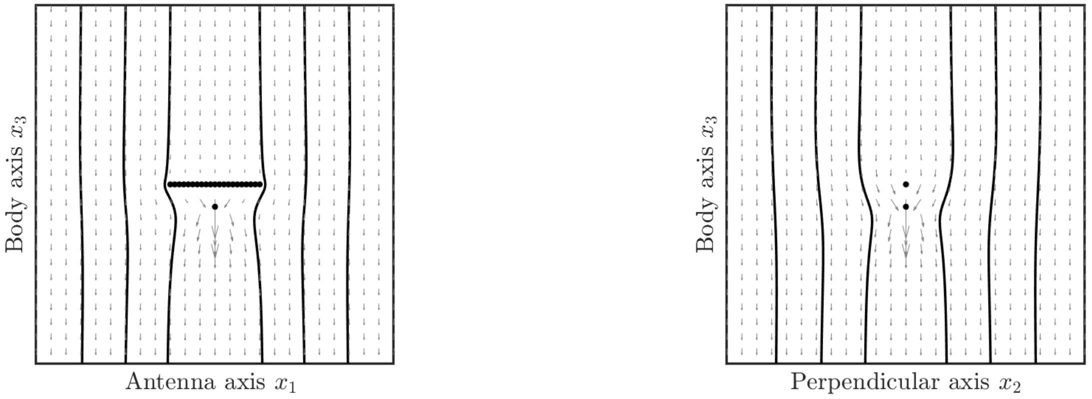

(a) x_1, x_3-plane

(b) x_2, x_3-plane

Figure 2.5: Velocity field for the swimming mode. The points represent the stokeslets used to approximate the body. Trajectories are shown by the dark lines. Vectors have been scaled by a factor of 2.

around the body and antenna. We see that directly above the antennae in the x_1, x_3-plane, the velocity vectors decrease in size to meet the no-slip condition along the approximated cylinder. Along the two ends of the antennae, there is a small amount of curvature as the fluid passes around the ends with a slight bend inwards towards the body. Below the row of Stokeslets, the vectors point inward and then outward as the flow passes the model's body. This is further demonstrated in the x_2, x_3-plane and depicts a drastic difference in the fluid velocity as it is ejected downward from the swimming copepod.

The flow field around the hovering model produces the most qualitatively different set of images for the x_1, x_2 and x_2, x_3-planes. Firstly, for each viewpoint, there is a large variation in the magnitude of velocity vectors. In the far field, the magnitude is weak and small. Moving inward, the magnitude begins to gradually increase until it reaches its maximum directly underneath the body Stokeslet. There is also a drastic difference in direction of the velocity vectors with reference to above and below the body Stokeslet. Above the body, we see that the vectors point inward towards the x_3-axis and below it, we see that the vectors have changed direction and are now pointing outward. Like the swimming case, the flow passes from above to below the model. This produces trajectories portraying a funnel like flow-field around a hovering copepod where a hovering copepod draws in the fluid, but not just from directly above it (or below it) like in the previous two modes of feeding, but from regions that extend horizontally outward as well. The plot of the x_2, x_3-plane shows the drastic

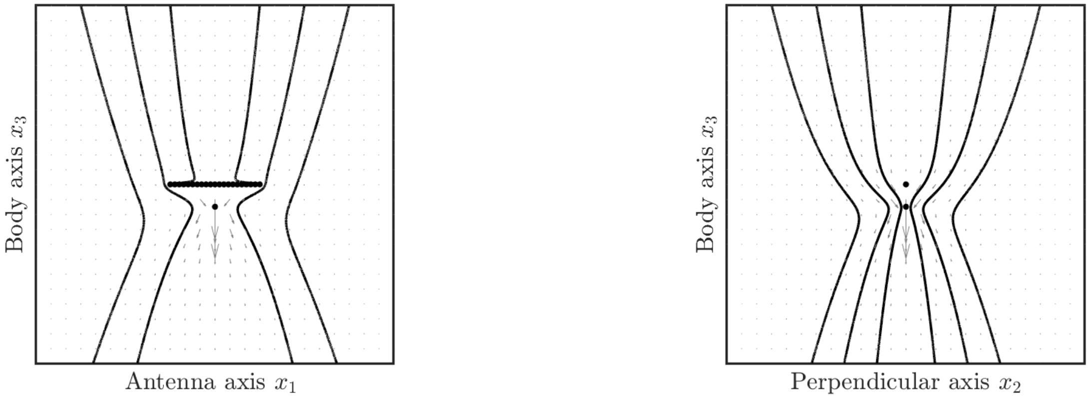

(a) x_1, x_3-plane

(b) x_2, x_3-plane

Figure 2.6: Velocity field for the hovering mode. The points represent the stokeslets used to approximate the body. Trajectories are shown by the dark lines. Vectors have been scaled by a factor of 2.

difference between the modes, as trajectory beginning the furthest from the model horizontally is drawn in near the body Stokeslet with a distance that is comparable with the trajectories that begin nearest the model horizontally in the other two modes.

The flow fields depicted and described here are the first hints into the qualitative differences between the three modes. They provide visual evidence that hovering may provide a copepod with a greater opportunity to come across a food source compared to the other two modes since it draws in fluid from a larger region. While this is certainly an advantage for this particular type of feeder, the flow field only shows the dynamics of the surrounding fluid and thus, only depicts one aspect of feeding, specifically the gathering of food. All their work is in vain if they are ultimately unable to sense their prey.

2.4 Sensing spherical particles

Copepods vision is limited to the detection of light and are unable to visually detect their food (Kiørboe 2011b). Therefore, they rely on other mechanics such as chemoreception and mechanoreception to detect the presence of food and obstructions present in the water column (Strickler and Bal 1973). Of particular interest for this study are spherical algal cells which is one primary source of nutrients for copepods. Organic matter seep a chemical signal which is advected throughout the water column and leaves a trail for the copepod to detect (Jiang et al. 2002b). This may be what happens on the macroscale, when the copepod is looking for its first hint for food. Once the animal has detected the general direction and positioned itself closer to the source, it begins to generate a feeding current. The surrounding fluid acts like a spider's web where the absence of obstruction serves as a baseline. The presence of an obstruction induces a disturbance flow field to the background feeding current which is then sensed by the copepod through deflections of sensory setae along the copepod's body (Strickler and Bal 1973). Below we outline a mathematical model for the disturbance velocity.

Consider a sphere of radius a with a rigid boundary centered at $\mathbf{y} \in \mathbb{R}^3$ immersed in a fluid with a background flow $\mathbf{u}$. Further assume that the sphere is non-motile and has a small density difference with the surrounding fluid, thus producing no external forces on the fluid due to acceleration (Maxey and Riley 1983). In this scenario, the particle simply moves with the background flow following the trajectory of a small fluid element located the center of the sphere. The flow field locally surrounding the particle applies a stress along the rigid boundary to conform the spherical shape to match the flow field in the absence of the particle. Following Newton's third law, the particle in turn applies a stress on the fluid. In the reference frame of the moving sphere, this stress is modelled as a stresslet, given by Faxen's third law

$$\mathbf{S}(\mathbf{y}) = \frac{20}{3}\pi\mu a^3 \left[1 + \frac{a^2}{10}\nabla^2\right] \mathbf{E}(\mathbf{y}) \tag{2.12}$$

where $\mathbf{E}$ is the rate-of-strain tensor. The resultant disturbance velocity at $\mathbf{x} \in \mathbb{R}^3$ induced by the stresslet located at $\mathbf{y} \in \mathbb{R}^3$ is given by

$$\mathbf{u}_i^S(\mathbf{x}) = \sum_{j=1}^{3}\sum_{k=1}^{3} T_{ijk}(\mathbf{x},\mathbf{y}) S_{jk}(\mathbf{y}) \tag{2.13}$$

where S_{jk} is the (j,k)-th entry of the stresslet $\mathbf{S}$ defined in equation 2.12 and

$$T_{ijk}(\mathbf{x},\mathbf{y}) = \frac{3}{8\pi\mu}\frac{(x_i - y_i)(x_j - y_j)(x_k - y_k)}{|\mathbf{x} - \mathbf{y}|^5} \tag{2.14}$$

(Takagi and Strickler 2020). In our calculations of the disturbance vector, we simplify equation 2.13 by neglecting the ∇^2 term in equation 2.12 since $a \ll 1$ and only contributes sums on the order of a^5.

Observations show that copepods have the ability to sense non-motile prey within a few prey diameters away from its body (Goncalves and Kiørboe 2015). In our model, we describe a detectable region around the copepod by computing the disturbance velocity vector $\mathbf{u}^S(\mathbf{x})$ given by equation (2.13) by taking into account the numerous mechanical sensory locations along the antennae over a plane surrounding the copepod engaged in the three modes of feeding.

2.4.1 How does sensing differ between the modes?

The hydromechanical signal is intimately linked to the rate of strain tensor of the background flow field. Therefore, flow fields that compress or elongate fluid elements will produce a signal with a larger magnitude. When comparing the three modes, there are some very noticeable differences in the regions where a particle would and would not be detected.

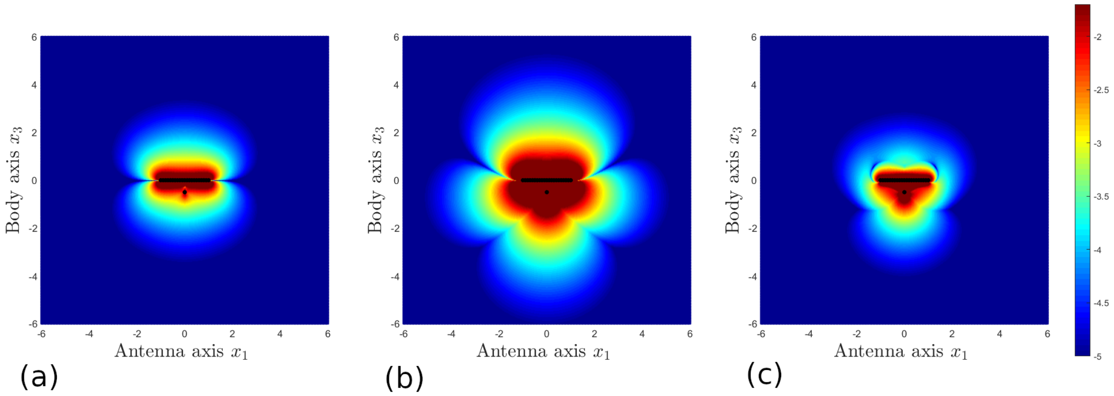

Figure 2.7: Maximum of the magnitude of the disturbance velocity vector in the x_1, x_3-plane for particles of size $a = 0.1$ mm in the three modes (a) sinking, (b) swimming, and (c) hovering. The points are colorized based on $\log_{10}$ of the disturbance velocity vector with the deepest red denoting detectable points with magnitudes larger than the detectable threshold and scales down to blue as the signal weakens. The regularized Stokeslets are denoted as black filled in circles near the center of each graph.

Figure 2.7 shows three plots depicting the variation in the hydromechanical signal for each of the three modes. The plots are produced using a heatmap color scheme where blue represents a magnitude decaying to zero and red represents a magnitudes leading up to an upper bound of the observed threshold of $\lambda = 20\,\mu\mathrm{s}^{-1}$ (Guasto et al. 2012; Lenz and Yen 1993). The x_1, x_3-plane is discretized as a cartesian grid at which the hydromechanical signal is computed using equation (2.13) with sensors located at each antennae Stokeslet individually. The maximum magnitude of the $n-1$ computations is selected for that particular point and is colored based on its value using the heatmap described previously. Thus, the outline of the dark red region in each plot depicts the boundary of the detectable region around the copepod for each mode while the dark blue depicts regions of undetectability. We discuss and compare the results.

At first glance, it is apparent that there is a drastically larger detectable region around a swimming copepod compared to the other two modes. The boundary of this shape surrounds the model on all sides in the x_1, x_3-plane. Overall, the shape resembles a snow angel and extends nearly a body length in each direction. What is interesting here is that the model predicts regions of undetectability near the tips of the antennae. This is shown by the outline of the dark red region that dip in towards the body near the ends of antennae. The sinking mode has the smallest detectable region among all the modes of feeding. The boundary of the dark red region is quite small and only extends a roughly a quarter body length around the antennae. Like the swimming mode, the detectable region does not completely surround the antennae as there is a sharp dip in the boundary at both ends. The detectable region around a hovering copepod lies somewhere between the other two modes. Similar to the swimming mode, the region encompasses all of the model's regularized Stokeslets but the area is significantly smaller. Furthermore, there is a dip in the boundary near the antennae, however the sharpness of the dip is not as strong as the other two modes. These plots demonstrate that a copepeod would be theoretically capable of sensing particles in regions surrounding the body in the x_1, x_3-plane. This data allows us to capture an even larger picture of their ability to sense their surrounding. Using the strong vertical component of the flow fields and evidence provided by these images, we are able to produce quantifiable data from a more natural perspective of a copepod.

2.4.2 The capture area

The plots of the detectable region for the three feeding modes in the x_1, x_3-plane provide evidence of the copepod's ability to sense particles around its body. By finding the vertical x_3-coordinate where the horizontal distance of the detectable region is the largest, we can construct a horizontal region surrounding the copepod where the area is maximized. The flow fields in figures 2.4, 2.5, and 2.6 portray trajectories that generally pass from above to below the copepod or vice versa. Using these two attributes, we can then consider the volumetric flux through these areas to compare the abilities of each mode.

The capture areas are shown in figure 2.8. For simplicity, the heatmap color scheme from the previous detectable region plots is replaced with a binary choice for each point: blue for undetected and red for detected. Due to the complex structure of the red region, a yellow curve approximating the boundary is used to aid in computation. The region bounded by the yellow curve is what we will

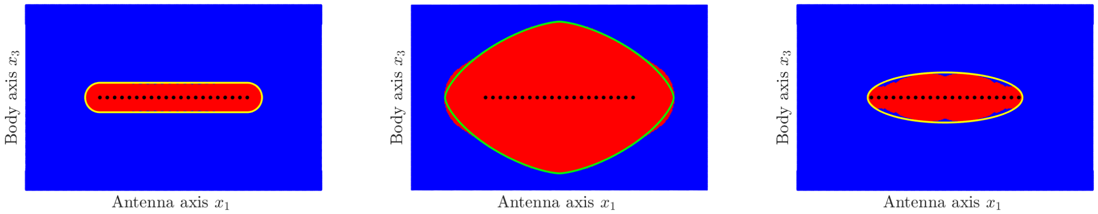

(a) Sinking (b) Swimming (c) Hovering

Figure 2.8: Capture areas for the three feeding modes (a) sinking, (b) swimming, and (c) hovering depicted with a binary color scheme using a particle of radius $a = 0.1$ mm. Detected spherical particle locations are indicated by red and undetected in blue. The approximated boundary of the capture area for each mode is outlined by a yellow curve and the stokeslet locations are denoted by black points.

call the capture area and represents the maximal horizontal region of detectability surrounding the copepod's body. What we see in figure 2.8 are three qualitatively different shapes. For the sinking mode, the boundary of the capture area extends outward relatively equally with respect to the antennae Stokeslets shown by black points. In contrast, there is some variation for the swimming and hovering mode. For the swimming mode, we have a diamond-esque shape surrounding the antennae Stokeslet with vertices along the x_1 and x_2-directions. The distance from the closest regularized Stokeslet to to the vertex is not equal either. Instead, we see that the distance is much shorter in the x_1-direction, about a quarter body length, than it is in the x_2-direction where it extends nearly a full body length. For the hovering mode, the capture area is elliptical in shape with the major axis along the x_1-axis and the minor axis along the x_2-axis. What is noticeably different in this image is that boundary of the capture area is in a close vicinity of the ends of the antennae. However, there is about a varying buffer around the length of the antennae with a maximal distance of roughly a quarter body length. With these capture areas, in particular their boundaries, we use these locations to construct what we call detectable streamtubes. For a point along the boundary, we look at the path of the fluid that passes through that point as a function of time to create the boundary of a volume of the fluid that will eventually pass through the capture areas.

The strong vertical component of the flow fields for the three modes of feeding hint at what seems to be the natural direction in which a copepod would expect its prey to travel. Using the locations of the boundaries of the three capture areas, we backwards integrate to construct the trajectories of the individual points to construct a volume representing the fluid that the will eventually pass through capture areas and are ultimately detectable. We name this region the detectable volume.

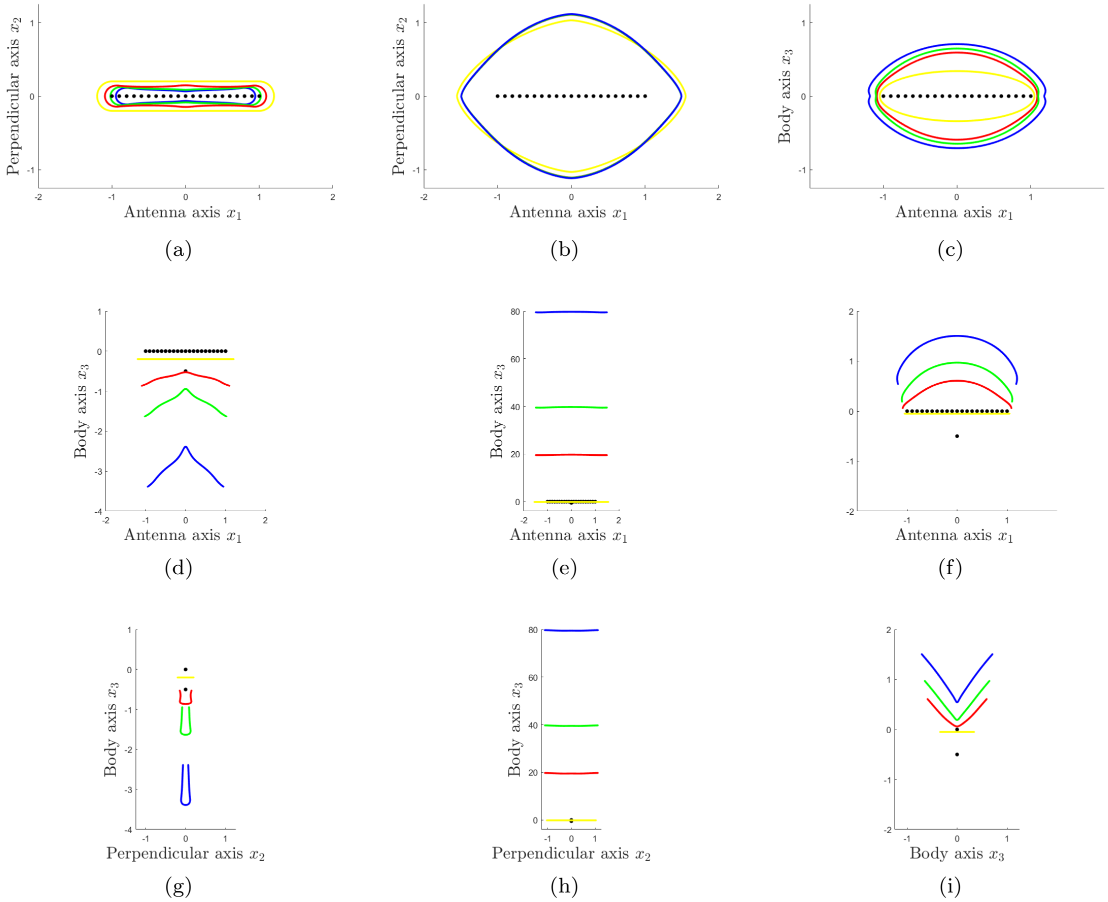

Figure 2.9: Backward time evolution of the boundary of the capture area for all three modes. The images are arrayed such that each column shows the the time evolution of the target zone for the x_1, x_2-plane, x_1, x_3-plane, and the x_2, x_3-plane in that order for the three feeding modes sinking (panels a,d,g), swimming (panels b,e,h) and hovering (panels c,f,i), again in that order. The initial boundary points are colored in yellow. Time is evolved for two, four and eight seconds and colored red, green and blue respectively. The regularized stokeslet locations are depicted by black points in each of the graphs. There is no scaling of the axis for the sinking or hovering case. The x_3-axis is scaled by a factor of one tenth for the swimming mode for clarity.

We first consider integrating backwards for set values of time. Figure 2.9 shows an array of plots in which we separate three point of view from three planes: x_1, x_2-, x_1, x_3-, and x_2, x_3-planes, by rows and separate the three feeding modes: sinking, swiming, and hovering, by columns. In each plot, the black points represent the stokeslets used in the model. The boundary of the capture area is drawn in yellow. Time is evolved backwards over the values of $t = 2$ seconds (red), $t = 4$ seconds (green), and 8 seconds (blue). The red, green and blue curves represent the region that will arrive along the boundary of the capture area after their given times.

It is immediately apparent that there is a drastic qualitative difference between the sinking and swimming modes compared to the hovering mode. For both the first two modes, there is quite a large vertical length along the boundary of the detectable volume, evident by the plots of the detectable volume in the x_1, x_3- and x_2, x_3-planes. However, the general shapes differ between the two modes. In the sinking case, what we see is a sheet-like volume that drapes down below the model. On the other hand, the detectable streamtube in the swimming case is cylindrical in shape and extends quite a distance above the antennae. A more important aspect of these two volumes is variation in the size of the boundary of the volume as time decreases. The detectable streamtube for the sinking copepod begins to decrease in size as the distance to the initial capture area increases. This is depicted by comparing the area of the boundaries in the x_1, x_2-plane. Here the boundary evolves from yellow to red to green and finally blue. This depicts a detectable streamtube with diminishing returns with respect to distance from the initial capture area. On the other hand, the boundary of the streamtube for a swimming copepod does not seem to vary much in comparison. The plot in the x_1, x_2-plane shows a very small variation in the area of the region as the colors evolve, with a slight decrease in the x_1-direction and a slight increase in the x_2-direction. Now, focusing on the hovering mode, we see a very large difference in behavior. Firstly, to address the vertical length of the volume that extends above the antennae, we note that this is about half the distance as the sinking case and significantly shorter than the swimming mode. However, the horizontal distances in the x_1, x_2-plane shows that the projected boundary is in fact increasing. The increase is less notable in the x_1-direction along the antennae, but is prominent in the x_2-direction. Here we see an increase in the projected volume that is roughly double the initial area of the capture area. The x_1, x_3 and x_2, x_3 views show a shape that is resembles a funnel like structure with a widening cone as the distance from the capture area increases. Comparing this to the previous two modes, what we have for the hovering mode is a detectable volume where the location of a detectable particle is not as restrictive. For a sinking copepod, only particles that lie below it in a decreasing volume will be detected. For a swimming copepod, a particle will only be detected if its projection lies within the initial capture area. In contrast, the restriction on the particle is significantly decreased due to the increasing expansion of the boundary of the detectable streamtube.

The second set of plots, figure 2.10, sets the streamtubes as a function of distance from the model's antennae. This may provide a more natural picture as it depicts a more realistic scenario of the detectable locations of particles relative to animal. The color scheme is given in order as red,

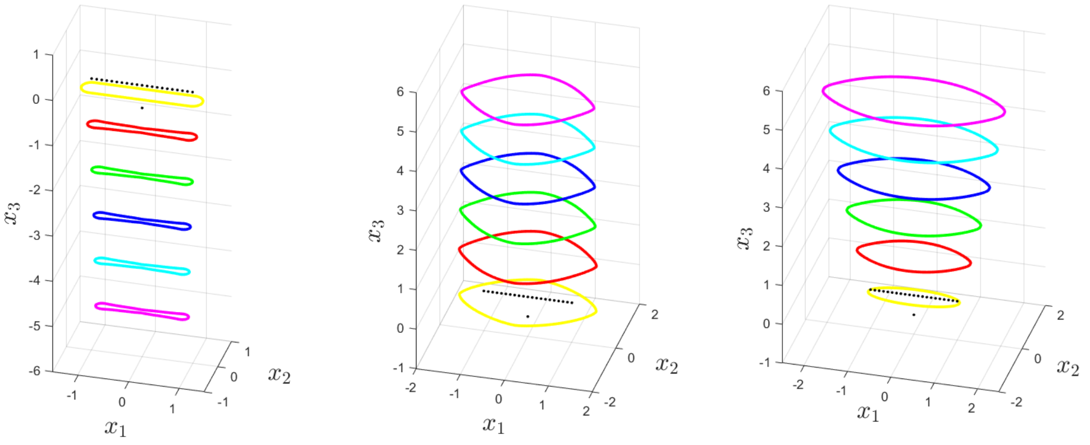

(a) (b) (c)

Figure 2.10: Time reversed evolution of the target zone intersected with horizontal planes above and below the copepod. (a) sinking (b) swimming (c) hovering.

green, blue, cyan and magenta with the respective distances of 1 mm, 2mm, 3mm, 4mm, and 5mm from the copepod's antenane. For reference, the initial capture area is again given by the yellow curve.

The streamtubes depicted here further demonstrate the results of the previous set of plots. The main important attributes for the streamtubes of each mode can be summarized by their characteristic shapes. The sinking mode again depicts a sheet-like shape that drapes down below the model. As the distance increases, the area of the intersection of the streamtube with the horizontal plane begins to diminish considerably. The largest decrease in size is noted along the x_2-direction as the sides begin to bend in toward the x_3-axis. For the swimming mode, we have much of the same behavior described in the previous set of plots. The streamtube extends above the antennae and the colored curves depict a streamtube that is largely cylindrical with little-to-no variation in the cross-sectional area. Again, the hovering mode stands out in comparison to the other two modes. The cone-like structure described previously is even more evident in this plot. The colored curves show a continuously expanding streamtube that increases in cross-sectional area as the distance from the antennae grows and displays a funnel-shape extending above the antennae. The comparison between the three modes follows similarly as above. The sinking and swimming mode provides streamtubes that either diminish in their cross-sectional area or stay relatively the same, while the streamtube for the hovering mode opens up above the model, with a cross-sectional area that increases in size as a function of distance.

2.5 Discussing the results

The ocean is a vast space for the copepod where some regions are dense in nutrients and others are not (Kiørboe 2011a). Algal cells leak chemical signals that are advected throughout the water by the ambient flow field of water column. This means that in order to locate its food source, the animal must be able to first sense the chemical signal and then locate its source. Doing so requires that the animal follows along a path in which the concentration gradient increases. Searching for its food source as well as capturing it ultimately requires energy from the copepod. To consider a mode to be more advantageous than another, we consider a cost-to-reward comparison. That is, we consider the amount of energy required by an organism to perform a mode of feeding as the cost and the volume of obtainable nutrients as the reward. For our analysis, we distinguish the modes of feeding by scenarios in which one mode would be more advantageous given a particular distribution of nutrient particles by providing context rather than simply comparing the geometric characteristics of each mode.

First we discuss an ideal and inplausible scenario. Suppose that the copepod was surrounded on all sides by an abundance of nutrients. In this scenario, all modes of feeding will ultimately provide it with food. However, only sinking may do so with a minimal cost of energy. Consider the streamtubes for the sinking mode in figures 2.9 and 2.10. Notice that the region of detectable particles lies directly below the antennae and so the copepod would be able to gather its food as it sinks. While the volume begins to diminish in cross-sectional area the further it gets from the body, the animal could simply begin to beat its appendages to stop sinking before continuing to sink again. Here, simply sinking uses no energy and the few moments used to beat its appendages would use less energy than if it were to continuously beat them to maintain its position in the water column by hovering. Theoretically, this would use the least amount of energy while still providing the animal with an ample amount of nutrients.

We now consider a scenario on the other side of the spectrum. Consider a scenario in which nutrients were sparsely distributed with large gaps between pockets of nutrients. Sinking could be useful here, but would leave too much to chance as the streamtube for the sinking copepod is considerably more narrow than the other two modes, swimming and hovering. Unlike the previous scenario where the requirement to find its food was completely eliminated, the copepod's ability to feed in this scenario completely relies on the opportunity of finding its food. For this scenario, swimming would provide the copepod with the best chances of encountering its food as the streamtube, as seen in figure 2.9 and 2.10, is wide and cylindrical extending above the copepod's antennae. For this, the energy required to continually propel itself through the water column could be considered an acceptable cost for the increased chance to come upon its food. Arguably, hovering would use less energy than swimming. While the streamtube for a hovering copepod also extends above the copepod's antennae and increases in cross-sectional area as the distance increases which consequently could lead to an increase in opportunity, the lengths to which it extends is considerably shorter. With a particularly sparse dispersal of nutrients, hovering would not allow the creature to explore a comparable amount of the water column compared to swimming.

The last scenario which we consider lies somewhere between the two extremes discussed above. Imagine a water column in which large pockets of nutrients are sparsely dispersed throughout the water column. Like the previous scenario, swimming along the chemical gradient would be the first step to finding its food. Once located, if the animal is able to position itself under the pocket, than rather than swimming directly through it, it would be more advantageous for the copepod to switch modes to hovering. Utilizing the enlarging streamtube, see figure 2.9 and 2.10, the copepod could maximize the yield of its prey. Once it has consumed the available nutrients, it could follow swim to the next source of nutrients and repeat the process. The combination of swimming and hovering would use less energy compared to just swimming through the water column. Furthermore, the yield of nutrients would also be increased compared to swimming. The streamtubes depicted in figure 2.9 are over equal time-steps. While swimming quite clearly depicts a region with a vastly larger detectable volume, hovering takes much longer and allows the animal time to carefully select its prey. Therefore, in this case, hovering would be more advantageous for the copepod.

Chapter 3

Fling and clap - Regularized Stokeslet Model

Copepods are extremely accomplished feeders. Some species that graze the water column must sift through relatively large quantities of water to search and obtain their food [Strickler]. This raises some interesting questions which we would like to begin to investigate. Firstly, how do copepods manipulate the fluid? There have been many observations of feeding copepods observed through microscopes (Strickler and Bal 1973; Strickler 1982, 1985; Price 1988) which describe what the copepod is doing and serve as a great starting point and inspiration in developing mathematical models to describe this physical phenomena. Another interesting question that one may ask is: why is this important? There are many great answers to this question. As a species, copepods have one of the highest biomasses among all animals in the animal kingdom. Given their respective size compared to the vast list of other animals, this is no easy feat and hints at their ability to survive. As finding food and successfully consuming it is an important aspect of this, understanding their ability to do so and to such a great extent would be a first step in explaining this. Another point of view is in regards to technology. A trend through recent decades is to build smaller, in the microscales. One great source of inspiration on how to deal with fluids and particles at a microscale could be sought for through nature. For instance, microplastics that come from man-made products have found their way into the oceans. While there have been many great inventions to deal with trash and debris at much larger scales, dealing with objects that are substantially smaller require different approaches and copepods may be able to inspire us with a solution.

In this chapter, we will discuss our simplified model of the fling and clap motion observed by Strickler (Strickler 2019) used to transport various particles trapped in the region between a pair of feeding appendages. We begin by introducing the physical problem introduced by the viscosity of the fluid, describe the thought process in developing our model, and then detail our results. There are two chapters on the fling and clap motion. This chapter models the motion through the method of regularized Stokeslets, as with the previous model in the previous chapter, where we first treat the feeding appendages as slender cylindrical rods which we then discretize as two straight rigid rows of spheres that rotate in a plane.

3.1 Motivational problem

In the previous section, we outline the physical problem that the copepod initially faces in its search for food, namely the ability to sense the presence or opportunity of its prey. Another challenge that the animal faces once it has overcome this obstacle is bringing the food into a location close enough that it may be able to consume it. While this might seem like a trivial task, this is actually quite difficult to accomplish in a viscous environment. The main food source for these grazing creatures are algal cells which have a negligible density difference with the water surrounding it (Kiørboe 2011a). This means that, generally speaking, the algae moves with the flow of the fluid. On a macroscopic scale, this may seem to be somewhat of difficult task to accomplish, but not impossible. We've all had instances where we've tried to remove debris or something similar from our beverages. For instance, coffee grinds floating in our coffee or perhaps a piece of hair from a beverage. Using our fingers to capture the object in a vice grip using our thumb and index finger can sometimes work, but it is usually significantly easier to use a spoon to displace the fluid surrounding the object to retrieve it. At the microscopic scale, the copepod unfortunately doesn't have a tool like spoons at its disposal. Instead, it must make use its anatomy to overcome the restrictions of its viscous environment if it hopes to feed.

The issue that arises in an aquatic environment is the difficulty in grasping objects. This is a problem for a variety of species of all varying sizes, but perhaps could be considered significantly more difficult in a low Reynolds number due to the high viscosity of the fluid. This is in part due to the no-slip boundary condition along the body of an animal. If a particle is orders of magnitude smaller than a body, is located in a close proximity to the boundary of the body, and has a low density difference with the surrounding fluid, it will tend to move with the motion of the body. This creates an extremely sticky and viscous scenario that makes it quite difficult to maneuver objects without direct physical contact with the object. This is indeed also true for copepods. However, some of these species have devised a way to circumvent this obstacle and effectively coax their food source near their mouth by manipulating the flow surrounding their food (Strickler 1985; Price 1988).

Briefly mentioned in the introduction, there are generally four types of feeding behaviors for copepods which can be further subdivided based on the mobility of the prey. In this paper, we are specifically focusing on non-mobile prey where the copepod does not sense any disturbance induced by a velocity gradient through the movement of the prey. Since the prey is not creating its own flow field, this group of feeders needs to rely on the presence of their food source in the water column in which its prey's location is relatively close to their body in order to sense it. This is more of an opportunistic scenario compared the more active feeders who sense their prey through disturbances in the flow field caused by the mobility of their prey. As a consequence, non-mobile prey feeders can be characterized as a sort of grazer. Some mindlessly sift the water column by oscillating their feeding appendages arrayed in a fan-like structure while others instead traverse the water column in search of their food source and position themselves in an advantageous location and generate their own current to draw the food to themselves once it has been sensed. The scenario we will be focusing on will be the latter of these two subgroups - feeding current feeders. Specifically, we will analyze how the copepod deals with its prey once the food is positioned near its feeding appendages using oscillating motion to maneuver food particles to its mouth.

Another difficulty that the copepod encounters along with the no-slip boundary condition around its body is that of reciprocal motion. Briefly stated, if a motion is the same regardless if time is run forward or backward, there can be no net displacement. Furthermore, the speed at which the motion takes place has no consequence on the flow field. While this may seem counter-intuitive, at low Reynolds number, inertia plays no role in the flow field. The velocity of a fluid particle suspended in a flow field in low Reynolds number is only affected by the flow field at that particular instance and is unaffected by the flow field at any previous instance. Therefore, in order to bring the food to its mouth, the copepod, at the very least, needs to break the symmetry of its oscillating arms. In reality, the copepod has multiple pairs of feeding appendages that are oscillating. In this study we will focus on a single pair of appendages and the flow in the near field trapped between the pair of arms. Unlike the previous section on sensing, the physical attributes of the particles and their presence on the flow are neglected. Instead, we will assume that the particles are traversing along the flow as a fluid element and analyze how the fluid moves as the appendages are in motion.

3.2 The fling and clap mechanism

Copepods are equipped with appendages used for various purposes. For example, some are used for propulsion while others are used for feeding. In his 1984, Rudi Strickler (Strickler 2019) observed the symmetry-breaking motion of the feeding appendages and noticed a striking similarity to that of the motion of the wings of many birds and insects. Dubbed the Weis Fogh clap and fling (or fling and clap) mechanism (Lighthill 1973; Kolomenskiy et al. 2011a), this motion has been analyzed extensively in a high Reynolds number regime. The majority of the studies are on the flight capabilities of small insects like wasps, butterflies and bees, to study how vortices are shed (Kolomenskiy et al. 2011b; Miller and Peskin 2005), how they take off (Jang and Lee 2013), increase hovering capabilities (Au et al. 2016) and lift (Santhanakrishnan et al. 2014), or the dynamics in different Reynolds number regimes (Kumar et al. 2015). Wing flexibility is another topic of interest not only in the nature (Miller and Peskin 2009), but also in practical use in building Micro Aerial Vehicles (MAVs) (Perçin et al. 2011). However, most of these studies focus more on the generation of vortices in the exterior region of the moving appendages outside of our area of interest. Regardless, it is quite fascinating to see that animals utilize similar patterns of motion to obtain quite drastically different goals regardless of the environment that they are operating in.

Strickler's discovery of the fling and clap motion came to light in the analysis of video footage in his 1984 publication and comments that a species of copepod's feeding appendages were capable of a variety of complex motion. This is an interesting fact which sheds some insight in the species capabilities of handling particles near its mouth. In a previous publication in 1980, he notes that copepods would spend time with possible food sources, testing it for quality, as well as maneuvering it into better position for capture and ingestion (Alcaraz et al. 1980). This demonstrated that the copepod was quite adept at dealing with small particles and had good control of the particle's position in the viscous environment. When there is no food source present, the appendages change their motion to draw water to itself. They search the water for evidence of the presence of food source by sieving the water, using perhaps chemical or mechanical signals, while funneling a constant supply of fluid and stopping when a potential food source arises.

When we think of crustaceans, we often think of a spider-like creature with a body and appendages that are more or less, like long and rigid cylindrical rods. However, the copepod's feeding appendages also have long thin setae that protrude outward. Therefore the influence on the water is affected not only by the appendages, but also by the hairlike setae, acting like paddles that sweep through the fluid. An interesting point to note is that the hairs are not stationary and are able to be flexed in a way so that the gaps between two adjacent setae can be increased or decreased in a similar way that we can flare our fingers outward. Therefore the copepod could have some control over the region of water in which the animal is able to move around. These two notions combined could imply that the copepod is adept at manipulating the fluid around itself and could explain why it is skilled at feeding.

3.3 Fling and clap model

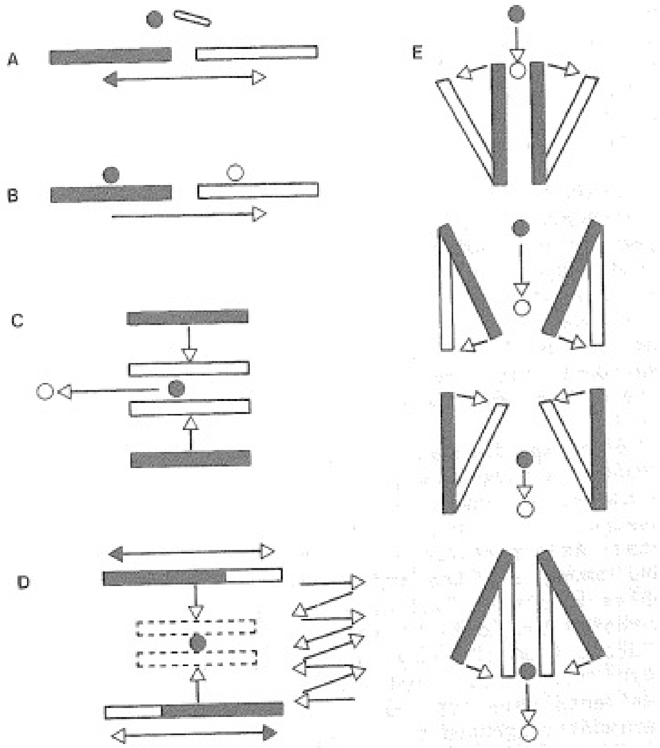

Figure 3.1: A sketch of the experiments done by Strickler using household objects. The rectangular shapes denote the blades of the knives used and the circular objects are the particles used in the experiment. The initial positions are shaded. The left column (A-D) are a set of different experiments. The right column (E) shows the sequence of motions for his model for fling and clap. Image taken from *Tropic Interactions within Aquatic Ecosystems, Sticky Water: A Selective Force in Copepod Evolution* by J. Rudi Strickler.

In 1984, Strickler provides diagrams suggesting the motion of the feeding appendages and its effect on a single particle near it, see figure 3.1, through an experiment using some common household kitchen supplies. He uses a pair of knives held vertically so that the tip of the knife to the base of the handle lie perpendicular to the surface. To mimic the fluid environment, he uses honey or corn syrup to introduce viscosity. A grain of rice in the fluid is used to represent a physical particle in the water column. Using the blade of the knives, he demonstrates their effect on the particle at different locations and under a variety of motions he'd observed in feeding copepods, see left hand column of figure 3.1. The right side of the same figure shows his two dimensional interpretation of the appendages cyclic motion through four stages with the initial positions denoted through by shading. Beginning from the top image and moving down, the knives begin with their blades parallel with a small gap between them. In the first step, a pair of ends sweep outward as they pivot about their respective opposite ends. In the second step, the roles of the ends swap so that the previous fixed ends now sweep outward with their respective opposite ends fixed in place to end the second step with the blades once again parallel but with a larger gap between them. In the last two steps, the roles of the ends again swap each time so that the ends sweep inward to return them to their initial position while the opposite ends are fixed. Throughout the four steps, the rice particle is seen to move downward from the outside of the gap between the two blades and travels further downward along the center line of the axis of symmetry before finally being ejected out the bottom by the final step of the cycle.

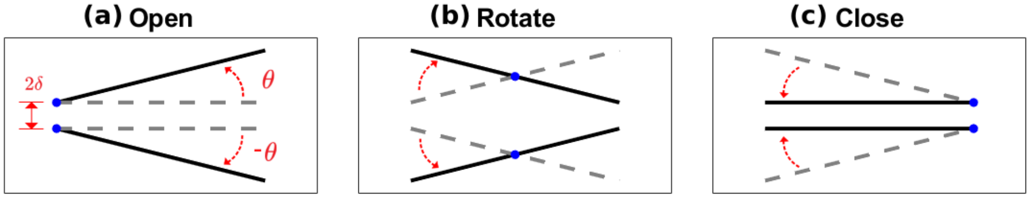

Figure 3.2: A diagram of our fling and clap model. The cyclic sequence begins with the image in the left and progresses to the right, open → rotate → close, with the initial position of each step shown by the gray dashed lines and the final position shown by a solid black line. Initially, the two arms are parallel and a distance 2δ apart. In the first stage (open), the two arms open up on the right side with an angle $\pm\theta$ that pivot about the two blue points on the left. In the second step, the two arms rotate about the midpoints shown in blue. In the final stage (close), the arms pivot about the blue points to return it to the initial configuration of the first stage.

In this study, we will use a simplified model of the motion of the fling and clap described by Strickler, see figure 3.1. Our model is shown in figure 3.2. Due to the cyclic nature of this mechanism, we will define the start or initial configuration as the two lines representing the rigid feeding appendages parallel to eachother and separated by a gap 2δ with the copepod's body located on the opening of the left side, see figure 3.2(a). The motion throughout the cycle can be defined through a pivot location along with an angle of rotation. From the initial position, the motion is through a rotation that opens up the right side by pivoting the arms around the left end points of the line. Upon reaching the terminal angle θ, the pivot location then shifts to the center of each arm and a rotation by $-\theta$, figure 3.2(b). The figure now looks like a vertical reflection of the initial step, figure 3.2(a), and is returned to the initial position in the final step through a pivot around the right end points of the appendages, figure 3.2(c). The general idea here is that in the first stage, the opening in figure 3.3(a)-(b), fluid is drawn between the two appendages. The rotation stage shown in figure 3.3(c), then pushes trapped between the right end of the appendages towards the middle and left end of the body. In the final stage, figure 3.3(d), the fluid is then further pushed out the left end of the arms near the mouth to test for quality of nutrients while the appendages again repeat the cycle.

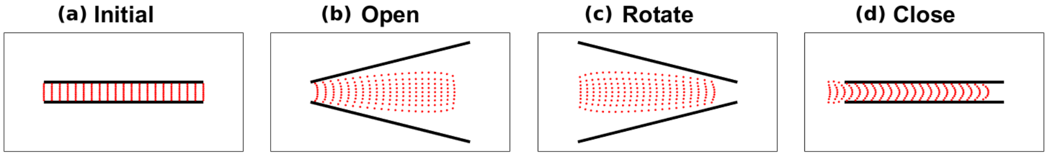

Figure 3.3: A demonstration of the movement of particles (red dots) scattered between the two cylinders (solid black lines) through a single cycle of the regularized stokeslet fling and clap model.

The main difference between this motion and Strickler's fling and clap is that the second and third step of Strickler's is combined into a single step in ours. In Strickler's model, the arms pivot about the ends and switch at the end of each step. In our model, the location of the pivot transitions from one end of the arms, to the center of the arms, and then finally the opposite end of the arms. We do not investigate if this difference between the two models has any noticeable change in the net displacement of particles, but it would be interesting to see if the change would be more or less efficient. As the overall transition from step to step is relatively the same, the qualitative behavior of the flow field would probably not be too different.

Strickler's model serves as a great initial step into understanding the dynamics of the fling and clap mechanism performed at the microscale. His observations and experiments provide a solid foundation into the investigation of particle manipulation in a viscous environment. To further understand this, a mathematical model could provide us with answers to further questions. For instance, how does the spacing between the arms affect affect the flow between them? Or, does varying the degree to which the arms open up have a profound effect on fluid? These could be answered through experiment, but replication and accuracy of the experiments could play a factor in the results. Developing a mathematical model would go a long way in eliminating any human errors. We sought to develop a model that was simplified enough to capture the motion of the fling and clap mechanism to study its affects on the fluid. Arguably, a pair of slender rigid rods is a very crude approximation of the arms, and surely a highly accurate representation of the copepod's appendages would yield a highly realistic flow field. However, this would be extremely computationally expensive. Developing the simplest model would allows us to easily vary parameters and would serve as a base point for those who wish to pursue a future study with increasing layers of detail.

3.3.1 Deriving the flow field

In this portion of the study, we consider a single pair of appendages simply as a pair of slender rods or cylinders. In this way, any curvature of the appendages is neglected as are the hairlike setae and the appendages are considered to be just a pair of rigid rods. The main region of interest lies in the 2δ gap between a pair of slender rods lying lengthwise in a horizontal x, y-plane, see figure 3.2. To analyze the flow field of the pair of rods in motion, we approximate each slender rod by a series of spheres of the same radius whose centers are spaced evenly along the major axis of the rod and whose volumes intersect such that a single point of one sphere touches the center point of the adjacent sphere. This discretization of the cylinder is similar to that of the antenna of the copepod's body in section 2.3.1. The motion of the arms are parameterized by linear equations of the form $x_2(t) = A(t)x_1 + E(t)$ where both the slope $A(t)$ and x_2-intercept $E(t)$ are both functions of time.

The fling and clap model that we've adapted is a cyclic motion with three steps transitioning in the order open-rotate-close. Each step is assumed to take an equal amount of time, so we can think of one cycle taking three units of time. We can describe the motion of the top arm with three parametrizations and obtain the motion of the second arm by reflecting the parametrization about the x_1-axis. We nondimensionalize the length scales so that the horizontal length of the arms is 2 mm and therefore the arms run between $x_1 = \pm 1$. In the initial opening stage, the arms pivot about the leftmost points at $x_1 = -1$. In the middle rotating stage, the arms then pivot about the points that lie along $x_1 = 0$. In the finial closing stage, the arms pivot about the points where $x_1 = 1$. The parametrization is broken up between three intervals given below

$$h_1(x,t) = atx + at + e \quad \text{for } 0 \leq t < 1 \tag{3.1}$$

$$h_2(x,t) = a(3-2t)x + a + e \quad \text{for } 1 \leq t < 2 \tag{3.2}$$

$$h_3(x,t) = -a(3-t)x + a(3-t) + e \quad \text{for } 2 \leq t \leq 3 \tag{3.3}$$

where a is the maximum slope of the upper arm and e is half the initial gap between the arms. The parametrization for the lower arms are given by $-h_i(t)$ for $i = 1, 2, 3$ over the same time intervals.

The flow field is calculated following the same procedure as in the section on sensing using the method of regularized Stokeslets. However, in this model, we prescribe the motion of the stokeslets using the equations (3.1), (3.2), and (3.3) and therefore the position of each stokeslet is determined by computing the center of stokeslet along each line as it progresses through each stage. For the kth stokeslet, the velocity at time t is prescribed by computing the time derivative of h_i, for $i = 1, 2$ or 3 depending on stage) at the x_1 coordinate of the k-th stokeslet. This leaves the force vectors from equation (2.3) as an unknown quantity for which we must solve for to compute the flow field similar to the sensing model.

The regularized stokeslet fling and clap is a model that lives in $\mathbb{R}^3$. As the main interest of the study is region trapped between the arms, we focused our attention in the two dimensional plane that contains the stokeslets. In our analysis, we compared the differences to the flow field by changing how close the appendages were brought together through the parameter e or the magnitude they were separated through the parameter a.

3.4 Results

3.4.1 The parameter a

For this section, let's assume that we hold the gap between the two feeding appendages constant and allow the angle in which the appendages pivot to vary. Intuitively, as the angle increases, more water is allowed to pass into the region between the two arms and therefore the distance in which the particles trapped between the feeding appendages should increase. Tracer particles are arrayed as a grid in the region between the two appendages and their trajectories are computed using Euler's method.

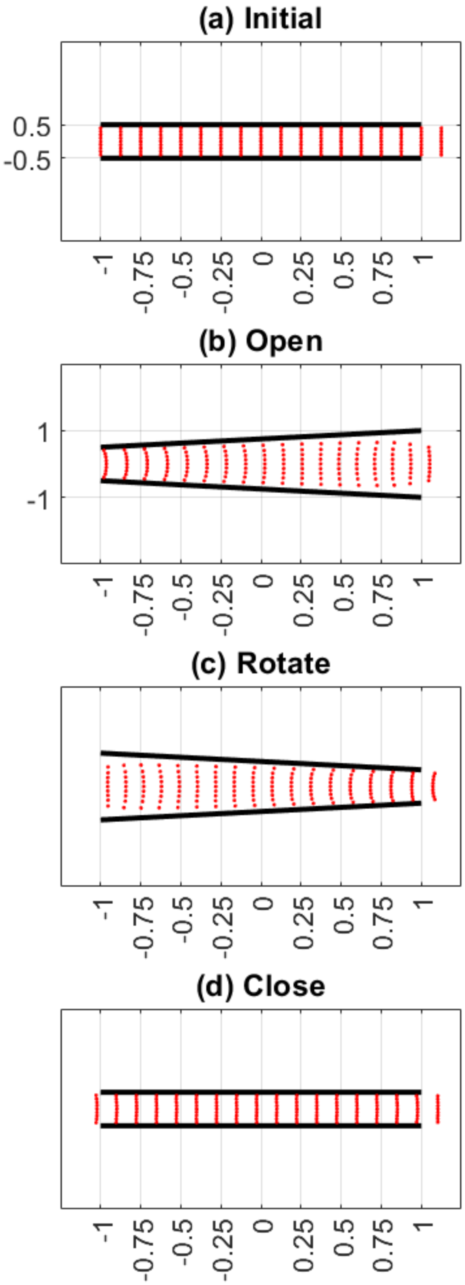

Figure 3.4: Regularized fling and clap with $e = 0.5$ mm and $a = 0.25$, figure scaled. Red points represent particles between the two arms and are arrayed in columns separated by a distance of 0.125 mm beginning from the left opening of the arms (body end of copepod) through past the right end of the arms, with a final column of particles 0.125 mm past right endpoints of the arms.

In figure 3.4, the maximum slope that the arms reach is a slope of 0.25. This means that the maximum gap between the arms throughout the fling and clap cycle is 2 mm as seen in figure 3.4(b). With this scenario, very small adjustments are made to the overall net displacement of the particles.

Notice that in the transition between the initial stage and the opening stage, shown in figure 3.4(a) to 3.4(b), as the arms open, depending on the horizontal placement of the column of particles, a different parabolic profile is shown. To the left of the 0.25mm mark, the columns of particles bow to the right. In contrast to this, the columns between 0.25mm and 0.75mm marks bend in the opposite direction, to the left. The final two columns on the right in figure 3.4(b), the columns again switch the direction the bow, now to the left. As the arms open, fluid particles outside of the arms are drawn in to fill in the area introduced by the increase in the gap of the two arms. This has an effect on the column of particles located between the arms. Because the the fluid is assumed to be incompressible, the increase of volume or area requires that the pre-existing particles bend and move to accommodate for the added fluid between the arms. Transition between the opening and rotating phase, figure 3.4(b) to (c), we see an almost reflected image of the opening stage where columns to the right of the of the -0.25mm mark now bow to the left and the remaining columns of the left of the -0.25mm mark bow to the right. This would account for the symmetric nature of the model during the rotational stage. In the final transition between the rotational stage and the closing stage, we see that the arms columns more or less return to their original profile. There is some deviation, but they are more or less straight columns.

The main focus that we should focus on here is the horizontal displacement of the columns as the model cycles. Throughout the transition between the stages, columns undergo a transformation through bends and bows that are parabolic in shape and change direction depending on the stage. Furthermore, considering the initial positioning of the particles in figure 3.4(a) and their final position after a single cycle in figure 3.4(d), we see that there is a definite, albeit small, horizontal displacement in the columns of particles.

In the next image, figure 3.5, the amplitude of the slope of the two arms is increased to 0.5. The effect here is the maximum vertical distance between two rods is now 3 mm. The overall effect on horizontal displacement of the vertical columns between the two arms is the generally the same throughout all of the transitioning stages. In the transition between the initial and open stages, figure 3.5(a) to (b), roughly matches the qualitative shape of the columns in the case where $a = 0.25$ in figure 3.4 (a) to (b). However, there is a drastic difference in the horizontal displacement of

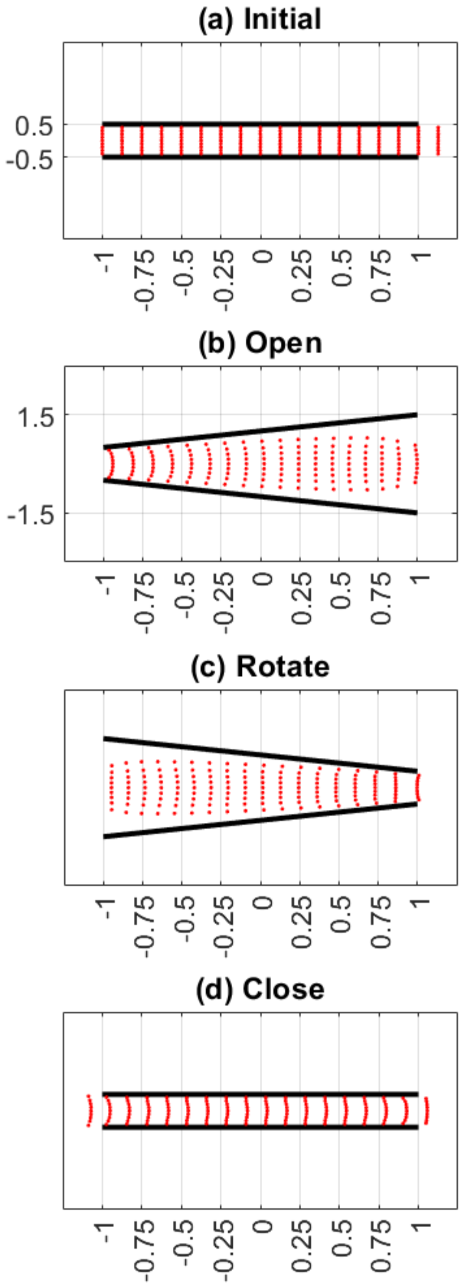

Figure 3.5: Regularized fling and clap with $e = 0.5$ mm and $a = 0.5$, figure scaled. Red points represent particles between the two arms and are arrayed in columns separated by a distance of 0.125 mm beginning from the left opening of the arms (body end of copepod) through past the right end of the arms, with a final column of particles 0.125 mm past right endpoints of the arms.

the rightmost three columns. Notice that the in figure 3.4(b), the column furthest on the right remains on the outside of the region trapped between the arms. In comparison, in figure 3.5(b), the rightmost column is now fully contained within the region between the horizontal 0.75mm and

1.0mm tick marks. In fact, more can be said about the effect of increasing the amplitude of the arms. The bow in each of the columns in figure 3.5(b) is much more pronounced for each affected column and there is much more vertical displacement along the arc of the bow. This could be accounted for by the stretching of the vertical line through a given column as the opening of the right hand size has increased in comparison to the previous case. The larger region in the gap between the rods introduces more fluid from the outside area in which the pre-existing fluid needs to mold its boundary to account for it. If we consider region between the top of each column and the bottom of the upper rod, we see large triangular shaped region representing the area of the new fluid. The transition between the open and rotate phase also introduces some interesting behavior in figure 3.5(b) to (c). Notice that similar to the previous parameter value of $a = 0.25$, the images are qualitatively reflections of eachother. However, there is a much more pronounced wave-like structure as we look at the profiles of each column. This may be a bit more evident in the final image on the right, figure 3.5(d). Notice that unlike the previous case, the columns have not returned to their initial form and now have curvature which is more pronounced in the columns on the end of the rods. Comparing the initial stage in figure 3.5(a) and the final stage in figure 3.5(d), there is an evident ripple effect induced by the wave-like motion of the rods. In this case, there is a greater horizontal displacement of the columns in which each column has shifted to the left with a greater magnitude than the previous case.

The final value for the slope parameter is $a = 1$, see figure 3.6. In this case, the maximum vertical distance between the arms is 5mm. As with the previous two scenarios, the overall qualitative behavior of the trajectories of the particles is the same. The first transition from initial to open, figure 3.6(a) to (b), we see that there is an influx of new fluid brought into the gap between the two arms but with a greater volume than the previous two values of a. The effects on the particles are more closely related to that of $a = 0.5$ and depict a clearer image of the wave-like profile seen in figure 3.5(d). However, unlike the previous two cases, the horizontal coordinate of the column that remains somewhat unaffected and vertical is now at the horizontal tick at 0.5 mm. In the near vicinity of this column and branching outward horizontally, there is a gradual increase in the magnitude of the bowing of the columns. Another interesting point is that in figure 3.6(b), the columns that are bent bow in the same direction. In the next stage of rotation, figure 3.6(c), a number of columns bow in both directions, see the region between the horizontal ticks 0.0mm and 0.5mm. In the final transition from rotate to close, figure 3.6(c) to (d), the arms pivot about the right most endpoints

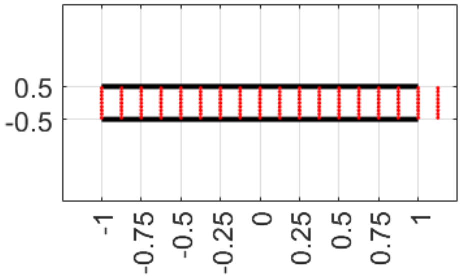
(a) Initial

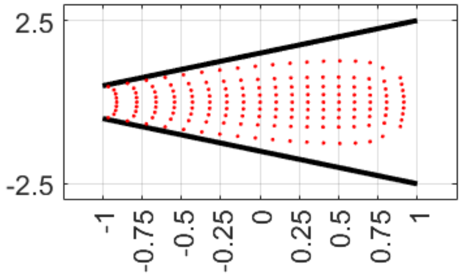
(b) Open

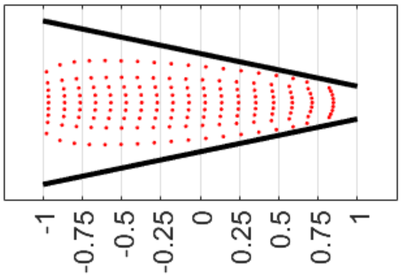
(c) Rotate

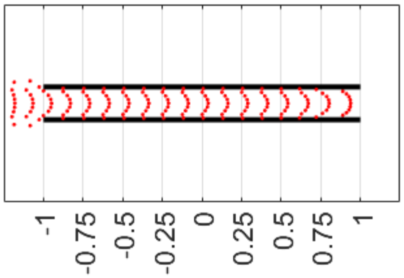
(d) Close

Figure 3.6: Regularized fling and clap with $e = 0.5$ mm and $a = 1$, figure scaled. Red points represent particles between the two arms and are arrayed in columns separated by a distance of 0.125 mm beginning from the left opening of the arms (body end of copepod) through past the right end of the arms, with a final column of particles 0.125 mm past right endpoints of the arms.

of each cylinder and the particles are ejected outward with a considerable distance. Comparing the initial configuration with the resultant positions in the final close stage, we see that each column has moved to the left a considerable distance. Furthermore, each column doesn't retain its original shape and is instead bowed to the right. The overall effect is that fluid between the arms has been squeezed while shifting to the left.

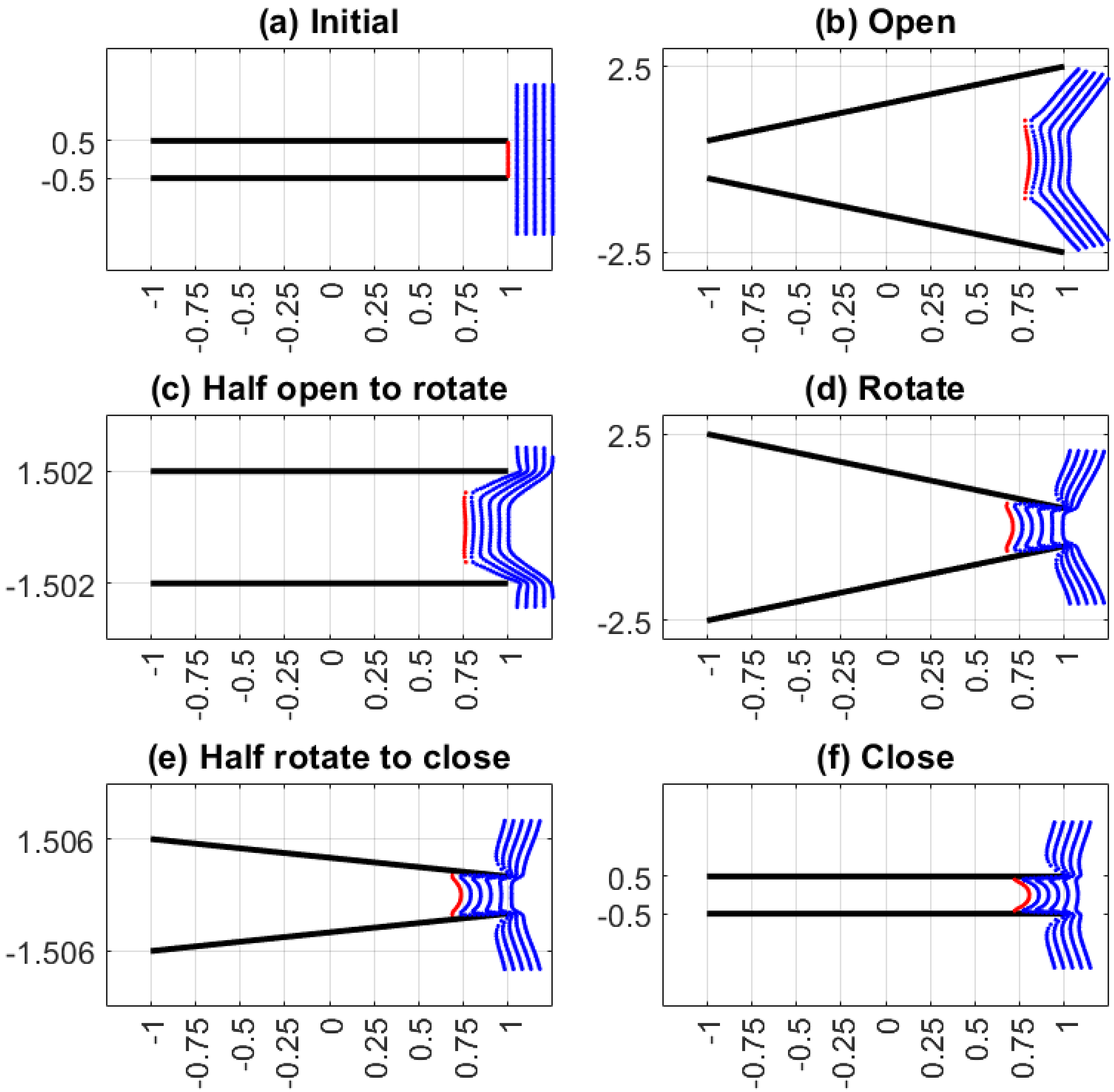

Figure 3.7: Regularized fling and clap with $e = 0.5$ mm and $a = 1$, figure scaled. Red points represent particles between the two arms with $x_1 = 1$. The blue particles represent particles that originate from particles to the right, outside of the region trapped between the two arms. The sequence (a) through (e) show the transition of particles as the model transitions between the stages. In (a) we have the intial configuration of particles. In (b), we have the configuration after the first opening stage has completed. In (c), we show the particle positions halfway between the transitioning rotating stage. (d) shows the particle location after the rotation stage has completed. (e) particle locations after half of the closing stage has completed. (f) shows particle locations after one cycle.

In the final stage for the varying values of $a = 0.25, 0.5, 1$, the column of particles located along the right boundary of the region trapped between the two arms are transported to the left. This is an effect of both the introduction of the outside fluid and the incompressibility of the fluid. Firstly, the fluid is assumed to be incompressible, meaning that volume of water cannot be compacted to take up less space. Secondly, fluid that is located to the right of the model is drawn in between the two arms. Consider figure 3.7(a), which depicts the position of several vertical (blue) columns of particles located to the right of the pair of cylinders and a single column of red particles represent the right boundary of the region trapped between the arms in the initial configuration. The figure shows the evolution of the outside particles as one cycle is performed at varying steps in time with parameters $e = 0.5$ and $a = 1$. In figure 3.7(b), the opening phase of the fling and clap has been performed. Notice that at this stage, blue particles with $x_2 \in [-0.5, 0.5]$ follow a similar pattern to the red particles and are drawn into the region between the arms with a parabolic profile bowing to the right. Particles with $|x_2| > 0.5$ have a more linear profile. Overall, what we see is a funneling effect. As the arms open, the vertical columns funnel into the region between the arms to fill in the newly introduced area. In figure 3.7(c), we show the evolution after half the rotation stage has been performed, and the cylinders are now parallel. The curvature of the profile for the particles with initial vertical coordinate $x_2 \in [-0.5, 0.5]$ are no longer parabolic, but are relatively vertical. For particles with $|x_2| > 0.5$, there are two different effects. Recall that during this stage, the pair of arms pivot about the midpoint of the cylinders with the right end points closing to produce a reflected image of the opening phase. Notice that the linear profile of these particles in the (b) are now bent. As the right ends of the cylinder rotate inward, the volume of fluid is compressed, squeezing the particles closer together. On the other hand, some of the blue particles that lie outside the right end points now form shorter vertical columns to the top and bottom right of the arm of cylinders. This is also caused by the rotation of the arms, in particular, the influence from the right endpoints. In figure 3.7(d), the rotation stage is complete and the cylinders have finished rotating close on the right. Some of the particles in the region trapped between the arms in (c) shift to the left. There is once again a parabolic profile that bows to the right. For the other particles, we see that they trail on the outside of the arms. In figure 3.7(e), we see the particle locations after half the closing stage has completed. During this stage, the cylinders rotate about the right endpoints and the left ends of the cylinders are drawn together. If we consider figure 3.6(d), we see that particles within the region between the arms retain a strong parabolic wave like shape that bow to the right. This is also apparent in figure 3.7(f), in which the bowing is even more pronounced. Throughout the sequence of motion in figure 3.7, we see that the fling and clap brings in a wave of fresh particles from the right after a single cycle of the fling and clap. It also demonstrates that these vertical columns are translated to horizontally to the left throughout the cycle. The translation has the largest magnitude in the first opening stage and weaker in later stages. From the final image in the sequence, figure 3.7(f), the center region of the blue columns have the largest translation, even more so for columns that are nearest to right end of the columns.

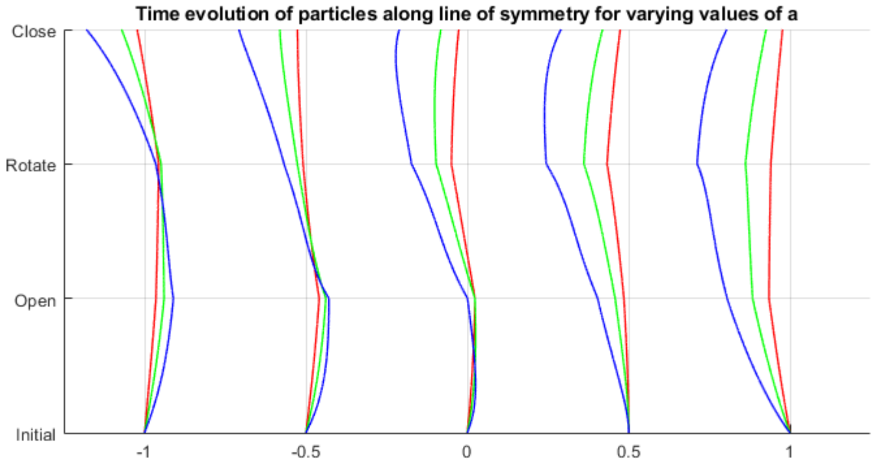

Figure 3.8: A graph of the horizontal displacement of particles along the line of symmetry with $x_1 = -1, -0.5, 0, 0.5, 1$. The horizontal axis is the horizontal coordinate x_1 and the vertical axis is time, with tickmarks denoting the end of the stages for one cycle of the fling and clap. The colors of each graph represent the different amplitudes $a = 0.25, 0.5, 1$ shown in the respective colors red, green, and blue.

If we compare the final closing stage in figures 3.4, 3.5, and 3.6, there is a definite correlation between the amplitude and particle displacement. It would seem that an increase in amplitude results in an increase in horizontal displacement. Consider figure 3.8 which shows depicts the trajectory of a particle trapped along the line of symmetry, $x_2 = 0$, for various particles with $x_1 = 0, \pm 0.5, \pm 1$ along the horizontal axis. The vertical axis is time over one cycle of the fling and clap with tick marks at the end of each stage: open, rotate, and close. Because the pair of cylinders are reflected images of eachother, then along the horizontal line of symmetry, there can be no vertical displacement throughout time. In other words, the line $x_2 = 0$ is invariant with respect to time. For each initial position, there are three graphs for the amplitudes $a = 0.25, 0.5, 1$ plotted with the respective colors red, green and blue. A clear trend that is that the blue curve for each initial point has the largest displacement to the left at the end of the close stage. In fact, we see the same trend for each initial point. The largest displacement to the left at the closing stage is the blue curve, followed by the green curve and finally the red curve. This refers to the change in the amplitude parameter

a descending in magnitude from $a = 1, 0.5, 0.25$. Therefore, increasing the amplitude increases horizontal displacement to the left.

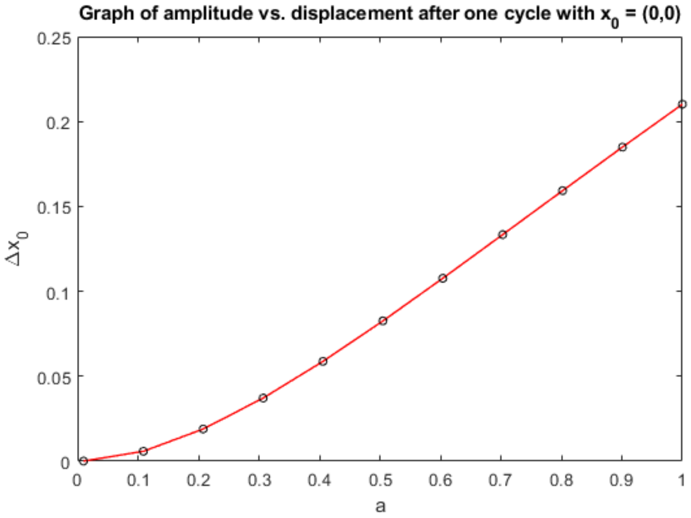

Figure 3.9: A graph of the horizontal displacement of a particle located at $\mathbf{x}_0 = [0,0,0]'$. The horizontal axis is amplitude parameter a and the vertical axis is the net displacement $\Delta\mathbf{x}_0$ after one iteration of the fling and clap. The horizontal coordinate of each black point is the value of a used in the simulation.

To further investigate the effects varying the amplitude, we fixed a point $\mathbf{x}_0 = [0,0,0]'$, the midpoint along the line of symmetry in the region trapped between the two arms. Letting a vary between $a = 0.1$ to $a = 1$, we graph the net displacement of $\mathbf{x}_0$ over one cycle of the fling and clap, see figure 3.9. This graph shows that there is a definite increasing behavior in $\Delta\mathbf{x}_0$ as a increases. In other words, the larger the maximum amplitude of the arms is, the further the particle located at $\mathbf{x}_0$ moves to the left.

For relatively small values of a, we can actually seek to quantify the increase. Letting $a \in [0.01, 0.1]$ we show the graph of a vs. $\Delta\mathbf{x}_0$ in figure 3.10 with two different scales on the axis. On the left, we have left both scales in their normal length, but on the right, we look at the length scales in $\log_{10}$. The purpose for looking at both length scales is that it is evident by figure 3.9, $\Delta\mathbf{x}_0$ changes on the order of a^n where n is some positive integer. Assuming that $\Delta\mathbf{x}_0 \approx ca^n$, we can look at the graph of the scaled axis of the figure 3.10(b) to determine the slope, and therefore the integer n. Using Matlab's polyfit function, we fit a line to the data for $a \in [0.01, 0.1]$ and determine a line with slope that is approximately 1.9507 with a y-intercept of -0.3841. From this, we conclude that for small values of a, the graph of $\Delta\mathbf{x}_0$ increases quadratically with a. In figure 3.10(a), the

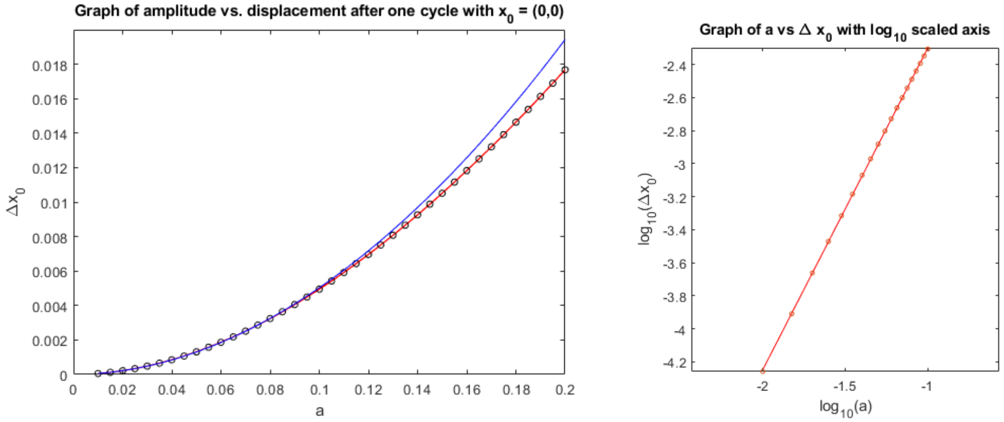

Figure 3.10: A graph of the horizontal displacement of a particle located at $\mathbf{x}_0 = [0, 0, 0]'$ for small values of $a \in [0.01, 0.2]$. (a) graph of simulated data in red, blue curve is the approximation by determining the coefficient c and degree n for the graph of ca^n. (b) Scaling of the axis to $\log_{10}$.

blue curve is the graph of $0.4486a^{1.9507}$, which for values of a that are less than $a = 0.1$ follow closely to the simulated data.

3.4.2 The gap parameter

In the previous section we considered what effect the amplitude parameter a had on the transport of fluid trapped in the region between the two cylindrical appendages. In this section, we will investigate how the gap separating two plates affects the flow of fluid throughout one cycle of the fling and clap. Throughout this section, the amplitude of the arms is fixed at $a = 0.5$ and we vary the spacing between the arms with $e = 0.25, 1, 1.5$.

The first case we considered are when the pair of appendages are separated by a distance of $2e = 0.5$ mm, see figure 3.11. In this case, the arms separate to a maximum distance of 2.5 mm. At the end of the opening stage, figure 3.11(b), we see that the column of red particles are qualitatively similar to the first two cases of the previous section where $e = 0.25$ and we varied the amplitude a between $a = 0.25$ and $a = 0.5$. Depending on the value of x_1 coordinate of the column, we again see parabolic velocity profiles which either bow to the right or the left. Around the column where $x_1 = 0.25$, we have a relatively straight column. To the right of it, the velocity profiles bow to the left whereas to the left of $x_1 = 0.25$, the velocity profiles bow to right. After the completion of the rotation stage in figure 3.11(c), we see that the velocity profiles are almost a vertical reflection of their profiles after the opening stage. The straightest vertical velocity profile is the column between $x_1 = -0.5$ and $x_1 = -0.25$. To the right, the parabolic velocity profiles bow to the the right and to

(a) Initial

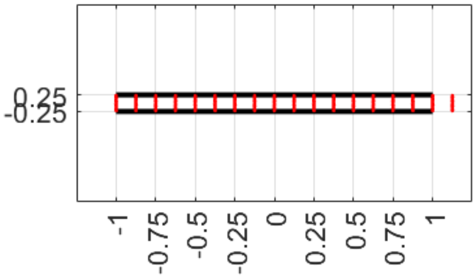

(b) Open

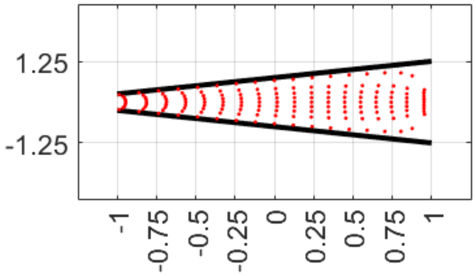

(c) Rotate

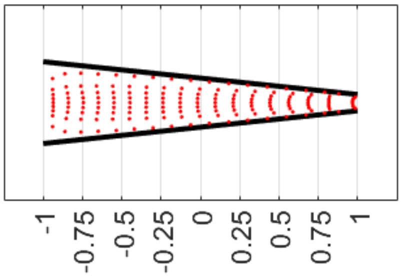

(d) Close

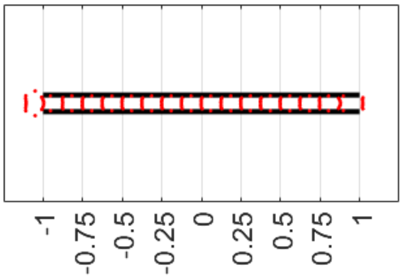

Figure 3.11: Regularized fling and clap with $e = 0.25$ mm and $a = 0.5$, figure scaled. Red points represent particles between the two arms and are arrayed in columns separated by a distance of 0.125 mm beginning from the left opening of the arms (body end of copepod) through past the right end of the arms, with a final column of particles 0.125 mm past right endpoints of the arms.

the left, they bow to the left. However, the bowing is more pronounced on the right hand side as the gap between the two cylinders is smallest on that side, which has driven the fluid together in that region. In the final closing stage, figure 3.11(d), we see that the fluid is ejected out the left hand side of the cylinders. The two columns which began at $x_1 = -1$ and $x_1 = -.875$ in figure 3.11(a) show displacement to the left with the furthest particles reaching a vertical coordinate of $x_1 = -1.1$ in figure 3.11(d). The right most column which began at $x_1 = 1.125$ can be seen to now linger as a relatively straight and vertical column near to the opening on the right opening of the appendages, indicating a displacement of the to the left.

In the next case, the cylinders are initially separated by a distance of $2e = 2$ mm and have a maximal separation of 4 mm at the end of the opening and rotational stages, see figure 3.13(a), (b) and (c). After the opening stage, we see the straightest vertical column near or along the column at $x_1 = 0.25$. To the right and the left, the columns again have a parabolic shape which all now appear to bow to the right with varying degree. The intensity of the bowing looks to be in relation to the horizontal distance from the column at $x_1 = 0.25$ where the curvature increases as the distance increases. After the fluid is rearranged during the rotational stage, see figure 3.12(c), it looks as though the straightest column is the one that second from the left. We also see a variation in the direction of the parabolic bowing in comparison the figure 3.12(b). Some columns look to bow to the left and some to the right, while others bow a bit in both directions, similar to dynamics in a previous case where $e = 0.5$ and $a = 1$, see figure 3.6(c). In the final closing stage, the two arms return to their parallel position, figure 3.12(d). At this point, the velocity profiles for each column look again to be parabolic with a distinct bowing to the right. There a clear transport of fluid to the left as the left most column, initially at $x_1 = -1$, has been ejected from the region trapped between the arms with the leftmost particle with an x_1 coordinate $x_1 = -1.07$ mm. The column that originally began along the line $x_1 = 1.125$ to the right of the pair of rods has also moved to the left. However, this distance is visually less than in the previous case with $e = 0.25$. The closest particle from the column, initially along the line $x_1 = 1.125$, to the line $x_1 = 1$ has vertical coordinate $x_1 = 1.07$ mm.

The final case we consider is when $e = 1.5$ mm. In this case, the cylindrical rods began a distance of 3 mm apart and have a maximal distance of 5 mm after both the opening and rotating stages of the fling and clap, see figure 3.13(a),(b) and (c). After the rods have opened up on the right hand side and fluid has rushed in to fill in the gaps, figure 3.13(b), the straightest velocity profiles seem to occur in the gap between $x_1 = 0$ to $x_1 = 0.25$. To the left, there is a slight bowing with the most pronounced occurring at the leftmost column. To the right, the strongest bowing occurs to the rightmost column. At the end of the rotational stage, figure 3.13(c), there is a sort of ripple effect

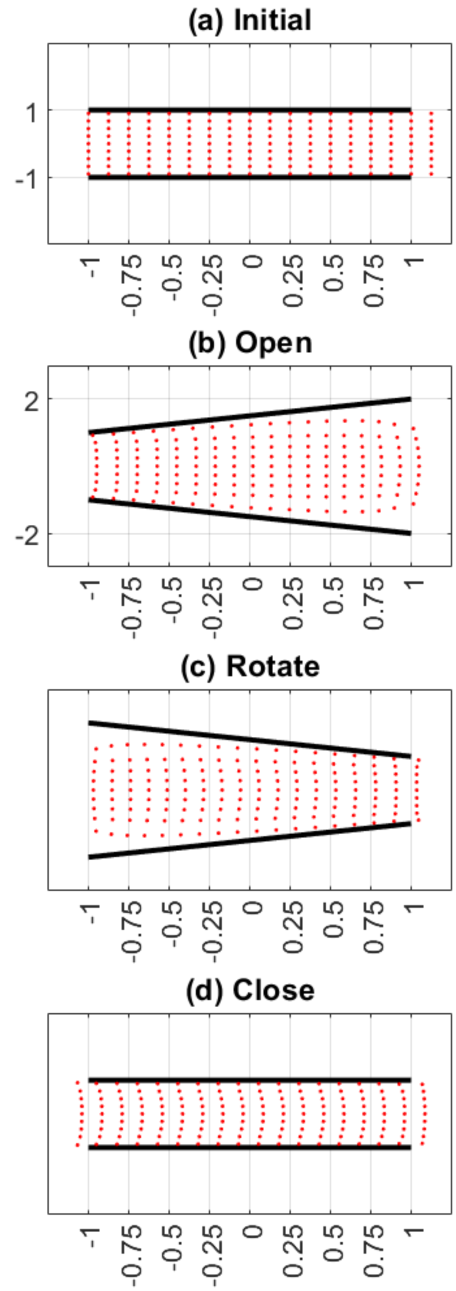

Figure 3.12: Regularized fling and clap with $e = 1.0$ mm and $a = 0.5$, figure scaled. Red points represent particles between the two arms and are arrayed in columns separated by a distance of 0.125 mm beginning from the left opening of the arms (body end of copepod) through past the right end of the arms, with a final column of particles 0.125 mm past right endpoints of the arms.

throughout the region between the two rods. At $x_1 = -0.75$, the velocity profile of the column is somewhat straight. To the left of it, the remaining two leftmost columns bow to the left, whereas to the right of it, the other columns bow to the right. In the final closing stage, we see that the leftmost

(a) Initial

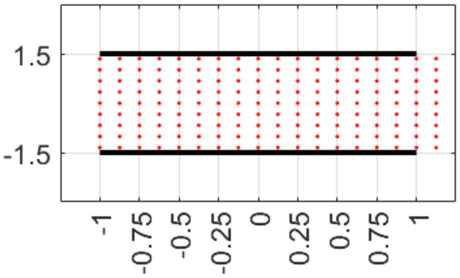

(b) Open

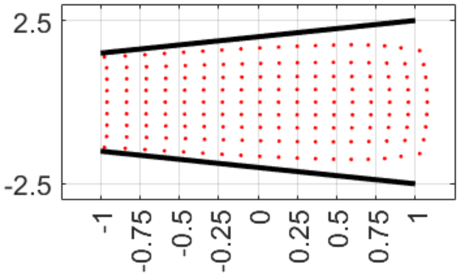

(c) Rotate

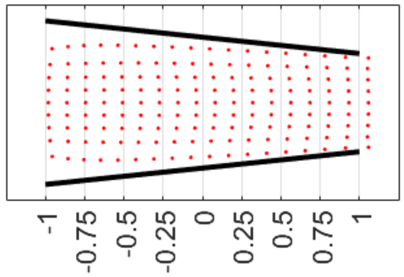

(d) Close

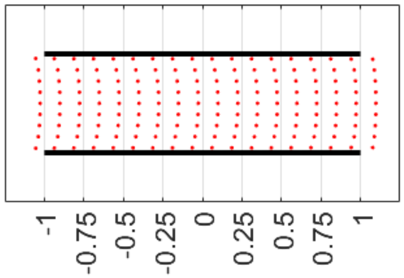

Figure 3.13: Regularized fling and clap with $e = 1.5$ mm and $a = 0.5$, figure scaled. Red points represent particles between the two arms and are arrayed in columns separated by a distance of 0.125 mm beginning from the left opening of the arms (body end of copepod) through past the right end of the arms, with a final column of particles 0.125 mm past right endpoints of the arms.

column is ejected out of the region between the arms and the column which began at $x_1 = 1$ has shifted to the left as well. The leftmost particle on the leftmost column has a vertical component of $x_1 = -1.05$ mm and the leftmost particle of the rightmost column (originally at $x_1 = 1.125$ mm) has a vertical component $x_1 = 1.08$ mm.

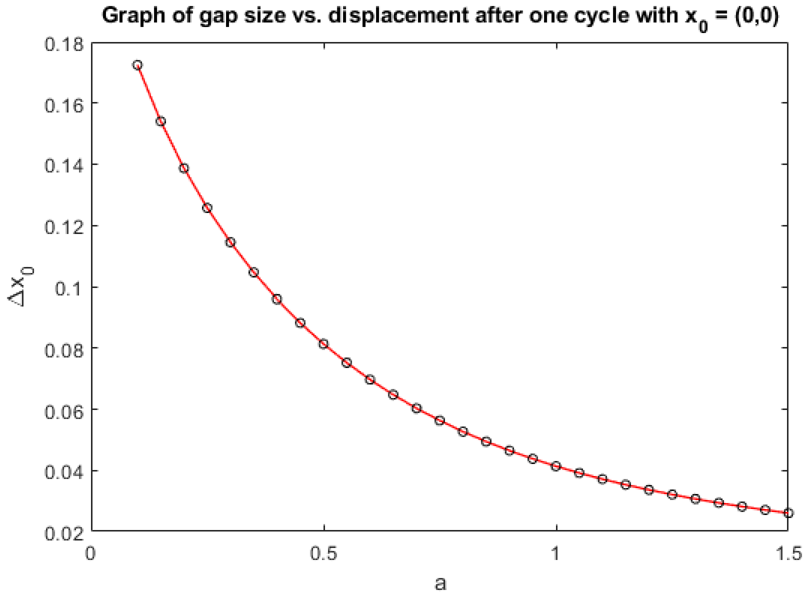

Figure 3.14: For the fixed point $\mathbf{x}_0 = [0, 0, 0]'$, we compute the particle position displacement after one cycle of the fling and clap for increasing values of e.

Through comparison of the final closing step of each cycle for the gap size $e = 0.25, 1.0, 1.5$, there is a clear indication that the spacing between the two arms plays a key role in displacing fluid to the left. In the first case, when the pair of appendages are closest together, nearly both of the leftmost columns of red particles, along the lines $x_1 = -1, -0.875$, are ejected from the region between the two arms, figure 3.11(d). The rightmost column with $x_1 = 1.25$ is also transported to the left and is almost within the region trapped between the arms. We see a similar picture in figure 3.5(d) from the previous section. Recall that in this case, the parameters are $a = 0.5$ and $e = 0.5$, so it serves as a case between $e = 0.25$ and $e = 1.0$ from this section. In that image, we see that the leftmost column has been fully ejected from the region between the arms, and the rightmost column has been drawn nearer to this region.

In figure 3.14, we plot this behavior for a fixed point along the line of symmetry, $\mathbf{x}_0 = [0, 0, 0]'$ and compute the net displacement $\Delta\mathbf{x}_0$ for increasing values of e. Notice that there is a steep decay in $\Delta\mathbf{x}_0$ for values of e in the interval $[0.1, 1]$. Afterwards the decrease is much less pronounced. The reason behind the decay in $\Delta\mathbf{x}_0$ is quite intuitive. The first thing to recall is that the amplitude of the arms is fixed, and the parameter e controlling the gap between the arms in the initial stage is increased. When e is small, the gap between the rods is small and therefore the area trapped between them is also small. Throughout the opening stage of the fling and clap, fluid from the neighboring region to the right is introduced and funneled between the pair of cylinders. Therefore the area of the initial region between the pair of rods must now deform considerably to accommodate the introduced fluid from the right. Now, if compare this same scenario when the gap is significantly larger, then the ratio of the area introduced during the opening phase relative to the initial region is significantly smaller than when arms are closer together. As the gap size increases, then the effect of the motion of the pair of arms also decreases in the vertical strip near the line of symmetry. From the evidence provided in figure 3.14, we come to the conclusion that as the parameter e increases, the net displacement of the particles trapped between the pair of cylinders decreases.

3.4.3 Summary of results

Our simplified model is used to mimic the qualitative behavior of Strickler's fling and clap motion from his previous observations and experiments (Strickler 2019). We simplify the geometry of the appendages to a pair of slender rigid rods and discretize the cylinder into a series of spheres. We compute the flow field due to the motion of the simplified fling and clap, figure 3.2, using the method of regularized stokeslets. We then control two parameters, a the maximum slope of the pair of arms, and e the distance between the the arms and line of symmetry in the initial stage and report our results which we summarize below.

In all three cases for the fixed gap of $e = 0.5$mm and varying parameter $a = 0.25, 0.5$ and 1.0 demonstrated in figures 3.4, 3.5, and 3.6, the model shows that a pair of rods that move following the fling and clap motion produces a net displacement of the fluid between the arms. The overall trend is that increasing the amplitude yields an increase in the net displacement along the line of symmetry. In the three cases for the fixed amplitude $a = 0.5$ and varying parameter $e = 0.25, 1.0, 1.5$ demonstrated in figures 3.11, 3.12, and 3.13, we still see a notable displacement of particles to the left. Our results provide evidence that the displacement to the left of a particle along the line of symmetry decays as the distance between the pair of cylinders increases.

It is again important to remind ourselves that the images above are plots of the position of particles within a two dimensional plane containing the center line of the cylinders and do not examine the dynamics in three dimensional space. Furthermore, it assumes perfect symmetry in the motion as well, that the rods pivot in perfect unision with a unique line of symmetry. These are physically impossible assumptions, the copepod's appendages cannot move following our model's configuration exactly. Another aspect of where our model deviates from the physical scenario is that we neglect the influence that the slender hairlike setae has on the surrounding fluid. However, this model demonstrates that just a pair of rods have a significant influence on the viscous fluid implying that an array of hairlike cylinders arrayed along the cylindrical arms would result in the appendages acting more like a pair of paddles than just a pair of slender rods.

Chapter 4

Fling and Clap - Lubrication Theory Model

In the previous section, we showed what a pair of cylindrical rods moving in the fling and clap motion could do to produce fluid flow. However, we also had neglected a key feature of the copepods anatomy - their hairlike setae. What the previous section demonstrates is that thin cylindrical rods can have a drastic impact on the sticky fluid even if it lacks the surface area of a much larger object. Their appendages are covered in setae, therefore when the copepod moves its appendages, both the appendage and setae act more like paddles rather than cylindrical rods. In this section, we will outline the approximations and simplifications of our model, derive the equations of motion, and show the results of our model.

4.1 Plates vs. rods

Much of the motivation behind this model is outlined in the previous section on the regularized Stokeslet fling and clap. We are still primarily interested in the fluid being driven between a pair of moving appendages during the fling and clap motion in figure 3.2. However, in this section, we make a major distinction from the regularized Stokeslet model, particularly by introducing the role that the copepod's setae play in driving the fluid. Figure 4.1 is a drawing of a copepod and its appendages by Koehl (Koehl 1981). The image on the left, figure 4.1(a) shows the side view while figure 4.1(b) shows the ventral view. Three types of appendages are drawn in detail and labelled as A for feeding, S for swimming and F for filtering. The long hairlike setae are depicted by long lines that extend from the appendages. On first inspection, it would seem that an array of thin cylindrical rods would have a small or minimal impact on the fluid. However, the setae add structure to the moving appendages and are capable of a range of motion. It has been reported that gaps between

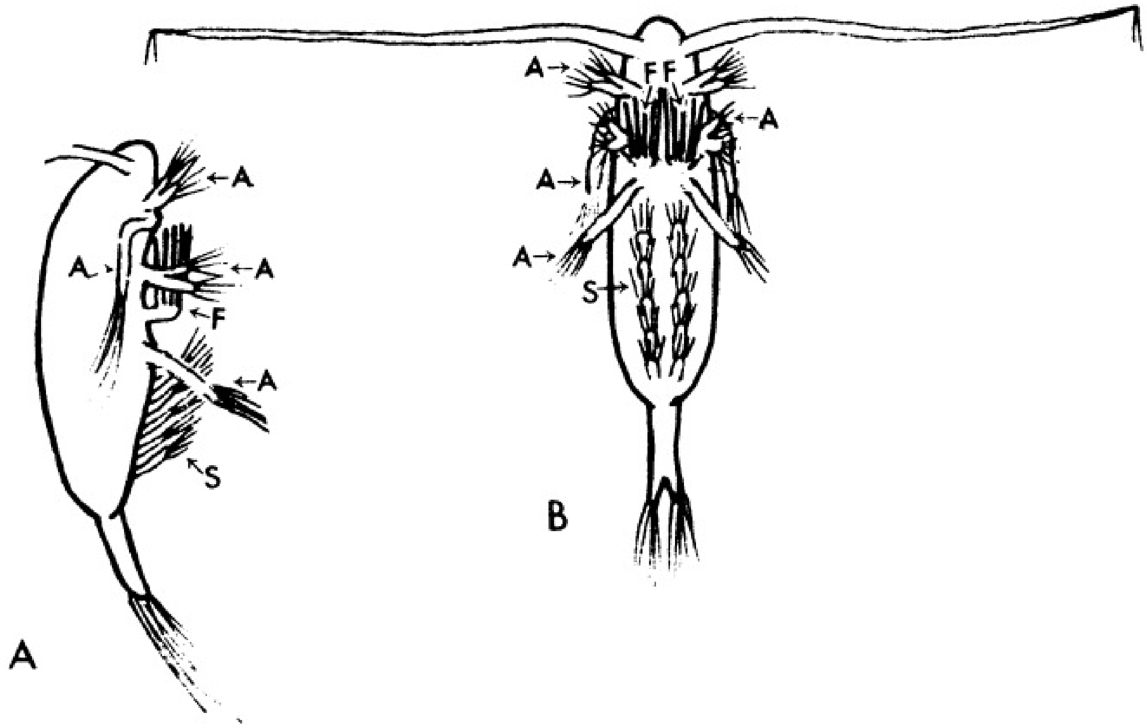

Figure 4.1: Drawing of a copepod accentuating the appendages and setae of a copepod. Figure on the left (A) is the side view and figure on the right (B) is the ventral view. The appendages roles are labelled A (feeding), S (swimming), and F (filtering). Image taken from (Koehl 1981)

the setae are not fixed so that they may be flared outward or contracted much like how our own fingers work (Koehl 1981). This could be highly advantageous when the copepod wants to fine tune the fluid flow near the setae to capture prey. Furthermore, because it adds additional structure to the copepod, food particles that are near the setae are easier to grasp as the no-slip condition along the boundary of the moving body ensures that food particles that either come into contact or are located near the setae tend to stay there which makes for easier capture. It is also noted that the setae could also be used to act similarly to paddles. This was observed and depicted by M. Koehl , see figure 4.2. Notice that the setae are flared outward to produce a fan-like rake rather contracted together in a way to extend the length of the appendage like a chopstick. The purpose of the drawing is to demonstrate the fan-like expansion's influence on the fluid as the appendage is pulled outward (out of the paper and toward the reader) in the region between the setae and the reader. The darkened area represents black dye that was introduced in the experiment to visualize the flow field. It is noted that the region trapped between the fan-like shape and reader and, in particular, does not slide in between the gaps of the setae. Instead, the flared array of setae act like a solid barrier.

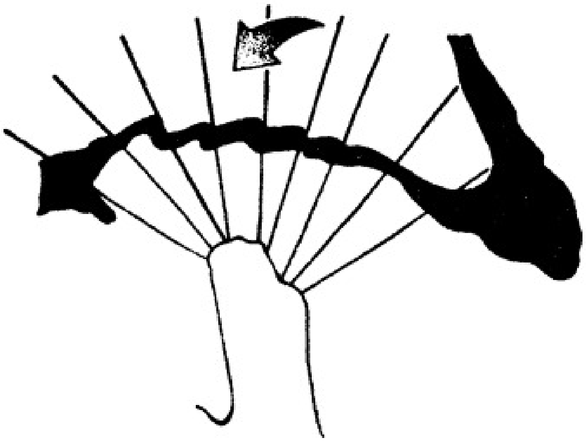

Figure 4.2: Drawing of a copepod flaring its setae along an appendage. The motion of the appendage is a pulling motion in the direction of the arrow out of the paper and toward the reader. The darkened region depicts black dye introduced to visualize the flow induced by the motion of the appendage. Image taken from (Koehl 1981).

In a later paper, A. Cheer and M. Koehl provided further knowledge in understanding this phenomena by developing a mathematical model for the fan-like structure of the setae by approximating them as slender cylindrical rods spaced along a straight line (Cheer and Koehl 1987). They simplify scenario by considering the influence of a pair of cylinders has on a background flow field when the axis of the cylinders are positioned perpendicularly to the direction of the background flow, see figure 4.3. In this image, they show the effect of the cylinders under three parameters (Re, d, s) where Re is the Reynolds number, d is the diameter of the cylinder and s spacing between the two cylinders. The background freestream velocity scale is the same for all three changes in the parameter so that the length scales in each of (a),(b) and (c) are all drawn to the same scale. In figure (a), the parameters are set to $(10^{-1}, 0.1\,\mu\mathrm{m}, 5\,\mu\mathrm{m})$, in (b) they are $(10^{-1}, 1\,\mu\mathrm{m}, 5\,\mu\mathrm{m})$ and in (c), they are $(10^{-5}, 1\,\mu\mathrm{m}, 5\,\mu\mathrm{m})$. Between (a) and (b) it is clear to see that the cylinders diameter does indeed have an effect as the increased diameter decreases length that the fluid travels between the two cylinders. Between (b) and (c), the images demonstrate that the Reynolds number also has an effect on how far the fluid is able to travel in the gap between the arms. That is, a decrease in Re leads to a decrease in the distance that the fluid can travel in the region between the two cylinders. They also note that the pair of cylinder's influence on the fluid can be categorized in one on its leakiness - a ratio of the volume of flow between the gap between the cylinders in the presence of the cylinders to the absence of the cylinders over a single unit of time. They find that appendages whose setae operate at a low Re act more like paddles than those whose setae operate at a higher Re. In other words, the fluids ability to pass through the gap between setae is a function of the Reynolds number that they are moving in.

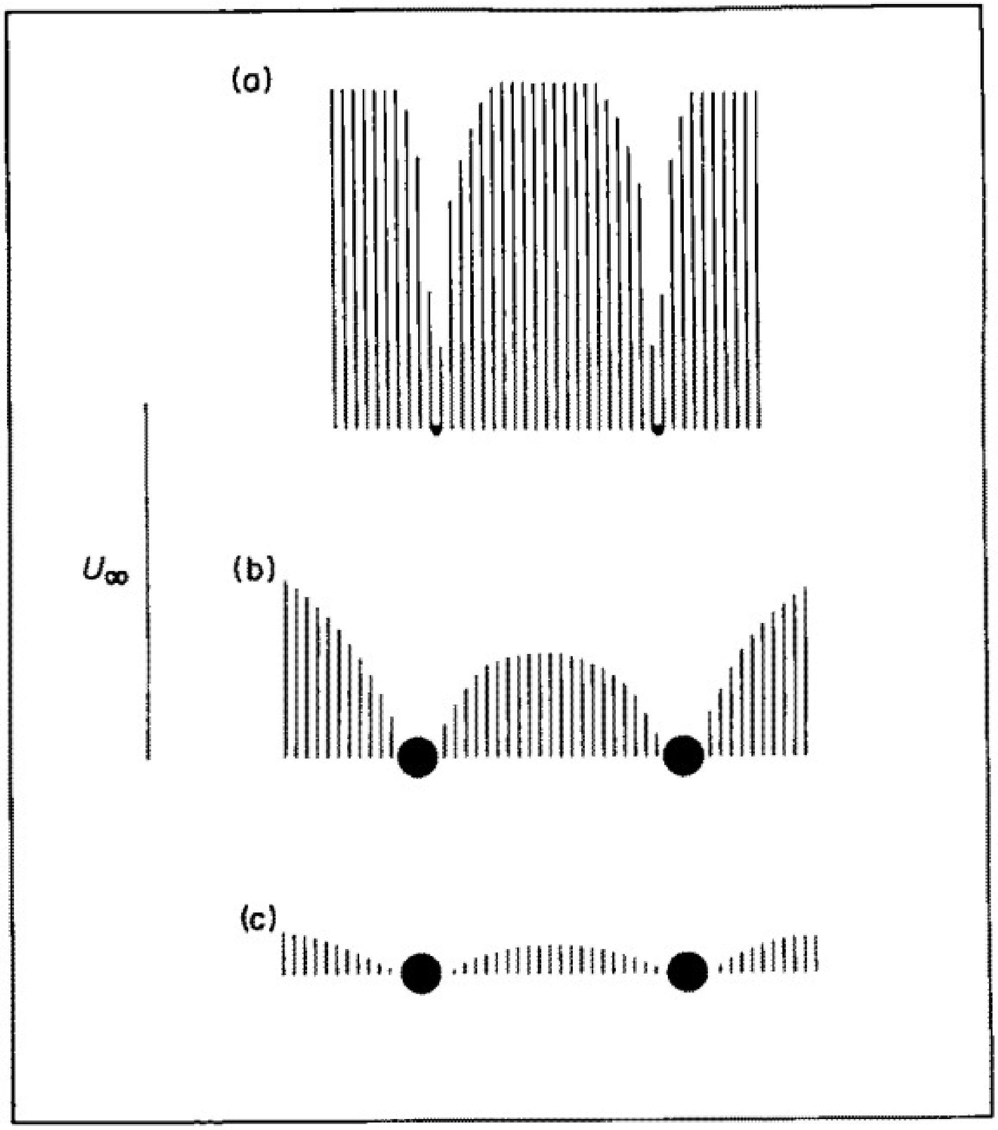

Figure 4.3: Flow field around a pair of cylinders (black dots), positioned perpendicularly to a uniform free stream velocity field (lines). In (a) Re = 10^{-1}, diameter of cylinders is 0.1 μm, and are spaced 5 μm apart. In (b) Re = 10^{-1}, diameter of the cylinders is 1 μm, and are spaced 5 μm apart. In (c) Re = 10^{-5}, diameter of the cylinders is 1 μm, and are spaced 5 μm apart. Image taken from (Cheer and Koehl 1987).

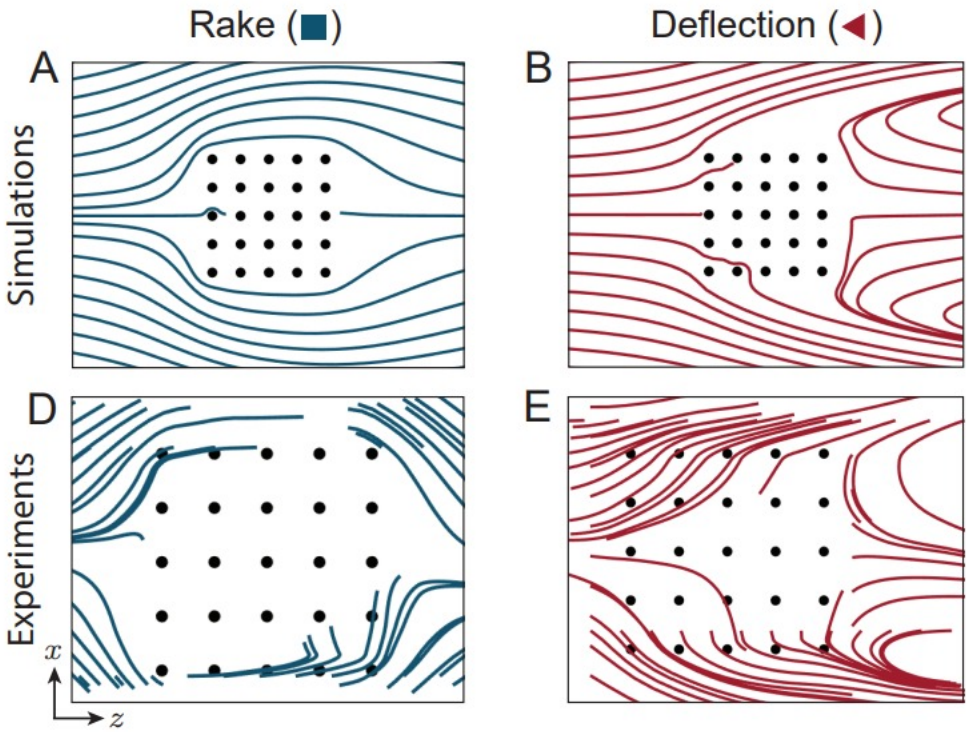

Figure 4.4: Flow field around a grid of cylinders with a diameter of 1 mm and 2 mm gap (black dots) positioned perpendicularly to a uniform free stream velocity field (lines). The top row holds the simulationed flow fields and in the bottom row, the flow field produced through experiments. The Reynolds number in (A) and (D) is Re = 0.8 and in (B) and (D) is 31. Image taken from (Hood et al. 2019).

In more recent years Hood, Jammalakadaka, and Hosoi observed similar behavior through experimentation and numerical simulation for a number of cylinders spaced in a grid pattern introduced into a background flow field moving perpendicularly to the cylinder's axis (Hood et al. 2019). Figure 4.4 shows their simulated results versus the results of their experiments for a flow field moving left to right. In all cases, the rods have a diameter of 1 mm is separated by a distance of 2 mm. The column on the left depicts the flow when Re = 0.8 and the right when Re = 31. In the left column, figures (A) and (D), where the flow field operates under a lower Reynolds number, the grid of cylinders acts almost like a solid wall and the gaps between the cylinders are ignored as the fluid passes around the boundary of the grid. In the other case on the right column, figures (B) and (E), when the Reynolds number is increased, the fluid passes through gaps cylinders. In this case, because the Reynolds number is much larger and the cylinders have less of effect on the fluid as the fluid is driven in between the gaps of cylinders. The presence of the cylinders cause a disturbance to the background flow field because of the no-slip boundary condition along the surface of the cylinder.

This induces a region around the cylinder where the velocity is varies continuously from zero along the boundary of the cylinder to the velocity of the background flow field. This region surrounding the cylinder where the velocity changes is called the boundary layer and is much thicker in low Re regimes compared to high Re regimes (Hood et al. 2019). If the gap separating an array of cylinders is small enough that their boundary layers overlap in a low Re regime, the authors state the flow should exhibit characteristics of figure 4.4(a) rather than 4.4(b).

As demonstrated in these two papers, the presence of cylinders has an effect on the fluid being driven perpendicularly to the configuration of the cylinders. In both cases, the configurations ability to repel the background flow field and act more like a solid object is directly affected by the Reynolds number - the lower the Reynolds number, the more effect is pronounced. With regards to copepods and their setae, if the animal were to keep the gap between the setae small enough by contracting them, we could consider approximate their feeding appendages by a pair of slender rods. However, if the copepod flares the setae outward while moving, then the motion of the feeding appendages is less like thin cylindrical rods moving in the fluid and more like paddles. In the previous section, we've investigated the influence on the fluid by a pair of slender rods and reported our results. Here, we would like to take the opportunity to think of the appendages and their setae as plates moving in the fluid and demonstrate the effects that a pair of moving plates would have on the fluid. Our simplification of the combined geometry of the appendage and setae into a single flat rigid plate may be a gross approximation of copepod's actual anatomical structure, but serves as a starting off point for future studies that may want to add further levels of complexity to their design. However, this simplification is done to gain an insight on the general qualitative behavior of the flow field while keeping the model relatively easy to compute for the purposes of numerical simulation and variation in parameters.

In our model, we will consider the arms to be a pair of plates in which they follow the design of the fling and clap motion from the previous section in the x_1, x_2-plane 3.2. These pair of appendages then extend infinitely in the perpendicular direction (into and out of the page). This means that we may eliminate the dependence on the third coordinate and consider only a single plane as the flow field will look the same regardless of the x_3-coordinate. To simplify the notation, we take the x_1, x_2-plane to be the x, y-plane.

One thing to note about our two dimensional flow field is its striking resemblance to the motion of fluid being pumped through peristaltic pumping. For some practical applications, this mechanism is used to pump fluid or gas through flexible tubing much akin to squeezing toothpaste through its tube. A more mechanical approach would be to run a tube filled with gas or fluid through a gap smaller than the circular cross section area of the tubing and using the pressure built up near the pinched region as the driving force. A longitudinal cross section along the axis of the cylindrical tubing near the obstacle resembles a sinusoidal wave that travels in the opposite direction in which the tube is being driven. Considering only the region of deformation, our fling and clap resembles somewhat of a linearization of the sinusoidal wave as it lacks the curvature due to the flexibility of the boundary of the tube. The fluid flow due to peristaltic pumping has been studied in numerous cases with both viscous and non-viscous fluids (Chrispell and Fauci 2011; Fauci 1992; Hung and Brown 1976; Kumar and Naidu 1995; Shapiro et al. 1969). How our model differs from this is that we assume that our boundaries are rigid. Therefore, rather than deforming the boundary to make the sinusoidal wave, our arms rotate around a given set of points. With regards to real life application for microscopic technology, the movement of our model may serve as a template or basis in which materials are required to keep their rigidity and may decrease the complexity in design and components.

Copepods are quite amazing creatures. Their microscopic size compared to the vastness of the ocean conjures up a David vs. Goliath type of scenario as they must engage in a hopeless battle against the raging of ocean's currents. However, despite all of this, they are still able to find a substantial amount of nutrients in order to survive. So much so that they, as a collective species, have one of the largest biomasses among all animals. It is possible that their ability to procure such vast quantities of sustenance may be hidden in technique. Our study wishes to look deeper into this. But, a copepod's anatomy is quite complex. Even just a single appendage has a complicated structure with its long hairlike setae that extend in different directions along the surface. Furthermore, the appendages are also capable of a wide range of movements depending on their purpose such as as swimming and feeding. These are very specific features of the animal. Our focus in this chapter will be to explore more general questions: If we were to simplify the structure of a pair of copepod's appendage to a pair of plates, would the fling and clap motion be able to transport fluid and particles closer to the copepod? Does increasing the maximum distance between the two plates increase or decrease the amount of fluid displaced? In this chapter, we construct a simple to use and easily modifiable model to add some insight to the communities current understanding by providing some new answers.

4.2 Deriving the flow field

The general premise of our problem is that the copepod has already sensed its prey and brought it near the feeding appendages. As the copepod flares its setae and oscillates its arms, it drives the particles up to its mouth for inspection and consumption. Considering the appendages and setae as a single object, we envision them as plates oscillating about some line of symmetry and simplify the motion through our fling and clap mechanism from the previous section, figure 3.2. Another assumption that we make is that the length of the appendages L is at least an order of magnitude larger than the length of the gap b between the two appendages so that $b \ll L$. The flow field $\tilde{\mathbf{u}}$ is within the Stokes regime and satisfies the pair of differential equations:

$$\mu\nabla^2\tilde{\mathbf{u}} = \nabla\tilde{P} \tag{4.1}$$

$$\nabla\cdot\tilde{\mathbf{u}} = 0 \tag{4.2}$$

where $\tilde{\mathbf{u}} = (\tilde{u}, \tilde{v})$ is the flow field in the x, y-plane and μ is the fluid viscosity. Using the characteristic

length scales L and b, characteristic velocity scales U and V for the dimensional coordinate system in the $\tilde{x}, \tilde{y}$-plane over dimensional time $\tilde{t}$ with timescale T, we non-dimensionalize equations (4.1) and (4.2) using the following conversions:

Dimensional	Non-dimensional
$\tilde{u}$	Uu
$\tilde{v}$	Vv
$\tilde{x}$	Lx
$\tilde{y}$	by
$\tilde{P}$	P_0P
$\tilde{t}$	Tt

Table 4.1: A table showing the conversions between dimensional quantities (left) and non-dimensional quantities (right)

First, considering equation (4.2),

$$
\begin{aligned}
\frac{\partial \tilde{u}}{\partial \tilde{x}} + \frac{\partial \tilde{v}}{\partial \tilde{y}} &= 0 \\
\frac{bU}{LV}\frac{\partial u}{\partial x} + \frac{\partial v}{\partial y} &= 0 \\
\alpha \frac{\partial u}{\partial x} + \frac{\partial v}{\partial y} &= 0
\end{aligned}
$$

where $\alpha = \dfrac{bU}{LV}$. Taking $U = L/T$ and $V = b/T$ yields $\alpha = \dfrac{b}{L}\dfrac{L/T}{b/T} = 1$ and we have the non-dimensionalized continuity equation as

$$\frac{\partial u}{\partial x} + \frac{\partial v}{\partial y} = 0. \tag{4.3}$$

Under this transformation we non-dimensionalize the system so that the length of the plates are set to a length of two units, we set the gap between the pair of plates to 2 units, and the motion of the top plate follows $h_i(x,t), i = 1, 2, 3$ over non-dimensionalized time is described below:

$$h_1(x,t) = atx + at + 1 \quad \text{for } 0 \le t < 1 \tag{4.4}$$

$$h_2(x,t) = a(3-2t)x + a + 1 \quad \text{for } 1 \le t < 2 \tag{4.5}$$

$$h_3(x,t) = -a(3-t)x + a(3-t) + 1 \quad \text{for } 2 \le t \le 3 \tag{4.6}$$

where the parameter a controls the maximum slope of the plates. In general, we can think of h_i for $i = 1, 2, 3$ as

$$h_i(x,t) = a_0(t)x + h_0(t) \tag{4.7}$$

where $a_0(t)$ controls the slope and $h_0(t)$ controls the y-intercept of the plates at time t.

Next, from the vector equation (4.1), we consider the equation in the horizontal $\tilde{x}$ direction:

$$
\begin{aligned}
\mu\left(\frac{\partial^2 \tilde{u}}{\partial \tilde{x}^2} + \frac{\partial^2 \tilde{u}}{\partial \tilde{y}^2}\right) &= \frac{\partial \tilde{P}}{\partial \tilde{x}} \\
\frac{b^2}{L^2}\frac{\partial^2 u}{\partial x^2} + \frac{\partial^2 u}{\partial y^2} &= \frac{b^2 P_0}{U\mu L}\frac{\partial P}{\partial x}
\end{aligned}
$$

Notice that since $b \ll L$, it follows that $\dfrac{b^2}{L^2} \ll 1$, eliminating the first term on the left above. Furthermore, taking

$$P_0 = \frac{U\mu L}{b^2}, \tag{4.8}$$

we non-dimensionalize the horizontal component of equation (4.1) to

$$\frac{\partial^2 u}{\partial y^2} = \frac{\partial P}{\partial x}. \tag{4.9}$$

In what comes to follow, we show that the pressure is not a function of y. To do so, we show that $\dfrac{\partial P}{\partial x} = \dfrac{dP}{dx}$ so that $\dfrac{\partial P}{\partial y} = 0$. Considering the vertical component of equation (4.1),

$$\begin{aligned} \mu\left(\frac{\partial^2 \tilde{v}}{\partial \tilde{x}^2} + \frac{\partial^2 \tilde{v}}{\partial \tilde{y}^2}\right) &= \frac{\partial \tilde{P}}{\partial \tilde{y}} \\ \frac{bV\mu}{P_0}\left(\frac{1}{L^2}\frac{\partial^2 v}{\partial x^2} + \frac{1}{b^2}\frac{\partial^2 v}{\partial y^2}\right) &= \frac{\partial P}{\partial y}. \end{aligned}$$

Substituting P_0 with (4.8), $U = L/T$, and $V = b/T$ into the coefficient on the left hand side of the final step above, we come to

$$\frac{bV\mu}{P_0} = \frac{bV\mu}{(U\mu L)/b^2} = \frac{b^3(b/T)}{(L/T)L} = b^2\frac{b^2}{L^2}. \tag{4.10}$$

Rewriting this term in the equation above yields

$$\begin{aligned} \frac{bV\mu}{P_0}\left(\frac{1}{L^2}\frac{\partial^2 v}{\partial x^2} + \frac{1}{b^2}\frac{\partial^2 v}{\partial y^2}\right) &= \frac{\partial P}{\partial y} \\ \frac{b^2}{L^2}\left(\frac{b^2}{L^2}\frac{\partial^2 v}{\partial x^2} + \frac{\partial^2 v}{\partial y^2}\right) &= \frac{\partial P}{\partial y}. \end{aligned}$$

Following a similar argument as our previous approximation, we see that the left hand side of final step above is negligible as the largest term is on the order of $b^2/L^2 \ll 1$. Therefore pressure is constant in the vertical direction and is only a function of the horizontal coordinate x and t,

$$\frac{\partial P}{\partial x} = \frac{dP}{dx} = P_x(x,t). \tag{4.11}$$

Now, as the right hand side of equation (4.9) is independent of y, we may integrate both sides of the equation twice with respect to y to get

$$u(x,y,t) = \frac{P_x}{2}y^2 + c_1 y + c_2. \tag{4.12}$$

The no-slip boundary condition along the walls of the plates, $u = 0$ when $y = \pm h(x,t)$, allows us to solve for the two constants of integration and we arrive at

$$u(x,y,t) = \frac{P_x}{2}(y^2 - (h(x,t))^2). \tag{4.13}$$

The volumetric flux Q through a vertical cross section is calculated using

$$Q = \int_{-h(x,t)}^{h(x,t)} u\, dy = -\frac{2}{3}P_x(h(x,t))^3. \tag{4.14}$$

Integrating equation (4.3) with respect to y from $y = -h(x,t)$ to $y = h(x,t)$, we have

$$\int_{-h(x,t)}^{h(x,t)} \frac{\partial u}{\partial x} + \frac{\partial v}{\partial y}\, dy = \int_{-h(x,t)}^{h(x,t)} \frac{\partial u}{\partial x}\, dy + 2v(x,h(x,t),t). \tag{4.15}$$

Since $u(x, \pm h(x,t), t) = 0$ by the no-slip boundary condition,

$$\int_{-h(x,t)}^{h(x,t)} \frac{\partial u}{\partial x}\, dy = \frac{\partial}{\partial x}\left(\int_{-h(x,t)}^{h(x,t)} u\, dy\right) = \frac{\partial Q}{\partial x}. \tag{4.16}$$

Applying the no-slip boundary condition again,

$$2v(x,h(x,t),t) = 2\frac{\partial h}{\partial t}. \tag{4.17}$$

Substituting equations (4.16) and (4.17) into equation (4.15), we arrive at

$$\frac{\partial Q}{\partial x} + 2\frac{\partial h}{\partial t} = 0 \tag{4.18}$$

and from this, we see that

$$-Q = 2\int \frac{\partial h}{\partial t}\,dx = 2\dot{h_0}(t)x + \dot{a_0}(t)x^2 + C(t) \tag{4.19}$$

where h_0 and a_0 are described in equation (4.7). Replacing Q with equation (4.14) and solving for P_x, we have

$$P_x = \frac{3}{2(h(x,t))^3}\left(2\dot{h_0}(t)x + \dot{a_0}(t)x^2 + C(t)\right). \tag{4.20}$$

Now, we assume that there is no pressure difference at either end of the arms. This is because the fluid is not driven by a pressure gradient, but rather through the motion of the arms. Therefore,

$$\int_{-1}^{1} P_x\,dx = 0. \tag{4.21}$$

Substituting (4.20) into (4.21), we solve for $C(t)$

$$\int_{-1}^{1} \frac{3}{2(h(x,t))^3}\left(2\dot{h_0}(t)x + \dot{a_0}(t)x^2 + C(t)\right)dx = 0$$

$$\int_{-1}^{1} \frac{2\dot{h_0}(t)x + \dot{a_0}(t)x^2}{(h(x,t))^3}\,dx + C(t)\int_{-1}^{1} \frac{1}{(h(x,t))^3}\,dx = 0$$

from which we see that

$$C(t) = -\frac{\displaystyle\int_{-1}^{1} \frac{2\dot{h_0}(t)x + \dot{a_0}(t)x^2}{(h(x,t))^3}\,dx}{\displaystyle\int_{-1}^{1} \frac{1}{(h(x,t))^3}\,dx} \tag{4.22}$$

First, we integrate the denominator,

$$\int_{-1}^{1} \frac{1}{(h(x,t))^3}\,dx = \int_{-1}^{1} \frac{1}{(h_0(t)+a_0(t)x)^3}\,dx$$

$$= \frac{1}{(h_0(t))^3}\int_{-1}^{1} \frac{1}{(1+mx)^2}\,dx \tag{4.23}$$

$$= \frac{1}{m(h_0(t))^3}\int_{1-m}^{1+m} z^{-3}\,dz$$

$$= \frac{2}{(h_0(t))^3(1-m^2)^2} \tag{4.24}$$

where a substitution $z = 1 + mx$ is made at (4.23) with $m = a_0(t)/h_0(t)$. Next, integrating the numerator of equation (4.22) with the same substitution, we get

$$\int_{-1}^{1} \frac{2\dot{h_0}(t)x + \dot{a_0}(t)x^2}{(h(x,t))^3}\,dx = \frac{1}{m^3(h_0(t))^3}\int_{1-m}^{1+m} \frac{2\dot{h_0}(t)m(z-1) + \dot{a_0}(t)(z-1)^2}{z^3}\,dz$$

$$= \frac{1}{m^3(h_0(t))^3}\int_{1-m}^{1+m} \frac{\dot{a_0}(t)}{z} + \frac{2(\dot{h_0}(t)m - \dot{a_0}(t))}{z^2} + \frac{\dot{a_0}(t) - 2\dot{h_0}(t)m}{z^3}\,dz$$

$$= \frac{1}{m^3(h_0(t))^3}\left(\dot{a_0}(t)\ln\left|\frac{1+m}{1-m}\right| - \frac{4\dot{h_0}(t)m^4 - 4\dot{a_0}(t)m^3 + 2\dot{a_0}(t)m}{(1-m^2)^2}\right) \tag{4.25}$$

Now, using (4.24) and (4.25) in (4.22) we have

$$C(t) = -\frac{\dfrac{1}{m^3(h_0(t))^3}\left(\dot{a_0}(t)\ln\left|\dfrac{1+m}{1-m}\right| - \dfrac{4\dot{h_0}(t)m^4 - 4\dot{a_0}(t)m^3 + 2\dot{a_0}(t)m}{(1-m^2)^2}\right)}{\dfrac{2}{(h_0(t))^3(1-m^2)^2}}$$

$$= -\frac{1}{2m^3}\left(\dot{a_0}(t)(1-m^2)^2\ln\left|\frac{1+m}{1-m}\right| - 4\dot{h_0}(t)m^4 + 4\dot{a_0}(t)m^3 - 2\dot{a_0}(t)m\right) \tag{4.26}$$

To solve for the fluid flow in the vertical direction, we refer back to the continuity equation in (4.3) so that $v = -\int u_x \, dy$. Using (4.13) and differentiating with respect to x,

$$u_x = \frac{1}{2}P_{xx}(y^2 - (h(x,t))^2) - P_x a_0(t) h(x,t) \tag{4.27}$$

Recall that P_x, P_{xx}, and h are functions of only x and t so that when integrating with respect to y

$$v(x,y,t) = -\int u_x \, dy = -\frac{1}{2}P_{xx}\left(\frac{1}{3}y^3 - h^2 y\right) + P_x a_0(t) h(x,t) y + F(x,t). \tag{4.28}$$

By symmetry of the model, the flow along the x-axis must be purely in the x-direction. Evaluating v above for any time t at $y = 0$ shows that $F(x,t) = 0$ and so the vertical component of the flow is

$$v(x,y,t) = -\frac{1}{2}P_{xx}\left(\frac{1}{3}y^3 - (h(x,t))^2 y\right) + P_x a_0(t) h(x,t) y \tag{4.29}$$

$$P_{xx} = \frac{3}{2}\left(\frac{2\dot{h_0}(t) + 2\dot{a_0}(t)x}{(h(x,t))^3} - \frac{3a_0(t)(2\dot{h_0}(t)x + \dot{a_0}(t)x^2 + C(t))}{(h(x,t))^4}\right) \tag{4.30}$$

Using the solutions for the horizontal and vertical velocities in (4.13) and (4.29) we display our results in the next section using non-dimensionalized axis.

4.3 Results

4.3.1 The parameter a

The plots in this section will display images with non-dimensionalized axis. We set the vertical gap between the plates and the horizontal length of the plates to 2 units. By prescribing the length of the vertical gap, we effectively remove one of the parameters from our analysis and focus primarily on the slope of the arms throughout the fling and clap motion. What should be reminded here is that the scale of the horizontal axis has been shrunk quite drastically in this system and that the condition is that the vertical length scale b is orders of magnitude smaller than the horizontal length scale L so that $b \ll L$. We emphasize this point since the following plots could be misinterpreted for a pair of plates that are two units apart and that the slopes are the values that are assigned.

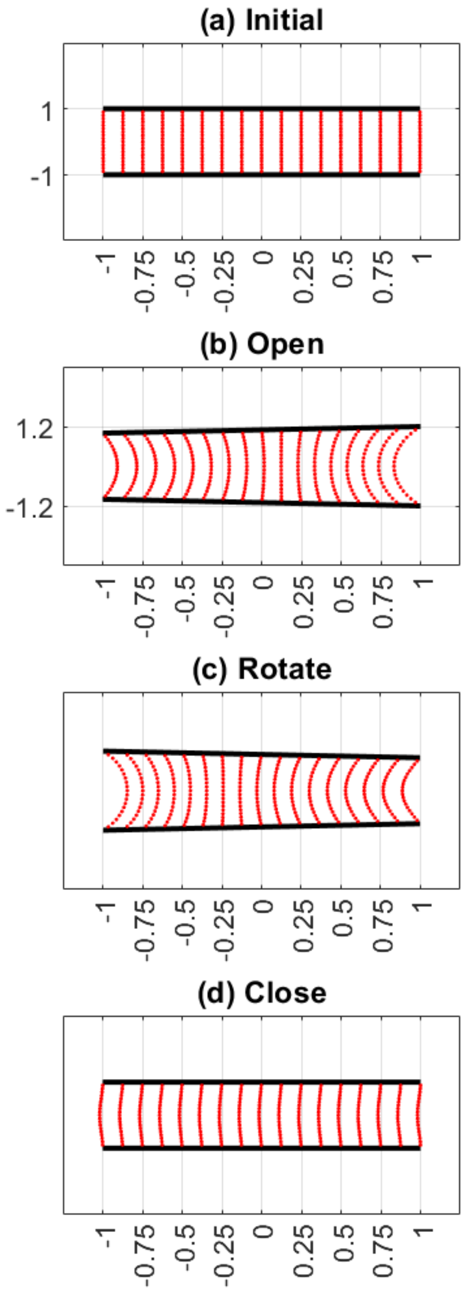

Figure 4.5: Lubrication theory fling at clap with $a = 0.1$, figure scaled. Red points represent particles between the two arms and are arrayed in columns separated by a distance of 0.125 units beginning from the left opening of the arms (body end of copepod) through to the right end of the arms.

In the first set of images in figure 4.5, the maximum slope of the arms is set to $a = 0.1$. We have the initial array of points in 4.5(a) situated as 17 columns spaced 0.125 units apart beginning from the body end of the copepod at $x = -1$ all the way to the opening to the water column on the right at $x = 1$. In the first stage, figure 4.5(b), the arms pivot about leftmost endpoints of the arms until it reaches a slope of $a = 0.1$. Similar to the cases in regularized Stokeslet chapter, there is a distinct parabolic deformation of the columns. In between $x = 0$ and $x = 0.25$, there is a column that maintains its vertical shape while the columns around it bend in toward it. On the left, the vertical columns bend to the right. On the right, the vertical columns bend to the left. Because the left end points of the plates are fixed and the right end points are opening up, there is a rush of fluid coming in from the region outside of the gap between the arms with a larger area being occupied on the right. Furthermore, since the right end opens up, we see that there is more of a vertical displacement between the particles on the right compared to the left. In what follows in the next step is the rotation stage, figure 4.5(c). What we see is a reflected image of the previous step. In this case, the column with vertical component $x = -0.25$ seems to be the most straight while the other columns have a parabolic deformation with the bowing in the same direction. Furthermore, the vertical displacement between particles in the columns is more pronounced on the left end as it opens up. On the opposite side, the ends are coming closer together. Therefore the fluid is being pinched closer together vertically. In the final step, figure 4.5(d), the plates have completed their rotation about the right endpoints and are now parallel. In this step we see that the none of the columns are vertical and are all now bow to the left. There is definitely more of a horizontal displacement for particles near the line of symmetry compared to those near the boundary of the plates. This is a consequence of the no-slip boundary condition where the velocity along the boundaries of the plates is zero. By continuity of the flow field, the displacement becomes stronger as the particles get closer to the line of symmetry $y = 0$.

In the next set of plots, the maximum slope is $a = 0.25$ so that the maximum vertical distance between the endpoints of the plates is 3 units, figure 4.6. There is much of the same qualitative behavior between the stages of the fling and clap as in the previous value of a. In the opening stage, figure 4.6(b), the left endpoints of the plates are fixed while the plates rotate open on the right end. There is a parabolic deformation which causes the vertical columns to bend either to the right or to the left in the vertical slice between $x = 0$ to $x = 0.25$. For the column located nearest $x = 0$, there is a slight bow to the right while the column to its right bow to the left. On the far ends of the plates, we see a lot of area where new fluid has been introduced. Again, since the left end has been fixed, more fluid is introduced on the right end. In the following stage, figure 4.6(c), the plates rotate about their y-intercepts to prepare for the closing stage. This rearranges the fluid to produce

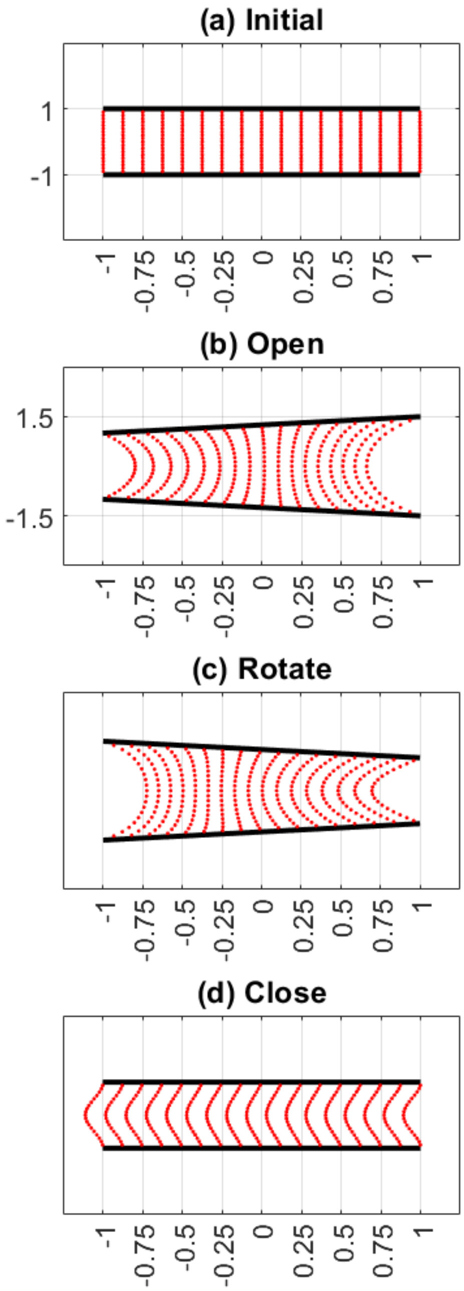

Figure 4.6: Lubrication theory fling at clap with $a = 0.25$, figure scaled. Red points represent particles between the two arms and are arrayed in columns separated by a distance of 0.125 units beginning from the left opening of the arms (body end of copepod) through to the right end of the arms.

an image that is qualitative similar to a reflected image of the previous stage. In this case here, we again see that column along $x = -0.25$ appears to have the least horizontal displacement and the rest of the columns maintain a parabolic shape. Unlike the previous parameter value of $a = 0.1$, we see an overall vertical displacement of particles within each vertical strip. In the final closing stage, figure 4.6, each vertical column is now bowed the left, but stays within it's own strip. The horizontal displacement, like the previous value of a, is again strongest near $y = 0$ and tapers off towards 0 as y approaches the boundary of the plates. While the left most column that originated along the line $x = -1$, looks to have cleared the gap between the arms. However, we should note that the trajectories of particles are not necessarily valid outside of the region where $x \in [-1, 1]$. Looking to the next column on the right, we see that particles near $y = 0$ are nearing the vertical line $x = -1$.

For the plots in figure 4.7, we have set the parameter for the maximum slope of the arms to $a = 0.5$ so that the maximum distance between the two plates is 4 units. After opening up in the first stage, figure 4.5(a), the images look qualitatively similar to what we've seen in the previous two other values of $a = 0.1$ and $a = 0.25$. The maximum distance between the two plates is doubled from the previous case and the amount of new fluid from the outside is increased on both the right and left side of the openings. On the right and left of the line $x = 0$, the columns are now parabolic in shape with the ones to the left bowing to the right and vice-versa for the columns on the right. Where we see a deviation from the previous two cases is in figure 4.7(c). In this image, the model has just completed the rotational phase. In the previous two cases, image (c) was more or less a reflected image of the previous step. In this case, that is not so. Notice that the columns that are to the right of $x = -0.25$ are concave to the right and columns that are left of $x = -0.5$ are concave to the left. However, columns that are in $[-0.5, -0.25]$ are beginning to look like the concavity changes as a function of y. In the final closing stage, figure 4.7(d), we see a replication of a parabolic profile for each column that bows to the left, each with a relatively equal maximum horizontal displacement for particles along the line of symmetry $y = 0$. This behavior seems to be mimicked between each column with the particle along this line translating roughly 0.375 units to the left.

In the final set of plots, figure 4.8, we have images for the fling and clap sequence when $a = 1$. In this case, the maximum distance between the two plates is 4 units. The opening stage, figure 4.8(a), is similar as the previous values of a. As the opening on the right has been increased, there is a larger area of occupied by newly supplied fluid. The column that remains the straightest is located between $x = -0.25$ and $x = 0$. To the right and left, we have the same parabolic profiles that bow in the same directions as the previous cases. However, after the completion of the rotational phase, figure 4.8(c), the rightmost and leftmost columns are either concave to the right or concave to the left. Some columns in between switch in concavity similar to the previous case when $a = 0.5$. What

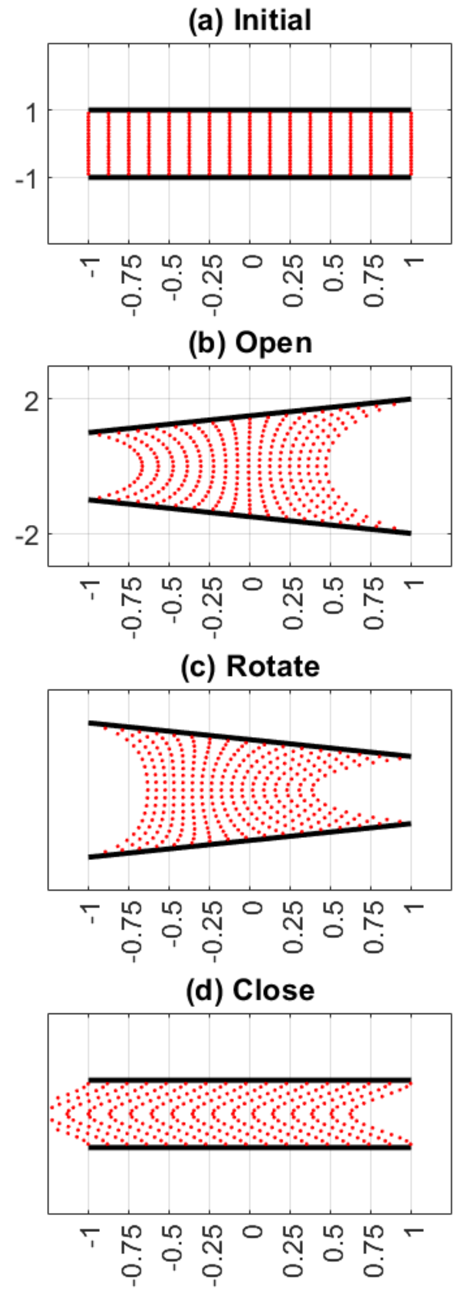

Figure 4.7: Lubrication theory fling at clap with $a = 0.5$, figure scaled. Red points represent particles between the two arms and are arrayed in columns separated by a distance of 0.125 units beginning from the left opening of the arms (body end of copepod) through to the right end of the arms.

is quite interesting in this step is that there appears to be a set of five almost horizontal rows of particles near $y = 0$. In the final step of the sequence after the plates have closed, figure 4.8(d), there is a significant horizontal translation of the particles to the left. Like the previous cases, the largest

(a) Initial

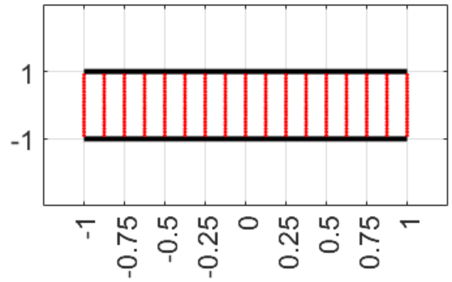

(b) Open

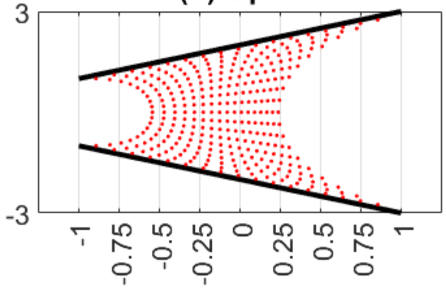

(c) Rotate

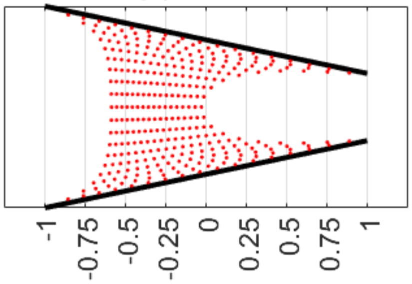

(d) Close

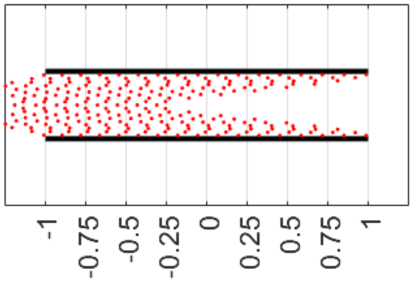

Figure 4.8: Lubrication theory fling at clap with $a = 1.0$, figure scaled. Red points represent particles between the two arms and are arrayed in columns separated by a distance of 0.125 units beginning from the left opening of the arms (body end of copepod) through to the right end of the arms.

horizontal displacement occurs near $y = 0$ and tapers to zero as we move closer to the boundary of the plates. In this case, the rightmost column's particle along the x-axis translates to somewhere in $[-0.5, -0.25]$, a considerable distance more than previous value of a.

What can we infer from these results? In each case, after a single cycle of the fling and clap, there is net displacement of the columns to the left. This displacement is most significant towards the line $y = 0$ and least near the boundaries of the plates. The dynamics in the region near the boundaries follows as a consequence of the no-slip boundary condition. The flow along line of symmetry, $y = 0$, is purely along the x-axis. By symmetry of the model, this is intuitive, but we may also reconfirm this by equation (4.29). That is, along the x-axis, $v(x, 0, t) = 0$. In the intermediate steps where the fling and clap transitions between the stages open, rotate, and close, there are qualitative similarities between all values of $a = 0.1, 0.25, 0.5, 1$. The opening stage serves to drawn in fluid from the two ends with a larger area of fresh fluid on the right end. The rotational stage rearranges the bulk of the fluid from the right to the left. The final closing stages then ejects the fluid out of the left side. From what is apparent as we focus on image (d) of figures 4.5, 4.6, 4.7 and 4.8, the horizontal displacement along the x-axis is depends on the parameter a where the displacement to the left increases as a increases.

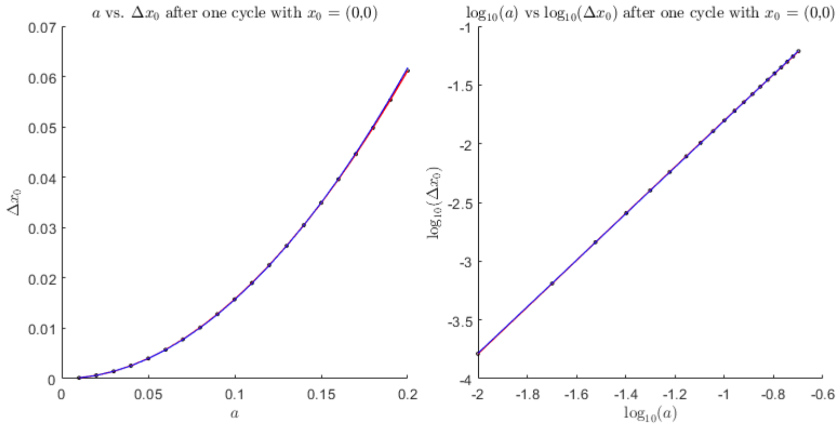
a vs. Δx_0 after one cycle with $x_0 = (0,0)$

$\log_{10}(a)$ vs $\log_{10}(\Delta x_0)$ after one cycle with $x_0 = (0,0)$

Figure 4.9: A graph of the horizontal displacement of a particle located at $\mathbf{x}_0 = [0, 0]'$ for small values of $a \in [0.01, 0.2]$. (a) graph of simulated data in red, blue curve is the approximation by determining the coefficient C and degree n for the graph of Ca^n. (b) Scaling of the axis to $\log_{10}$.

In figure 4.9, we plot our results regarding the increase in horizontal displacement of a particular point $x_0 = [0, 0]'$. For values of amplitude ranging between $a \in [0.01, 0.2]$ we complete a single cycle of the fling and clap motion and calculate its final position. The black dots in 4.9(a) represent the displacement to the left. Following a similar method as in the previous section, we approximate the red curve through the simulated data by a curve of the form Ca^n. Taking $\log_{10}$ of the data and using Matlab's polyfit function, see figure 4.9(b), we find that $C = 1.4906$ and $n = 1.9781$. This indicates that for small values of a, the change in position of the point x_0 is roughly on the order of a^2.

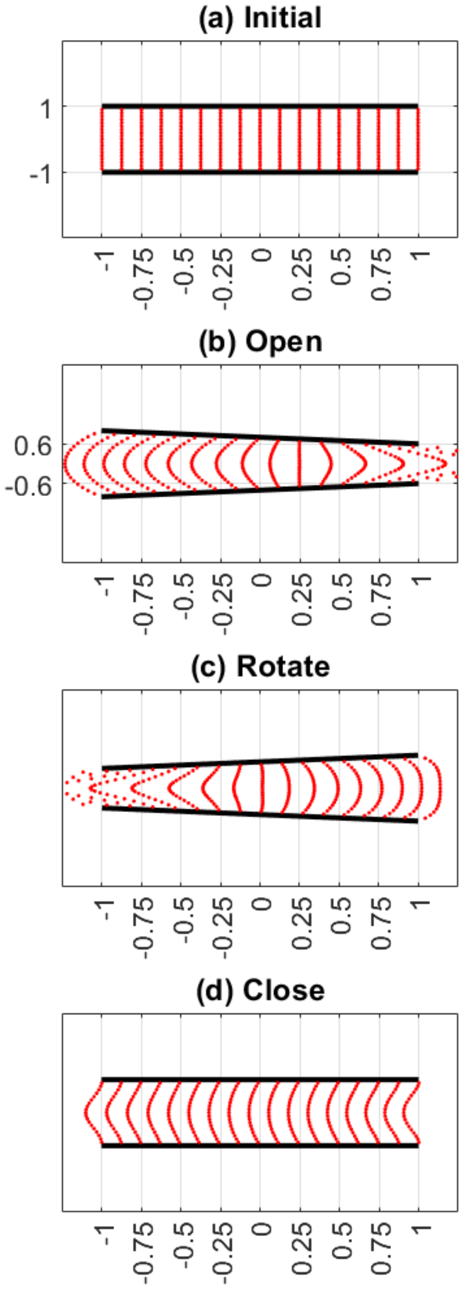

Figure 4.10: Lubrication theory fling at clap with $a = -0.20$, figure scaled. Red points represent particles between the two arms and are arrayed in columns separated by a distance of 0.125 units beginning from the left opening of the arms (body end of copepod) through to the right end of the arms.

An interesting question that we can ask is if the displacement of x_0 is truly on the order of a^2 by conducting analysis on negative values of the amplitude a for relatively small $|a|$. The motion of the arms in this configuration is inherently different than our model's fling and clap. In our model, the arms first open up about the left endpoints, rotate around the midpoint, and then close about the right endpoints. However, if the amplitude is negative, then the arms begin by closing about the left endpoints, rotating about the midpoint, and then opening up about right endpoints.

To demonstrate the change in motion for the amplitude of $a = -0.2$, we plot the time evolution of particles initially located in the same region as our previous analysis for positive amplitude and show the results for $a = -0.2$ in figure 4.10. In figure (b), the arms begin by pivoting about the left endpoints and close in on the right. In this case, the area trapped between the arms decreases as the vertical gap closes to 1.2 units. The particles at either end are ejected from between the region between the arms. Interestingly, there is a column along the line $x = 0.25$ that maintains its vertical nature while the other once vertical columns now are parabolic and bow in their respective direction relative to the column along $x = 0.25$. The columns on the right are affected more significantly than those to the left which is not too surprising as it is the side in which the area between the arms is decreasing the most. In figure 4.10 (c), the arms have finished rotating about midpoint of the arms. Qualitatively, this configuration results in a reflected image of the open stage. However, in this stage, the vertical column has transitioned to the column along $x = 0$ with the other parabolic columns bowing outward from it. As the left is the side in which the area between the arms has decreased, it is the side that the columns bow the most while ejecting particles outward. However, unlike the final closing stage with a positive amplitude a, the arms now open up on the left side. The effect this has on the fluid is that is draws the fluid back into the region between the arms. The final image in figure 4.10 (d) the particles final position after a single cycle. Notice that the image is strikingly similar to 4.6. The columns all bow to the left showing a positive net displacement to left for all of the columns. Furthermore, notice that the displacements are similar in magnitude for the columns. This is probably most easily seen for the columns in the vertical strip between $x = 0.75$ to $x = 1$. Notice that in figure 4.6, the amplitude is $a = 0.25$ but is close in magnitude to the case in figure 4.10 with $a = -0.2$. It is interesting to see that within this strip, the displacement of the columns are comparable and in both cases, stay within that vertical strip.

To investigate further, we take point $x_0 = (0, 0)$ and run a single cycle of the fling and clap with amplitudes ranging between $a = [-0.2, -0.01]$. The results are shown in figure 4.11. On the left in

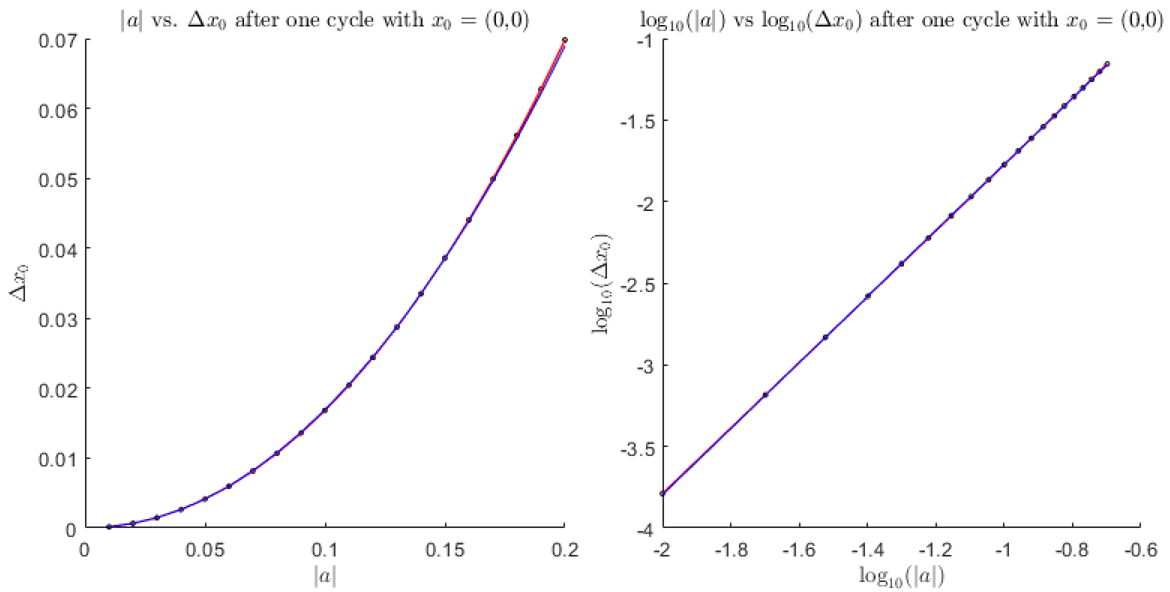

Figure 4.11: A graph of the horizontal displacement of a particle located at $\mathbf{x}_0 = [0, 0]'$ for small values of $a \in [-0.2, -0.1]$. (a) graph of simulated data in red, blue curve is the approximation by determining the coefficient C and degree n for the graph of Ca^n. (b) Scaling of the axis to $\log_{10}$.

figure 4.11 (a), we plot the magnitude of the amplitude versus its net displacement. The simulated data for each value of $|a|$, the displacement is plotted by a blue point and the curve through the points is also shown in blue. Notice that this plot looks very similar to the case for positive amplitude in figure 4.9(a) as it is also parabolic in shape and increases at a comparable rate. Similar to the method for the range of positive amplitudes, we also sought to find an approximate form for the blue curve by assuming that it is of the form $y = Ca^n$. The figure on the left, 4.11(b), we use MatLab's linear approximation command to find that $C = 1.7922$ and $n = 2.0245$, therefore confirming that the blue curve is again roughly on the order of a^2.

Chapter 5

Conclusion

Throughout the course of this document, we've looked to outline some of the events that take place during the copepod's pursuit for food. They must overcome the highly viscous nature of the fluid at their microscopic scale, seek out their food and ultimately bring it into a vicinity close enough that they may consume it. While there may be many stages in their search for food, we outlined and focused on two main certainties: they must be able to detect their prey and they must be able to direct the food to their body.

In the second chapter, we investigated the copepod's ability to detect its prey. The ocean in general is a barren environment and so the animal's ability to effectively and efficiently detect its food is important (Kiørboe 2011a). There are multiple types of feeders and we chose to focus on those who generate their own feeding current as their means of detection. We focused on three modes of feeding: swimming, sinking and hovering. Previous works modelling the flow field of a feeding copepod have neglected a key feature of the copepod's anatomy, the antennae. In our model, the copepod's geometry was simplified in each mode by approximating their long antennae as a single rigid cylinder and their body as a sphere. We used the method of regularized Stokeslets to discretize the antennae and body as a series of spheres. Since the antennae were included with the model, we were able to generate flow fields that would be influenced by their presence and determine the magnitude of disturbances for sensors located along the antennae. After analyzing a background flow field generated by these three modes of feeding, we used Faxen's third law to determine a region around the copepod where a small spherical particle could be detected. Then, treating its feeding current as a sort of conveyor belt, developed a time-dependent volume, a sort of detectable streamtube, around the model which describes the region that each feeding mode would scan for a fixed period of time. What we discovered was that depending on the density of food in the bulk region surrounding the copepod, one mode may be more advantageous than another. In the abundance of food, sinking may be the most energy efficient as the copepod does not have to do anything in order to come into contact with food. But in a more realistic scenario, where food is randomly dispersed throughout the water column, swimming or hovering may prove to be a better strategy. If the food is generally spaced far apart, then swimming may be the better choice as it increases the copepod's chance to encounter food in its detectable volume. However, if a copepod finds a large pocket of food, then hovering may be a better strategy if the copepod can position itself under the source and then hover to pull the food to itself. No one strategy is better than another as the advantages are dependent on the distribution of nutrients within the water column. Past studies on mechanical sensing capabilities have often prescribed a generic background flow field to mimic the flow generated by a feeding copepod or placed particles in specific locations. Our flow fields are determined by approximating the copepod's drag and propulsive forces on the water while engaged in one of three modes of feeding. Furthermore, we gain a larger picture on what the copepod may be able to sense by varying the location of a particle from a particular location to a plane around the copepod and then extend it to a theoretical detectable volume.

The third and fourth chapter is used to investigate the stage in which a copepod has already detected its food and brought it within a region near its feeding appendages. Using Strickler's observations on the motion of the copepod's appendages to maneuver food near its mouth (Strickler 2019), called the fling and clap mechanism, and his experiment described in (Strickler 2019), we developed a simplified motion of this and investigated their influence on the fluid when treating the pair of appendages as either a pair of long slender rods or a pair of plates. While Strickler's observations are a few decades old, there has been no mathematical models to date. Therefore our results are new findings and we are happy to confirm that Strickler's home experiment, see figure 3.1, did indeed lead to positive net displacement.

In chapter three, we treated a pair of appendages as a pair of long slender rods by neglecting the long hairlike setae that align them. We discretized the rods cylindrical shape as rows of spheres and used the method of regularized Stokeslets to compute the flow. We investigated how the variation of two parameters, the pitch of the arms a and initial gap between the arms e, affected the flow in the region trapped between the pair of rods. The first thing we discovered was that any value of a and e that we used produced a net displacement of particles towards the copepod's body. Next, fixing the initial gap between the pair of arms, e, we saw that an increase in amplitude led to an increase in the displacement of particles in the region trapped between them. For small values of a, the net displacement for a particle located at the point $x_0 = (0,0,0)'$ was on the order a^2. Lastly, we fixed the amplitude a and varied the gap e. In this case, there was an opposite effect. The larger the gap, the less of a net displacement.

In the final chapter, we introduced the hairlike setae into our approximation of the copepod's appendages, and treated them as a pair of plates that extend infinitely in the orthogonal direction of the arms. In this case, as each slice in the orthogonal direction is the same, we ultimately had a two-dimensional flow field. We further assumed that the length scale of the gap between the pair of arms is at least an order of magnitude smaller than that for the length of the appendages. This allowed us to use lubrication theory with which we developed a non-dimensionalized model to analyze the flow field. We fixed the gap between the two plates and varied the parameter a which controls the amplitude of the arms throughout the fling and clap motion. What we found here is that again, like the regularized Stokeslet model in which we represent the arms by a pair of slender rods, as the amplitude is increased, so is the net displacement of the fluid trapped between the arms in the direction of the copepod's body. Furthermore, similar to the case with the slender rods, for a particle located at the point $x_0 = (0,0)'$, we saw a net displacement on the order of a^2 after one cycle of the fling and clap.

Throughout this study, we sought to find clues to the secret behind the copepod's feeding ability. In doing so, we introduced a variety of approximations to both the copepod's anatomy and environment. It is true that copepod's do not always operate in a low Reynolds number regime and therefore in future studies, it may be interesting to see how increasing it may have an effect on their ability to sense objects: does it make it easier or less so? We also greatly simplified their anatomy. The copepod's body is not simply a sphere, but much more complicated with multiple sections and have a multitude of appendages with the long hair like setae arrayed along them. We neglected such features for the purpose of beginning a study with a basic figure, one in which others who may be interested in how specific features of the copepod's anatomy may affect and change the flow in the near field can work off. The copepod's appendages are neither slender rods or plates, adding another layer of detail by incorporating setae along a pair of oscillating rods may bring about interesting results. There are many things that can be done to build upon and alter our model. Our hope is that this study has lent enough of a foundation for future studies.

References

Ainley, J., Durkin, S., Embid, R., Boindala, P., and Cortez, R. (2008). The method of images for regularized stokeslets. *Journal of Computational Physics*, 227(9):4600–4616.

Alcaraz, M., Paffenhoffer, G., and Strickler, R. (1980). 22. catching the algae: a first account of visual observations on filter-feeding calanoids. *Evol. Ecol*, 3:241–248.

Andersen, A., Wadhwa, N., and Kiørboe, T. (2015). Quiet swimming at low reynolds number. *Physical Review E*, 91(4):042712.

Andrews, J. C. (1983). Deformation of the active space in the low reynolds number feeding current of calanoid copepods. *Canadian Journal of Fisheries and Aquatic Sciences*, 40(8):1293–1302.

Au, L. T. K., Phan, V. H., and Park, H. C. (2016). Flow analysis of flapping wing in near-clap-and-fling. *A*, pages 508–509.

Becker, L. E., Koehler, S. A., and Stone, H. A. (2003). On self-propulsion of micro-machines at low reynolds number: Purcell's three-link swimmer. *Journal of fluid mechanics*, 490:15–35.

Bundy, M. H., Gross, T. F., Vanderploeg, H. A., and Rudi Strickler, J. (1998). Perception of inert particles by calanoid copepods: behavioral observations and a numerical model. *Journal of plankton research*, 20(11):2129–2152.

Bundy, M. H. and Vanderploeg, H. A. (2002). Detection and capture of inert particles by calanoid copepods: the role of the feeding current. *Journal of plankton research*, 24(3):215–223.

Cannon, H. G. (1928). On the feeding mechanism of the copepods, calanus finmarchicus and diaptomus gracilis. *Journal of Experimental Biology*, 6(2):131–144.

Catton, K. B., Webster, D. R., Brown, J., and Yen, J. (2007). Quantitative analysis of tethered and free-swimming copepodid flow fields. *Journal of Experimental Biology*, 210(2):299–310.

Cheer, A. and Koehl, M. (1987). Paddles and rakes: fluid flow through bristled appendages of small organisms. *Journal of Theoretical Biology*, 129(1):17–39.

Chrispell, J. and Fauci, L. (2011). Peristaltic pumping of solid particles immersed in a viscoelastic fluid. *Mathematical Modelling of Natural Phenomena*, 6(5):67–83.

Cortez, R. (2001). The method of regularized stokeslets. *SIAM Journal on Scientific Computing*, 23(4):1204–1225.

Cortez, R. (2018). Regularized stokeslet segments. *Journal of Computational Physics*, 375:783–796.

Cortez, R., Fauci, L., and Medovikov, A. (2005). The method of regularized stokeslets in three dimensions: analysis, validation, and application to helical swimming. *Physics of Fluids*, 17(3):031504.

Drescher, K., Goldstein, R. E., Michel, N., Polin, M., and Tuval, I. (2010). Direct measurement of the flow field around swimming microorganisms. *Physical Review Letters*, 105(16):168101.

Fauci, L. J. (1992). Peristaltic pumping of solid particles. *Computers & fluids*, 21(4):583–598.

Gimbutas, Z., Greengard, L., and Veerapaneni, S. (2015). Simple and efficient representations for the fundamental solutions of stokes flow in a half-space. *Journal of Fluid Mechanics*, 776.

Giuffre, C., Hinow, P., Jiang, H., and Strickler, J. R. (2019). Oscillations in the near-field feeding current of a calanoid copepod are useful for particle sensing. *Scientific reports*, 9(1):1–8.

Goncalves, R. J. and Kiørboe, T. (2015). Perceiving the algae: How feeding-current feeding copepods detect their nonmotile prey. *Limnology and Oceanography*, 60(4):1286–1297.

Guasto, J. S., Rusconi, R., and Stocker, R. (2012). Fluid mechanics of planktonic microorganisms. *Annual Review of Fluid Mechanics*, 44:373–400.

Hernandez-Ortiz, J. P., Stoltz, C. G., and Graham, M. D. (2005). Transport and collective dynamics in suspensions of confined swimming particles. *Physical review letters*, 95(20):204501.

Hood, K., Jammalamadaka, M. S., and Hosoi, A. E. (2019). Marine crustaceans with hairy appendages: Role of hydrodynamic boundary layers in sensing and feeding. *Physical Review Fluids*, 4(11):114102.

Hung, T.-K. and Brown, T. D. (1976). Solid-particle motion in two-dimensional peristaltic flows. *Journal of Fluid Mechanics*, 73(1):77–96.

Hyon, Y., Powers, T. R., Stocker, R., Fu, H. C., et al. (2012). The wiggling trajectories of bacteria. *Journal of Fluid Mechanics*, 705:58–76.

Jang, Y. I. and Lee, S. J. (2013). Dynamic motion of a butterfly argyronome laodice in ground take-off flight. *Journal of Mechanical Science and Technology*, 27(6):1763–1769.

Jeanneret, R., Contino, M., and Polin, M. (2016). A brief introduction to the model microswimmer chlamydomonas reinhardtii. *The European Physical Journal Special Topics*, 225(11):2141–2156.

Jiang, H., Meneveau, C., and Osborn, T. R. (2002a). The flow field around a freely swimming copepod in steady motion. part ii: Numerical simulation. *Journal of plankton research*, 24(3):191–213.

Jiang, H., Meneveau, C., and R Osborn, T. (1999). Numerical study of the feeding current around a copepod. *Journal of plankton research*, 21(8).

Jiang, H., Osborn, T. R., and Meneveau, C. (2002b). Chemoreception and the deformationof the active space in freely swimming copepods: A numerical study. *Journal of Plankton Research*, 24(5):495–510.

Jiang, H., Osborn, T. R., and Meneveau, C. (2002c). The flow field around a freely swimming copepod in steady motion. part i: Theoretical analysis. *Journal of Plankton Research*, 24(3):167–189.

Jiang, H. and Strickler, J. R. (2005). Mass density contrast in relation to the feeding currents in calanoid copepods. *Journal of plankton research*, 27(10):1003–1012.

Jiang, H. and Strickler, J. R. (2007). Copepod flow modes and modulation: a modelling study of the water currents produced by an unsteadily swimming copepod. *Philosophical Transactions of the Royal Society B: Biological Sciences*, 362(1487):1959–1971.

Kiørboe, T. (2011a). How zooplankton feed: mechanisms, traits and trade-offs. *Biological reviews*, 86(2):311–339.

Kiørboe, T. (2011b). What makes pelagic copepods so successful? *Journal of Plankton Research*, 33(5):677–685.

Kiørboe, T., Gonçalves, R. J., Couespel, D. F., van Someren Gréve, H., Saiz, E., and Tiselius, P. (2016). Prey perception in feeding-current feeding copepods: Reply to comment. *Limnology and Oceanography*, 61(4):1169–1171.

Kiørboe, T. and Jiang, H. (2013). To eat and not be eaten: optimal foraging behaviour in suspension feeding copepods. *Journal of the Royal Society Interface*, 10(78):20120693.

Kiørboe, T., Jiang, H., Gonçalves, R. J., Nielsen, L. T., and Wadhwa, N. (2014). Flow disturbances generated by feeding and swimming zooplankton. *Proceedings of the National Academy of Sciences*, 111(32):11738–11743.

Kiørboe, T. and Visser, A. W. (1999). Predator and prey perception in copepods due to hydromechanical signals. *Marine Ecology Progress Series*, 179:81–95.

Klindt, G. S. and Friedrich, B. M. (2015). Flagellar swimmers oscillate between pusher-and puller-type swimming. *Physical Review E*, 92(6):063019.

Koehl, M. (1981). Feeding at low reynolds number by copepods. *Lectures on mathematics in the life sciences*, 14:89–117.

Kolomenskiy, D., Moffatt, H., Farge, M., and Schneider, K. (2011a). The lighthill–weis-fogh clap–fling–sweep mechanism revisited. *Journal of Fluid Mechanics*, 676:572–606.

Kolomenskiy, D., Moffatt, H., Farge, M., and Schneider, K. (2011b). Two-and three-dimensional numerical simulations of the clap–fling–sweep of hovering insects. *Journal of Fluids and Structures*, 27(5-6):784–791.

Kristineberg Marine Biological Station, S. and Sweden, F. (1990). Foraging behaviour of six calanoid copepods: observations and hydrodynamic analysis. *Marine ecology progress series*, 66:23–33.

Kumar, B. R. and Naidu, K. (1995). A numerical study of peristaltic flows. *Computers & fluids*, 24(2):161–176.

Kumar, S. P., De, A., and Das, D. (2015). Investigation of flow field of clap and fling motion using immersed boundary coupled lattice boltzmann method. *Journal of Fluids and Structures*, 57:247–263.

Lauga, E. and Powers, T. R. (2009). The hydrodynamics of swimming microorganisms. *Reports on progress in physics*, 72(9):096601.

Legier-Visser, M., Mitchell, J., Okubo, A., and Fuhrman, J. (1986). Mechanoreception in calanoid copepods. *Marine Biology*, 90(4):529–535.

Lenz, P. H. and Yen, J. (1993). Distal setal mechanoreceptors of the first antennae of marine copepods. *Bulletin of Marine Science*, 53(1):170–179.

Lighthill, J. (1976). Flagellar hydrodynamics. *SIAM review*, 18(2):161–230.

Lighthill, M. (1973). On the weis-fogh mechanism of lift generation. *Journal of Fluid Mechanics*, 60(1):1–17.

Malkiel, E., Sheng, J., Katz, J., and Strickler, J. R. (2003). The three-dimensional flow field generated by a feeding calanoid copepod measured using digital holography. *Journal of Experimental biology*, 206(20):3657–3666.

Maxey, M. R. and Riley, J. J. (1983). Equation of motion for a small rigid sphere in a nonuniform flow. *The Physics of Fluids*, 26(4):883–889.

Miller, L. A. and Peskin, C. S. (2005). A computational fluid dynamics ofclap and fling'in the smallest insects. *Journal of Experimental Biology*, 208(2):195–212.

Miller, L. A. and Peskin, C. S. (2009). Flexible clap and fling in tiny insect flight. *Journal of Experimental Biology*, 212(19):3076–3090.

Mueller, P. and Thiffeault, J.-L. (2017). Fluid transport and mixing by an unsteady microswimmer. *Physical Review Fluids*, 2(1):013103.

Nguyen, H., Cortez, R., and Fauci, L. (2014). Computing flows around microorganisms: slender-body theory and beyond. *The American Mathematical Monthly*, 121(9):810–823.

Paffenhöfer, G.-A. and Jiang, H. (2016). Comment: On phytoplankton perception by calanoid copepods. *Limnology and Oceanography*, 61(4):1163–1168.

Perçin, M., Hu, Y., Van Oudheusden, B. W., Remes, B., and Scarano, F. (2011). Wing flexibility effects in clap-and-fling. *International Journal of Micro Air Vehicles*, 3(4):217–227.

Price, H. J. (1988). Feeding mechanisms in marine and freshwater zooplankton. *Bulletin of Marine Science*, 43(3):327–343.

Price, H. J., Paffenhöfer, G.-A., and Strickler, J. R. (1983). Modes of cell capture in calanoid copepods 1. *Limnology and Oceanography*, 28(1):116–123.

Purcell, E. M. (1977). Life at low reynolds number. *American journal of physics*, 45(1):3–11.

Santhanakrishnan, A., Robinson, A. K., Jones, S., Low, A. A., Gadi, S., Hedrick, T. L., and Miller, L. A. (2014). Clap and fling mechanism with interacting porous wings in tiny insect flight. *Journal of Experimental Biology*, 217(21):3898–3909.

Shapiro, A. H., Jaffrin, M. Y., and Weinberg, S. L. (1969). Peristaltic pumping with long wavelengths at low reynolds number. *Journal of fluid mechanics*, 37(4):799–825.

Shen, X. and Fu, H. C. (2020). How the bending mechanics of setae modulate hydrodynamic sensing in copepods. *Limnology and Oceanography*, 65(4):749–761.

Strickler, J. (1985). Feeding currents in calanoid copepods: two new hypotheses. In *Symposia of the Society for Experimental Biology*, volume 39, pages 459–485.

Strickler, J. R. (1982). Calanoid copepods, feeding currents, and the role of gravity. *Science*, 218(4568):158–160.

Strickler, J. R. (2019). Sticky water: a selective force in copepod evolution. In *Trophic interactions within aquatic ecosystems*, pages 187–239. Routledge.

Strickler, J. R. and Bal, A. K. (1973). Setae of the first antennae of the copepod cyclops scutifer (sars): their structure and importance. *Proceedings of the National Academy of Sciences*, 70(9):2656–2659.

Takagi, D. and Strickler, J. R. (2020). Active hydrodynamic imaging of a rigid spherical particle. *Scientific reports*, 10(1):1–10.

Tamm, S. L. (1972). Ciliary motion in paramecium: a scanning electron microscope study. *The Journal of cell biology*, 55(1):250.

van Duren, L. A., Stamhuis, E. J., and Videler, J. J. (2003). Copepod feeding currents: flow patterns, filtration rates and energetics. *Journal of Experimental Biology*, 206(2):255–267.

van Duren, L. A. and Videler, J. J. (2003). Escape from viscosity: the kinematics and hydrodynamics of copepod foraging and escape swimming. *Journal of Experimental Biology*, 206(2):269–279.

Villanueva, R., Nozais, C., and Boletzky, S. v. (1997). Swimming behaviour and food searching in planktonic octopus vulgaris cuvier from hatching to settlement. *Journal of Experimental Marine Biology and Ecology*, 208(1-2):169–184.

Visser, A. W. (2001). Hydromechanical signals in the plankton. *Marine Ecology Progress Series*, 222:1–24.

Yen, J. and Okubo, A. (2002). Particle and prey detection by mechanoreceptive copepods: a mathematical analysis. *Hydrobiologia*, 480(1):165–173.